APPLICATION OF MULTIMODAL OPTICAL IMAGING FOR BRAIN FUNCTION MAPPING AND LIVER FIBROSIS MONITORING

WEIRAN PANG

PhD

The Hong Kong Polytechnic University

2025

The Hong Kong Polytechnic University

Department of Biomedical Engineering

Application of Multimodal Optical Imaging for Brain Function Mapping and Liver Fibrosis Monitoring

PANG Weiran

A thesis submitted in partial fulfillment of the requirements for the degree of Doctor of Philosophy

July 2025

CERTIFICATE OF ORIGINALITY

I hereby declare that this thesis is my own work and that, to the best of my knowledge and belief, it reproduces no material previously published or written, nor material that has been accepted for the award of any other degree or diploma, except where due acknowledgement has been made in the text.

_____ (Signed)

PANG, WEIRAN

_____(Name of student)

ABSTRACT

Optical imaging has increasingly gained prominence as a transformative modality in biomedical research due to its unique capacity for non-invasive imaging with high resolution and molecular specificity. Traditional medical imaging techniques, such as X-ray imaging, computed tomography (CT), magnetic resonance imaging (MRI), positron emission tomography (PET), and ultrasound (US), are widely utilized but are inherently limited in resolving cellular-level structural and functional details. Pure optical imaging methods, despite achieving high resolution, are significantly affected by strong tissue scattering, which greatly limits imaging depth and induces an urgent need for techniques that overcome these barriers. Emerging optical imaging methods, notably photoacoustic imaging (PAI), have been developed to overcome these limitations. PAI relies on optical absorption to provide intrinsic optical contrast of biological tissues, significantly overcoming the influence of optical scattering. This hybrid technology offers deeper penetration and superior contrast by combining optical excitation with acoustic detection.

PAI leverages the photoacoustic effect, in which absorbed pulsed laser energy in biological tissues induces thermoelastic expansion, generating acoustic signals detectable by ultrasound transducers. This hybrid modality surpasses traditional optical imaging methods by providing enhanced imaging depth, reduced scattering effects, and greater sensitivity to endogenous and exogenous contrast agents. Multiscale photoacoustic technologies, including photoacoustic computed tomography (PACT), photoacoustic microscopy (PAM), and photoacoustic endoscopy (PAE), have demonstrated promising applications in neuroscience, oncology, and hepatology. Recently, PAI has demonstrated clear advantages and extensive research potential in areas such as brain function mapping and liver disease detection. In brain function mapping, it provides valuable parameters including cerebral electrophysiological activities, oxygenation levels, and hemodynamic responses, which is essential for neurological research and disease diagnostics. Regarding liver disease detection, PAI effectively assesses microvascular structures, tissue oxygenation, and biomechanical properties, significantly contributing to early diagnosis and monitoring of liver conditions such as fibrosis and hepatocellular carcinoma.

This thesis specifically explores two significant biomedical applications of PAI: brain function mapping and liver fibrosis detection. In the first part, brain function mapping, we demonstrate PAI's capability to perform label-free, high-resolution imaging of cerebral electrophysiological activities, essential for diagnosing neurological disorders such as epilepsy. Our work is divided into three parts. Firstly, cellular experiments validated the optical response mechanism of voltage-sensitive dyes (VSD), demonstrating opposite changes in photoacoustic and fluorescence intensities in relation to membrane potentials, adhering strictly to energy conservation. Secondly, we utilized *in-vivo* fluorescence imaging to track VSD signals in epileptic mouse models, aligning with our cellular observations. However, the relatively low temporal and spatial resolution limited the signal mapping to minute-level temporal dynamics across the whole brain, restricting precise microscopic localization and detailed observation of epilepsy. Thirdly, PACT was employed, achieving a high-resolution (approximately 100 μm) whole-brain coverage (5.5 cm width) with substantial imaging depth (down to 4 mm) and a high imaging frame rate (up to 10 Hz). Our findings revealed that this method directly tracked epileptic signals, accurately localized epileptic foci within specific brain regions, and demonstrated the transmission and interaction among these epileptic foci. Through this innovative VSD technique combined with PAI (PA-VSD), real-time monitoring and precise localization of epileptiform discharges were achieved, providing a potential tool for intraoperative guidance and therapeutic intervention.

The second part focuses on liver fibrosis detection, presenting a novel photoacoustic elastomicroscopy (PAEM) system that integrates structural vascular imaging and biomechanical assessment via time-of-flight (ToF) quantification — a method particularly well-suited to the liver due to its rich vascularization and hemoglobin content, which enhance compatibility with photoacoustic monitoring. The exploration was divided into two parts. Firstly, we utilized high-resolution PAM to image liver tissue sections and found that significant alterations in vascular architecture—especially hepatic lobule structures—were already evident at the early stages of fibrosis. This finding aligns with existing literature, which indicates that structural changes precede biomechanical property alterations. However, we observed that structural imaging alone could only distinguish early fibrosis (0-3 weeks), but it failed to effectively differentiate middle to late stages. Therefore, we proposed a second component utilizing ToF-based elasticity quantification derived from ultrasound propagation speed through tissue to infer relative stiffness. Although this does not yield absolute mechanical values, it enables quantitative comparisons across the full spectrum of fibrosis (0-

16 weeks). This approach offers clear advantages in early-stage detection and addresses the limitations of shear wave elastography (SWE), which lacks sufficient sensitivity for early-stage diagnosis. This methodology allows early, sensitive detection of subtle hepatic changes, surpassing conventional imaging techniques in accurately staging fibrosis progression. By coupling structural vascular analysis with biomechanical quantification, this approach offers a comprehensive diagnostic platform for chronic liver disease management as well as the potential in hepatic tumor margins.

The presented work underscores the translational potential of photoacoustic modalities in clinical diagnostics and personalized medicine, establishing a methodological foundation for future advancements in biomedical imaging. Specifically, in the context of brain function mapping, the integration of PA-VSD paves the way for noninvasive, real-time neurophysiological monitoring with both spatial specificity and temporal precision—capabilities highly desirable for epilepsy surgery, brain-computer interface development, and broader neurological disease management. Similarly, in hepatology, the development of PAEM for concurrent structural and biomechanical assessment presents a promising solution for the early detection and quantitative staging of liver fibrosis. As liver fibrosis remains clinically underdiagnosed in its initial stages, the sensitivity and depth-resolved precision offered by PAI hold great potential for improving patient outcomes. With further optimization and validation, the methods presented in this thesis may accelerate the translation of PAI into routine clinical workflows, offering clinicians robust tools for real-time, label-free, and multi-parametric disease evaluation.

PUBLICATIONS ARISING FROM THE THESIS

Peer-reviewed Journal Publications

(†equal contribution)

1. **Weiran Pang**, Qi Zhou, Yang Qiu, Jiali Chen, Haofan Huang, Tianting Zhong, Yingying Zhou*, Liming Nie* and Puxiang Lai*. "Multi-Parametric Photoacoustic Elastomicroscopy: Quantitative Elasticity Mapping and Microstructural Analysis for Early-Stage Hepatic Fibrosis Detection." *Journal of Physics: Photonics* (2025): *In press.*

2. **Weiran Pang**†, Tianting Zhong†, Yize Gao†**,** Xiazi Huang†, Wu Yuan, Di Mei, Xingde Li, Kenneth K. Y. Wong, Xin Dong, Qiuqiang Zhan, Rui Pu, Zhenhua Hu, Daifa Wang, Di Wu, Changhui Li, Qinrong Zhang, Liulin He, Yuecheng Shen, Shian Zhang, Jiamiao Yang, Chunxu Ding, Lei Gong, Jing-Han Zhuang, Qing Yang, Quanzhi Li, Liangcai Cao, Jiachen Wu, Pengcheng Li, Jiachi Hong, Tingting Yu, Valery V. Tuchin, Chao Zuo, Haigang Ma, Yingying Zhou, Honglin Liu, Xuyu Zhang, Jie Tian*, Dan Zhu*, Cheng Ma*, and Puxiang Lai*. "Deep-Tissue Optics: Multidisciplinary Innovations and Emerging Frontiers – A Comprehensive Review." *PhotoniX Life* (2025): *Under review.*

3. **Weiran Pang**, Bowen Zhu, Honghui Li, Yingying Zhou, Chi Man Woo, Xiazi Huang, Tianting Zhong, Hsuan Lo, Laiyou Wang, Puxiang Lai* and Liming Nie*. "Direct Monitoring of Whole-Brain Electrodynamics via High-Spatiotemporal-Resolution Photoacoustics with Voltage-Sensitive Dye." *Laser & Photonics Reviews* 18(10): 2400165 (2024).

4. Siyang Zheng†, Wenzhao Li†, **Weiran Pang**†, Tianting Zhong* and Puxiang Lai*. "Optical Transparency in Live Animals: A Leap Toward Deep-tissue Applications." *Advanced Photonics* 6(6): 060504 (2024).

5. **Weiran Pang**†, Chuqi Yuan†, Tianting Zhong, Xiazi Huang, Yue Pan, Junle Qu, Liming Nie*, Yingying Zhou* and Puxiang Lai*. " Diagnostic and Therapeutic Optical Imaging in Cardiovascular Diseases." *iScience* 27(11): 111216 (2024).

6. **Weiran Pang**†, Chuqi Yuan†, Yuandong Zheng, Tianting Zhong* and Puxiang Lai*. "Applications Over the Horizon—Advancements and Challenges in Brain-computer Interfaces." *The Innovation Life* 2(1): 100058-1 (2024).

7. Xiazi Huang, Hui Hui, Wenting Shang, Pengli Gao, Yingying Zhou, **Weiran Pang**, Chi Man Woo, Jie Tian* and Puxiang Lai*. "Deep penetrating and sensitive targeted magnetic particle imaging and photothermal therapy of early-stage glioblastoma based on a biomimetic nanoplatform." *Advanced Science* 10(19): 2300854 (2023).

8. Wenzhao Li, Yuandong Zheng, **Weiran Pang** and Puxiang Lai*. "Bio-inspired adhesive hydrogel for wound healing." *Biomedical Technology* 1: 65-72 (2023).

9. Yingying Zhou, Xiazi Huang, Jiyu Li, Ting Zhu, **Weiran Pang**, Larry Chow, Liming Nie, Lei Sun and Puxiang Lai*. "Small animal in situ drug delivery effects via transdermal microneedles array versus intravenous injection: a pilot observation based on photoacoustic tomography." *Pharmaceutics* 14(12): 2689 (2022).

10. Zhipeng Yu, Huanhao Li, Tianting Zhong, Jung-Hoon Park, Shengfu Cheng, Chi Man Woo, Qi Zhao, Jing Yao, Yingying Zhou, Xiazi Huang, **Weiran Pang**, Hansol Yoon, Yuecheng Shen, Honglin Liu, Yuanjin Zheng, YongKeun Park*, Lihong V. Wang* and Puxiang Lai*. "Wavefront shaping: a versatile tool to conquer multiple scattering in multidisciplinary fields." *The Innovation* 3(5): 100292 (2022).

11. **Weiran Pang**, Yongjun Wang, Lili Guo, Bo Wang, Puxiang Lai and Jiaying Xiao*. "Two-dimensional Photoacoustic/Ultrasonic Endoscopic Imaging Based on A Line-focused Transducer." *Frontiers in Bioengineering and Biotechnology* 9: 807633 (2022).

12. Bo Wang, Congcong Wang, Fangyi Zhong, **Weiran Pang**, Lili Guo, Kuan Peng and Jiaying Xiao*. “3D acoustic resolution-based photoacoustic endoscopy with dynamic focusing.” *Quantitative Imaging in Medicine and Surgery* 11(2): 685 (2021).

Conference Presentation

1. **Weiran Pang** and Puxiang Lai. “Multiscale deep-tissue photoacoustic imaging.” *Light Conference 2025*, Changchun, China, 2025 (*Invited talk*)

2. **Weiran Pang**, Liming Nie and Puxiang Lai. “Voltage-sensitive Dye-based Photoacoustic Imaging Visualization of Whole Brain Electrodynamics.” *SPIE Photonics West 2025*, San Francisco, USA, 2025 (*Poster*)

3. **Weiran Pang**, Puxiang Lai and Liming Nie. “Voltage-sensitive Dye-based Photoacoustic Imaging Visualization of Whole Brain Electrodynamics.” *The 12th International Conference on Nanophotonics*, Shenzhen, China, 2024 (*Oral*)

4. **Weiran Pang** and Puxiang Lai. “Photoacoustic Visualization of Epilepsy in vivo.” *Advanced Photonics 5th Anniversary Forum*, Shenzhen, China, 2024 (*Best Poster Award*)

5. **Weiran Pang**, Yingying Zhou, Xiazi Huang, Puxiang Lai and Liming Nie. “Long-term non-invasive monitoring of neuronal electrical activity throughout the cerebral cortex by photoacoustic imaging with voltage-sensitive dyes.” *2023 China Biomedical Engineering Conference & Medical Innovation Summit*, Suzhou, China, 2023 (*Poster*)

6. **Weiran Pang**, Bo Wang, Puxiang Lai and Jiaying Xiao. “Two-Dimensional acoustic-resolution Photoacoustic/Ultrasonic Endoscopic Imaging Based on a Line-Focused Transducer.” *The 15th International Conference on Photonics and Imaging in Biology and Medicine (PIBM, 2021)*, Haikou, China, 2021 (*Poster*)

ACKNOWLEDGEMENT

Time flies swiftly, and my four-year doctoral research journey is approaching its conclusion, marking the end of over two decades of my academic pursuit. As the proverb goes, "Many have good beginnings, but few have good endings." I feel fortunate to have maintained unwavering determination and initial enthusiasm throughout these years, consistently advancing on the path of scientific exploration and making modest contributions to the community.

First and foremost, I would like to express my deepest gratitude to my Chief Supervisor, Professor Puxiang Lai, for his invaluable guidance, support, and mentorship throughout my Ph.D. studies. Professor Lai has generously provided comprehensive experimental facilities, insightful suggestions on research methodologies, and valuable guidance in academic writing and presentation. Beyond academic mentorship, he has consistently offered encouragement, support, and assistance during challenging times, significantly easing my difficulties. My sincere thanks to Professor Lai for his unwavering support.

I am also deeply grateful to Professor Liming Nie from Guangdong Provincial People's Hospital. During my doctoral studies, multiple research projects were completed at the Optical Molecular Imaging Platform under his generous provision of comprehensive resources. Professor Nie provided extensive assistance in resolving experimental challenges, substantially facilitating the smooth progression of my research. His insightful advice and substantial support in manuscript preparation and publication have also been invaluable.

I extend my appreciation to senior lab colleagues, Yingying Zhou, Xiazi Huang, Jing Lv, and Xiaoxiao Jiang, as well as Tianting Zhong, Honghui Li, for their practical advice and invaluable assistance throughout experiments. I also thank my classmates Chi Man Woo and Jing Yao, whose companionship brought joy to my monotonous research life, alongside their kind assistance in coursework and daily activities. My thanks further extend to junior colleagues Chuqi Yuan, Qi Zhou, Jiali Chen, Lanqing Li, Tong Sun, Haofan Huang, Yang Qiu, and Kai Long for their generous experimental support. Additionally, I appreciate Zhipeng Yu, Huanhao Li, Shengfu Cheng, Qi Zhao, Xiaozhou Xiao, Yuzhen Li, Haoran Li, Yuandong Zheng, Zhiyuan Wang, Kai Chen, Weibin Cai, Siyang Zheng, and other laboratory colleagues whose companionship has made my lab experience pleasant and memorable.

Finally, I sincerely thank my parents, family and lover for their quiet yet steadfast support, enabling me to pursue my academic goals without distraction or undue pressure.

The conclusion of my Ph.D. marks not an end but the beginning of a new journey. It is my sincere hope to maintain the enthusiasm I have fostered, remain at the forefront of scientific inquiry, overcome internal obstacles, and continue advancing bravely along this path.

TABLE OF CONTENT

LIST OF TABLES

LIST OF FIGURES

Chapter 1 Introduction

1.1 Background and significance of optical imaging in biomedical research

1.1.1 Conventional imaging methods in biomedicine

Clinically, commonly employed medical imaging techniques include X-ray imaging/computed tomography (CT), magnetic resonance imaging (MRI), positron emission tomography/single photon emission computed tomography (PET/SPECT), and ultrasound (US) imaging.

X-ray imaging, also known as Rontgen imaging, operates by exploiting differential attenuation of X-rays, determined by variations in thickness or density among biological tissues or organs. CT imaging employs rotating X-ray scanners combined with computational reconstruction to generate cross-sectional tomographic images of specific anatomical regions [1]. The primary advantage of CT imaging lies in its substantial tissue penetration capability, making it highly effective for imaging deep organs and cerebral tissues [2]. Nevertheless, the inherent ionizing radiation exposure remains an unavoidable limitation. Consequently, CT imaging is unsuitable for long-term monitoring of chronic diseases or continuous assessment of tumor progression and prognosis [3].

As its name suggests, MRI technology is fundamentally based on magnetic resonance phenomena [4, 5]. MRI has notable advantages, such as absence of ionizing radiation, excellent tissue penetration depth, and relatively high spatial resolution [5]. Currently, MRI is extensively utilized in clinical applications such as imaging vital organs (*e.g.*, liver and kidneys), the central nervous system, bones, and joints [6, 7]. Functional MRI (fMRI) further provides dynamic monitoring of blood flow, thus offering functional insights, particularly relevant for neurological conditions [8]. Despite these substantial advantages, MRI still faces some limitations, including prolonged scanning times, high maintenance costs, patient intolerance due to claustrophobia, and contraindications such as cardiac pacemakers, restricting its applicability for certain patient groups in clinical practice [9].

PET and SPECT, cornerstone techniques in nuclear medicine, utilize γ-ray emissions from systemically administered radiopharmaceuticals (e.g., ^{18}F-FDG for tracking glucose metabolism, or ^{99m}Tc-ECD for visualizing cerebral blood flow distribution) to reconstruct

tomographic images reflecting biological processes at molecular levels. The emitted positrons annihilate with electrons, producing single or paired gamma photons as the signal source, which are detected and reconstructed into metabolic images depicting tracer distribution [10]. They are frequently combined with CT or MRI modalities (PET/CT, PET/MRI or SPECT/CT), integrating functional and anatomical information. PET and SPECT have extensive clinical applications in oncology detection, neurological diseases (such as Alzheimer's disease and epileptic foci localization), and cardiovascular disorders, as well as important roles in pharmaceutical research and neurofunctional studies [11, 12]. Advantages of nuclear imaging include high sensitivity, functional imaging capabilities, and multimodal imaging integration. Conversely, limitations include radiation exposure risks, restricted spatial resolution, high equipment costs, and susceptibility to false-positive or false-negative results caused by inflammatory processes or low metabolic tumors [13].

US imaging is widely adopted in clinical practice, utilizing acoustic impedance differences among biological tissues or organs. Ultrasound waves reflect differently due to various attenuations in different tissues, thus enabling visualization based on these impedance variations [14]. Ultrasound imaging is extensively employed in thyroid and breast surgery, obstetrics and gynecology, and cardiovascular diseases [15]. Shear-wave ultrasound elastography (SWE) further provides tissue elasticity assessment (*e.g.*, in the liver), although its relatively low sensitivity increases the likelihood of missed or erroneous diagnoses in early-stage conditions [16, 17]. The primary advantages of US imaging include ease of operation, rapid imaging procedures, low costs, minimal maintenance requirements, and the absence of ionizing radiation. In addition, ultrasonography significantly reduces patient mobilization, facilitating convenient imaging examinations. However, the major drawbacks include lower imaging resolution and substantial operator dependency, potentially leading to variability in diagnostic outcomes among different examiners for the same patient or pathology.

1.1.2 Emerging optical imaging modalities and limitations

Traditionally, the above-mentioned clinical imaging modalities have predominantly been employed for disease diagnosis. However, these techniques typically provide macroscopic assessments and fail to resolve details at molecular, cellular, microvascular, or functional tissue levels. On this aspect, optical imaging is attractive, tending to reveal microscopic structural and functional details at cellular resolution.

Within the electromagnetic spectrum, optical radiation—particularly visible and near-infrared (NIR) light—is uniquely capable of interacting directly with almost all types of biological molecules, such as DNA/RNA, glucose, lipids, cytochromes, hemoglobin, melanin, and water. Consequently, optical imaging techniques can provide comprehensive insights into the structural, functional, metabolic, and molecular characteristics of cells and tissues, such as hemoglobin concentration, oxygen saturation, blood flow, and vascular density [18]. In recent years, optical imaging has emerged as an innovative biomedical imaging modality, attracting significant attention due to its distinct advantages compared to conventional medical imaging methods. Specifically, biomedical optics offers the following strengths: 1. Optical photons represent a safe electromagnetic wave range, and optical detection systems are relatively simple in design and cost-effective. 2. Spectral imaging based on absorption, fluorescence, or Raman scattering provides biochemical information directly related to molecular conformations [19]. 3. Optical absorption reveals information about angiogenesis and metabolic processes—both critical indicators for disease diagnosis [20]. Angiogenesis is associated with hemoglobin concentration, whereas metabolic processes correlate with blood oxygen saturation; hence, optical absorption enhances contrast for functional imaging [21]. 4. Optical polarization yields valuable information about structural tissue components, such as collagen and muscle fibers [22]. 5. Optical frequency shifts generated by the Doppler effect provide quantitative insights into blood flow dynamics [23]. 6. Optical characteristics of targeted contrast agents facilitate molecular imaging of specific biomarkers, offering exceptional contrast enhancement [24]. 7. Optical properties of gene expression products or bioluminescence signals enable molecular imaging related to genetic activity [25]. 8. Optical spectroscopy allows simultaneous detection of multiple molecules with different absorption wavelengths [26], an advantage not achievable by positron emission tomography (PET), which utilizes a single wavelength and frequency. 9. Optical transparency of the eye uniquely facilitates high-resolution retinal imaging with optical coherence tomography (OCT) [27].

It should be highlighted that propagation of light within biological tissues is inherently heterogeneous, characterized by high scattering, such that only a minimal fraction of photons penetrates deeper than approximately 1 mm beneath the human skin without experiencing multiple scattering events. For most optical imaging techniques, imaging depth and resolution inherently constitute a trade-off.

Historically, optical microscopy has been developed approximately three centuries ago, which provided excellent resolution but is with a limited penetration depth of roughly 100

μm. Following the advent of lasers, the development of confocal, two-photon, and multiphoton microscopy [28] has leveraged high-energy excitation sources, subsequently augmented by OCT [29], based on optical diffraction and coherence properties, to increase imaging depths up to approximately 1.5 mm. The emergence of photoacoustic imaging (PAI) represented a significant breakthrough by converting light, regardless of ballistic or diffusive states, into not-so-scattering sound, which diminishes the influence of optical scattering but amplifies optical absorption at the signal excitation stage. This helps enhance penetration depth by two orders of magnitude to several centimeters [30, 31]. Currently, PAI enables whole-body imaging of small animals and provides real-time, noninvasive visualization of multiple internal organs, representing a unique optical imaging technology that simultaneously achieves both high spatial resolution and relatively deep penetration depth among existing modalities.

Nonetheless, PAI continues to face critical challenges, particularly regarding how to further overcome depth limitations, achieve structural and functional imaging of deep internal organs, and develop multimodal strategies capable of simultaneous monitoring and quantitative analysis of multiple physiological parameters.

1.2 Photoacoustic imaging and its applications

1.2.1 Principle of photoacoustic imaging

PAI represents an emerging imaging modality, fundamentally based on the photoacoustic (PA) effect, first described by Alexander Graham Bell in 1880 [32]. When molecules absorb photons, they transition from the ground state to an excited state. The energy is primarily released through two pathways: radiative decay (i.e., fluorescence) and non-radiative decay (thermal dissipation). If the excitation light is a short pulse (time domain) or intensity-modulated (frequency domain), the heat generated during the non-radiative decay process will produce ultrasound waves through thermoelastic expansion, known as PA waves. So, the underlying principle of PAI involves the exposure of biological tissues to short pulses of non-ionizing light, where absorption by local biomolecules induces transient thermal expansion, consequently generating acoustic pressure waves (ultrasound waves), as illustrated in Figure 1-1. These ultrasound waves are subsequently detected by ultrasonic sensors to form or reconstruct images that reflect the spatial distribution of optical absorption within the targeted region [33, 34].

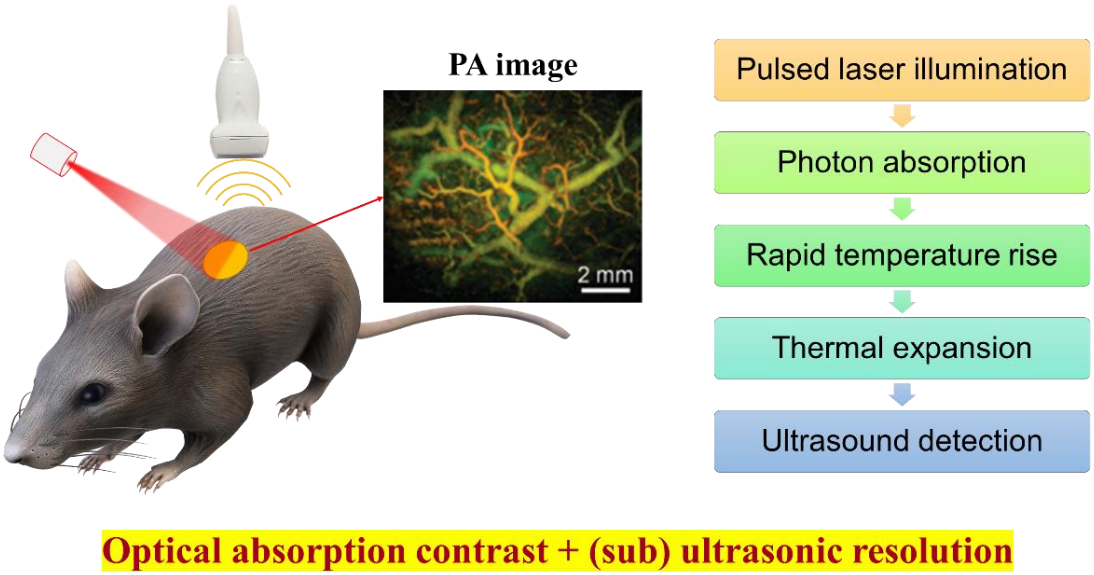

Figure 1-1. The principle of photoacoustic imaging. This process leverages the strong contrast of optical absorption and the high spatial resolution of ultrasound imaging in deep tissues, enabling high-resolution visualization of both structural and functional information such as vasculature, blood oxygenation, and molecular expression.

PAI combines the advantages of optical excitation and acoustic detection, forming a hybrid imaging modality that is highly sensitive to optical absorption and capable of deep tissue imaging. While purely optical imaging methods can also detect optical absorption by measuring changes in the intensity of transmitted or reflected light, their sensitivity is typically two orders of magnitude lower than that of PAI [35]. Furthermore, since the scattering coefficient of sound waves in biological tissues is much lower than that of light, it can provide high spatial resolution imaging at greater depths than traditional optical imaging methods, thus overcoming the optical diffusion limit.

In recent years, driven by advancements in laser design and ultrasound detection technology, the PA effect has found widespread application across various fields, from fundamental science to engineering. In biomedicine, the application of the PA effect began in the 1970s [36], and its applicability in optical scattering media and biological tissues has been demonstrated in recent 30 years [33, 34], leading to rapid development in PAI [37].

1.2.2 Multiscale photoacoustic technology and main configurations

Currently, the spatial scale of PAI spans organelles, cells, tissues, and entire organs. Depending on the imaging mode, PAI primarily includes photoacoustic computed tomography (PAT/PACT), photoacoustic microscopy (PAM), and photoacoustic endoscopy (PAE), which have been extensively employed in biomedical research involving the thyroid, breast, cardiovascular system, central nervous system, dermatology, and hepatic diseases.

Photoacoustic computed tomography (PACT)

PACT employs wide-field spatial illumination of biological tissues, enabling imaging across a large field of view (FOV). Early PACT implementations utilized a single ultrasound transducer, acquiring signals through rotational scanning; however, the slow scanning speed significantly restricted its practical applications. Recent advancements have introduced ultrasound transducer arrays that simultaneously detect photoacoustic waves emitted from objects at multiple angles, facilitating rapid cross-sectional or volumetric imaging [38-40]. For accurate boundary representation in two-dimensional (2D) PACT, the detector array must encompass a view angle of at least π radians [41]. Ultrasound transducer arrays configured in various geometric arrangements, including linear [42], semicircular [43, 44], hemispherical [45], and full-ring [46, 47] shapes, have been successfully implemented and validated in both animal and clinical studies.

Imaging speed in PACT systems typically depends on the data acquisition hardware and the repetition frequency of the excitation laser. One classical PACT system, equipped with ring-shaped ultrasound transducer arrays consisting of 512 elements, can achieve imaging frame rates of up to 10-20 frames per second over a circular imaging area with a diameter of approximately 5 cm, offering lateral resolutions better than 200 μm [48]. However, the implementation of whole-body scanning remains dependent on stepwise motorized layer-by-layer acquisition, consequently constraining elevational resolution. To overcome this, researchers have developed a continuously rotating scanning PACT system for rapid multi-parametric monitoring within relatively large torso regions of small animals. In this innovative PACT configuration, a hemispherical ultrasonic transducer array performs continuous high-speed rotation, achieving complete 3D whole-body murine scans in merely 54 seconds while maintaining a spatial resolution of 172-212 μm [49]. Such PACT systems facilitate whole-body in-vivo imaging of small animals, clearly visualizing subcutaneous and visceral vasculature as well as cardiac pulsations. Furthermore, deep-brain imaging in mice

can be conducted, particularly when enhanced by specific contrast agents, enabling real-time monitoring of cerebral functions and dynamic metabolic processes. As illustrated in Figure 1-2, examples of ring-shaped, linear, and hemispherical ultrasound transducer arrays in PACT are presented.

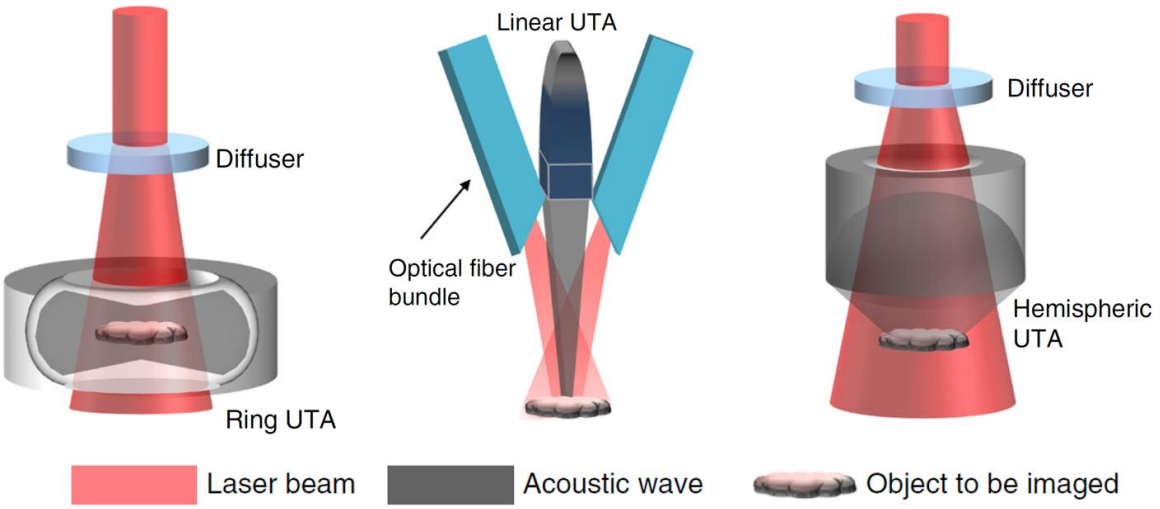

Figure 1-2. Schematic diagram of a ring, linear, and hemispherical array PACT system [50].

PACT provides unique advantages concerning imaging depth, speed, and resolution, making it an important complementary modality to existing clinical imaging techniques: (1) Compared with pure optical-imaging methods (such as fluorescence imaging), PACT maintains high spatial resolution in deep tissues. (2) Relative to US imaging, PACT offers abundant intrinsic and extrinsic optical contrast, fewer artifacts, and enhanced functional imaging specificity. (3) Unlike X-ray, CT, and PET, PACT utilizes non-ionizing radiation without radioactive exposure. (4) In comparison with MRI, laser-based PACT achieves higher spatiotemporal resolution at lower cost, coupled with targeted imaging and multi-wavelength spectral differentiation capabilities.

Photoacoustic microscopy (PAM)

Compared to PACT, PAM offers superior spatial resolution and can be categorized into optical-resolution PAM (OR-PAM) and acoustic-resolution PAM (AR-PAM). Achieving high acoustic resolution necessitates collecting high-frequency acoustic waves; however, these high-frequency waves experience significant attenuation in soft tissues. Within the optical quasi-ballistic regime (typically depths less than 1 mm in most biological tissues), light can be focused more tightly than ultrasound waves [51]. To eliminate the dependence of

resolution on acoustic frequency, OR-PAM employs spatially focused optical excitation, resulting in optical diffraction-limited lateral resolution [52]. Unlike X-ray imaging, OR-PAM can operate in either back-reflection mode [52-56] or transmission mode [57, 58], with representative configurations illustrated in Figure 1-3. In both setups, excitation light is focused onto the object to generate acoustic waves. To maximize detection sensitivity, a focused ultrasound transducer aligned confocally with the optical lens is used. The lateral resolution of OR-PAM is optically determined by the laser wavelength (λ) in vacuum and the numerical aperture (NA) of the lens: $R_{lateral} = \frac{0.5\lambda}{NA}$ [59].

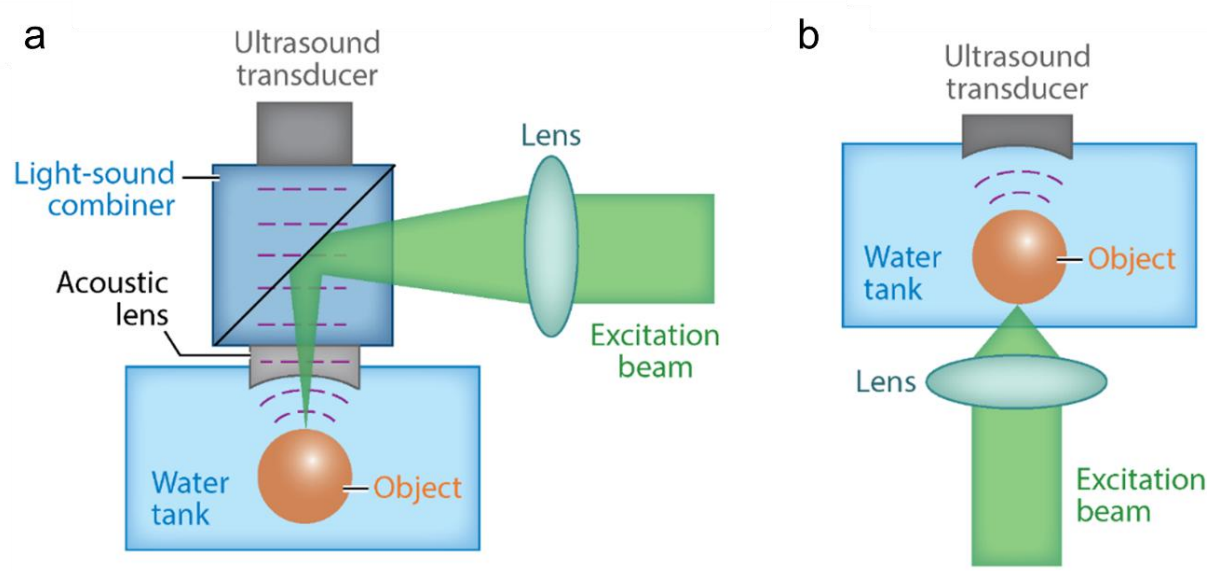

Figure 1-3. Schematic of a) a reflective and b) a transmissive OR-PAM system [59].

Volumetric imaging is typically performed by raster scanning the object in the lateral plane. Depth information is encoded in the travel time of the PA waves and can be reconstructed by the relationship $d = v_s t$, where v_s is the speed of sound in the medium, and t is the travel time of the acoustic wave to the ultrasound transducer. Since a single laser pulse is required at each scan position, the imaging speed of OR-PAM is limited by the laser repetition rate. With high repetition rate lasers (e.g., 100 kHz) and water-immersed MEMS scanning mirrors, B-scan imaging rates up to 400 Hz within a 3 mm scanning range have been reported [55]. Additionally, researchers developed a head-mounted PAM system featuring 9 μm lateral resolution, 0.2 Hz imaging rate, and 1.2 mm scanning range [60]. Utilizing dual-wavelength excitation, this system achieves single-vessel resolution for recording cerebrovascular responses to external stimuli, thereby enabling monitoring of both physiological and

pathological neurovascular functions in freely moving animals. To simultaneously expand the scanning range while maintaining imaging speed, Lee *et al*. proposed a waterproof galvanometer scanner approach, achieving a scanning area of 9 × 14.5 mm², an A-line rate of 40 kHz, and a lateral resolution of 4.9 μm [61].

OR-PAM operates within optical ballistic or quasi-ballistic conditions. Due to optical scattering, OR-PAM's imaging depth in biological tissues is typically limited to approximately 1 mm, beyond which lateral resolution rapidly deteriorates [62]. Compared to conventional optical microscopy techniques, the advantage of OR-PAM lies in its ability to provide high-contrast imaging of endogenous chromophores without staining, enabling label-free in vivo imaging of biological tissues or cells.

In contrast to OR-PAM, AR-PAM illuminates a relatively large area rather than focusing the light on an optical diffraction-limited spot. Consequently, AR-PAM allows higher laser energy levels under laser safety regulations compared to OR-PAM, increasing photon penetration depth. The lateral and axial resolutions of AR-PAM are acoustically limited. For a focused ultrasound transducer with aperture D and focal length l, the lateral resolution is calculated as: $R_{lateral} = 0.71\lambda_0 \frac{l}{D/2}$ [59], where λ_0 is the acoustic wavelength. Unlike OR-PAM, AR-PAM operates effectively within optical diffusion regimes, with achievable imaging depths scaling significantly with resolution and dependent on the ultrasound transducer's central frequency and bandwidth. For example, lateral resolution of 53 μm and an axial resolution of 18 μm at 1.8 mm depth using a 75 MHz transducer [63], lateral resolutions of 44 μm at 4.8 mm depth using a 50 MHz ultrasound transducer [64], and 560 μm at 38 mm depth using a 5 MHz ultrasound transducer [65] have been reported.

Photoacoustic endoscopy (PAE)

PAE is a variant of PAT that integrates optical and acoustic components into compact probes, enabling imaging of internal organ cavities via circumferential scanning. Conventional video endoscopy is limited to visualizing superficial morphological changes on tissue surfaces. PAE has emerged as a complementary modality for intracavitary disease detection by capturing ultrasound waves generated through laser absorption, which employs miniaturized flexible probes to perform minimally invasive imaging of deep internal cavities in humans and animals, including the esophagus [66], gastrointestinal tract [67], urinary tract [68], and vagina [69]. This technique provides high-resolution imaging through focused scanning of combined laser-ultrasound beams (Figure 1-4a).

Traditional PAE systems utilize focused piezoelectric transducers to detect laser-induced ultrasound signals. However, the inherent bulkiness of these transducers necessitates larger endoscope dimensions, restricting clinical application to anatomically wider lumens such as the esophagus and vagina. Recent advancements in fiber-optic ultrasound transducers have enabled substantial miniaturization while maintaining sufficient detection sensitivity [67]. These next-generation transducers now permit PAE deployment in smaller anatomical structures including blood vessels, urinary tracts, and finer regions of the gastrointestinal system. Furthermore, owing to its intrinsic accessibility to internal organs, PAE can be synergistically integrated with therapeutic modalities—including laser ablation [70], radiofrequency ablation [71], and ultrasound ablation [72]—to achieve simultaneous imaging-guided treatment (Figure 1-4b).

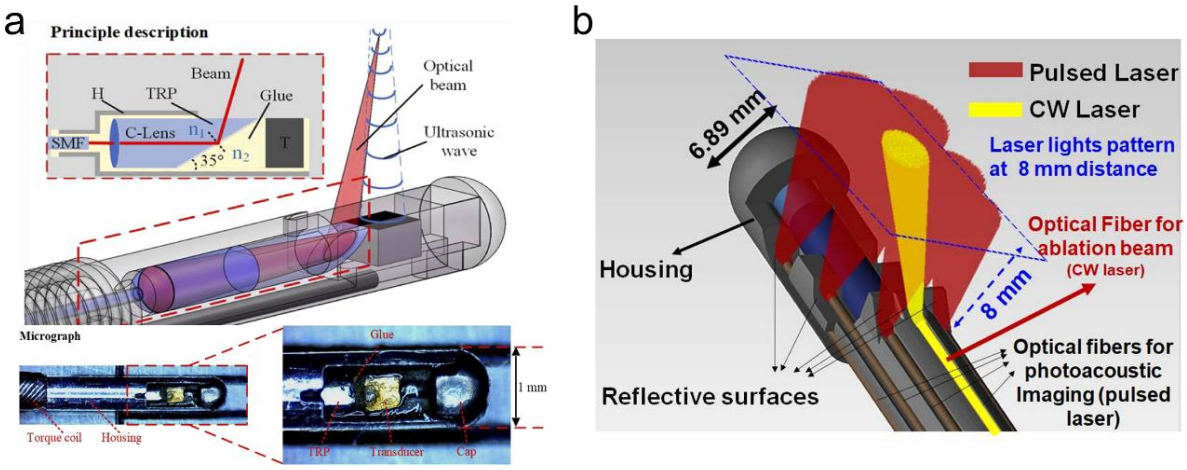

Figure 1-4. a) A Design and assembly PAE probe [73] and b) the schematic of a miniaturized catheter-integrated PA ablation system [70].

In summary, imaging characteristics of these photoacoustic schemes are summarized in Table 1.

Table 1. Multiscale photoacoustic imaging [59]

Methodology	**PACT**	**OR-PAM**	**AR-PAM**	**PAE**
Lateral resolution	Acoustic	Optical	Acoustic	Acoustic
Axial resolution	Acoustic	Acoustic	Acoustic	Acoustic

Depth limit	Optical diffusion (< 70 mm)	Optical ballistics (~ 1 mm)	Optical diffusion (< 3 mm)	Optical diffusion (< 7 mm)
Scanning mode	Parallel	Raster scanning	Raster scanning	Circumferential sector scanning

1.2.3 Functional photoacoustic imaging

Biological tissues inherently contain numerous endogenous chromophores exhibiting characteristic optical absorption spectra (Figure 1-5). Endogenous absorbers in biological tissues can be divided into two groups based on their primary absorption wavelengths. One group absorbs in the ultraviolet (UV, 180 nm to 400 nm) and visible (UV-VIS, 400 nm to 700 nm) regions. The main absorbers for PAI in this group include DNA/RNA [74, 75], cytochromes [76, 77], myoglobin [76], hemoglobin [78], and melanin [79]. DNA and RNA are primarily absorbed in the UV region. Ultraviolet photoacoustic microscopy (UVPAM) enables non-invasive in vivo imaging of cell nuclei without staining by exciting unlabeled DNA and RNA at 266 nm. Since cancer cells often exhibit abnormal cell density and nuclear morphology, UVPAM can be used for early cancer diagnosis and intraoperative detection of cancer cells [80]. UVPAM requires careful control to prevent potential cellular damage due to excessive UV exposure, such as direct and indirect DNA breaks [81]. PAI of cell nuclei via DNA/RNA absorption and of cytoplasm via cytochrome absorption provides in vivo label-free imaging equivalent to traditional ex vivo imaging using hematoxylin and eosin staining, where hematoxylin stains the nuclei and eosin stains the cytoplasm.

As the most abundant protein in blood and the primary oxygen carrier, imaging hemoglobin with PAM can yield numerous hemodynamic parameters, such as total hemoglobin concentration, oxygen saturation, blood flow speed, and oxygen metabolic rate [78]. In the visible spectrum, hemoglobin absorption is much stronger than other absorbers like water and lipids, enabling high-sensitivity PAI of microvasculature and even single red blood cells, with a signal-to-noise ratio (SNR) exceeding 40 dB. Functional and metabolic PAI of the microvascular system aids in comprehensively understanding the tumor microenvironment, such as angiogenesis, hypoxia, and metabolic hyperactivity [78, 82]. Besides cancer, PAM has been used to image microvascular damage caused by diabetes [83].

Melanin is the primary light-absorbing molecule in melanoma, the most lethal form of skin cancer [84]. Due to its extremely high optical absorption in the UV-VIS region (e.g., ~10,000

times that of water and ~100 times that of oxyhemoglobin at 700 nm), melanin in melanoma is an ideal contrast agent for early melanoma detection with PAM. In animals, PAM has been successfully applied for non-invasive in vivo detection of circulating melanoma cells in the bloodstream and chronic monitoring of melanoma growth, with a penetration depth of up to 4 mm and a SNR of 30 dB [79, 85-88]. In tissue engineering, the spatial distribution of melanoma cells in scaffolds has also been imaged using PAM [89]. Beyond melanoma detection, melanin provides good contrast for PAI of the retinal pigment epithelium (RPE) in rat eyes, with a SNR of 23 dB. More importantly, melanin's high optical absorption allows a laser incident energy density of 0.1 μJ/cm², below the safety threshold for ocular imaging (0.5 μJ/cm²). Since RPE plays a crucial role in vision, PAM holds great potential for basic research and clinical diagnosis of ocular diseases, such as age-related macular degeneration [90, 91].

The other group absorbs in the NIR region (700 nm to 1400 nm), with lipids [57, 92, 93], water [94], and glucose [95] being the main absorbers for PAI. Abnormal concentrations of lipids, water, or glucose often indicate unhealthy conditions. For example, lipids are common components of atherosclerotic plaques, whose location and size are closely related to the progression of atherosclerosis [96]. Using NIR excitation, PAM can image lipids and water at relatively deep tissue depths with high resolution. Blood glucose levels are standard indicators for diabetes diagnosis and treatment evaluation, and PAI of glucose concentration has been demonstrated both in vitro and in humans, showing good correlation with clinical measurements.

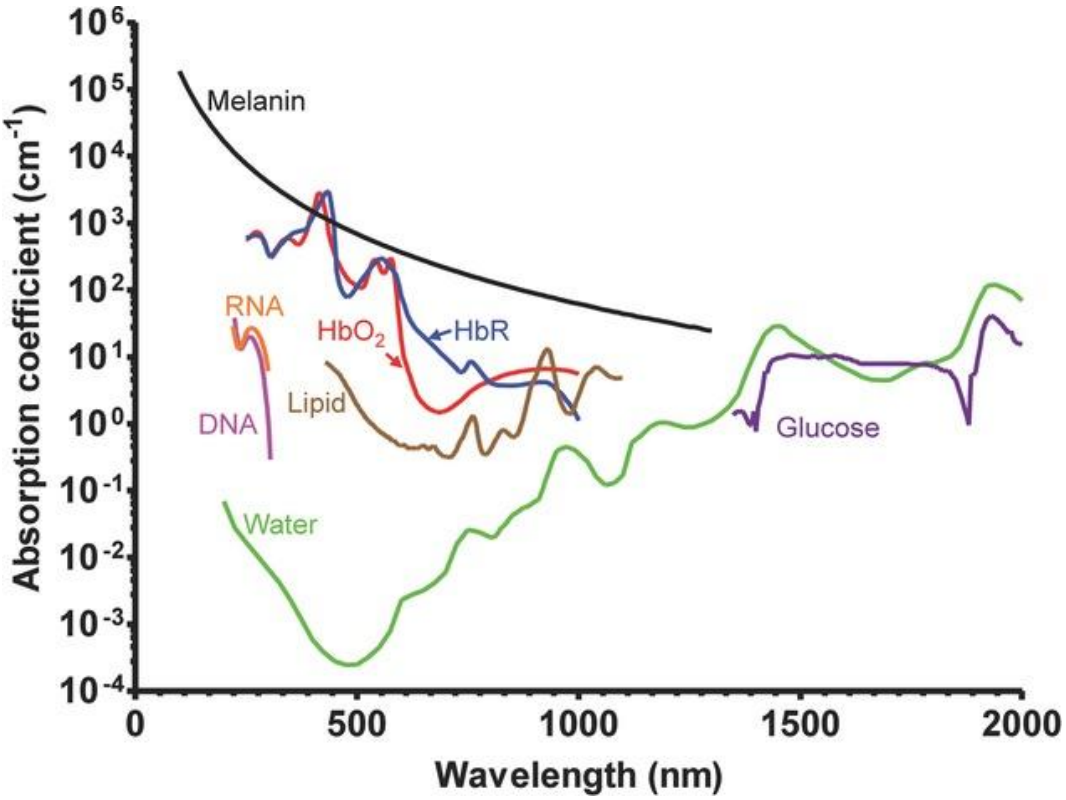

Figure 1-5. Absorption spectra of major endogenous contrast agents in biological tissues [97]. Specifically include: oxyhemoglobin (HbO_2), red line (150 g/L in blood); deoxyhemoglobin (HbR), blue line (150 g/L in blood); lipid, brown line (20% volume in tissue); water, green line (80% volume in tissue); deoxyribonucleic acid (DNA), magenta line (1 g/L in cell nuclei); ribonucleic acid (RNA), orange line (1 g/L in cell nuclei); melanin, black line (average 14.3 g/L in human skin); glucose, purple line (720 mg/L in blood).

Moreover, PAI exhibits superior morphological resolution and sensitivity, and when enhanced by exogenous contrast agents, it can perform more sophisticated functional imaging, thus playing an essential role in both fundamental biomedical research and clinical investigations. Exogenous contrast agents can be synthesized and tailored according to specific requirements, and when combined with molecular targeting strategies, they facilitate targeted imaging of lesions, significantly aiding disease diagnosis and therapeutic monitoring. Notably, FDA-approved agents such as indocyanine green (ICG) and methylene blue have already been successfully applied in clinical settings [98, 99]. In addition, novel nanomaterials, such as nanoparticles, semiconducting polymers, and carbon nanostructures, have been developed to provide enhanced signals with tunable optical properties and biocompatibility. While novel dyes with enhanced capabilities, such as activatable or

environment-sensitive dyes [100, 101], are being developed to offer higher specificity, improved SNR, and the ability to visualize dynamic biological processes. Meanwhile, novel transgenic proteins with high absorption in the NIR regime are being widely screened, with many promising candidates identified for future optimization.

Activatable probes, which respond to specific biomolecular cues like enzymatic activity or redox conditions, have emerged as powerful molecular tracers for functional imaging of neural activities and diseases such as cancer and inflammation. Hybrid agents combining diagnostic and therapeutic functions, often referred to as theranostic agents, have also gained attention for their ability to integrate real-time monitoring with treatment. Advances in molecular engineering have enabled the development of targeted tracers that bind to specific biomarkers with high precision, facilitating the detection of early-stage pathologies and providing insights into dynamic biological processes at molecular and cellular levels. Similar to photoswitchable fluorophores in optical super-resolution microscopy, switchable PA tracers—whether synthesized molecules or transgenic proteins—have demonstrated superior advantages in extracting extremely weak PA signals and have shown notable progress in recent studies [102, 103]. These developments have significantly broadened the potential of PA imaging, enabling it to transition from a structural imaging modality to a versatile platform for molecular and functional imaging.

1.3 State of the art

1.3.1 Brain function mapping

Given its deep tissue penetration and high spatial resolution, PAI emerges as an outstanding tool for brain functional mapping. Specifically, PACT utilizes uniform illumination of biological tissues with pulsed excitation light and collects ultrasound signals in parallel through linear, circular, or hemispherical ultrasonic transducer arrays. This approach enables whole-brain imaging in small animals and facilitates the observation of physiological dynamics.

Research teams from institutions such as Washington University and the California Institute of Technology (Caltech) have achieved notable advancements in PAT. For instance, in 2003, PAT successfully demonstrated structural and functional imaging of the living rat brain, depicting cerebral structures and cortical hemodynamic changes [37]. In 2013, this technique was further developed to image the mouse brain, providing noninvasive, large field-of-view

(FOV) imaging with high spatial resolution [104]. In 2015, genetically encoded NIR photoswitchable probes (BphP1) were integrated with PAT to investigate brain tumors, achieving improved sensitivity, reduced background signals, deeper penetration, and approximately 100 μm resolution at depths approaching 10 mm [105]. In 2017, single-impulse panoramic PACT (SIP-PACT) was developed, enabling dynamic, whole-body imaging of small animals, including brain structures, revealing detailed anatomical and functional information [48]. Subsequently, in 2021, a hemispherical ultrasonic transducer array surrounding the human head enabled PACT with a 10 cm FOV achieving spatial and temporal resolutions of 350 μm and 2 s, respectively. This approach successfully enabled functional PACT imaging in patients who had undergone hemicraniectomy [106]. Additionally, the University of Florida developed a wearable miniature PAT system capable of achieving 200 μm spatial resolution, allowing real-time monitoring of hemodynamics in the primary visual cortex of rats during visual stimulation tasks [107-109]. The ETH Zurich team demonstrated functional photoacoustic neuroimaging both *ex vivo* and noninvasively in vivo using genetically encoded calcium indicators (GCaMP6f). This method enabled rapid, high-resolution imaging of neuronal activity, hemodynamic responses, and fast calcium signaling throughout the entire mouse brain [110].

Furthermore, PAM, characterized by higher spatial resolution through confocal detection, provides detailed imaging of cerebral blood supply, oxygenation, and metabolic activity, making it a superior imaging technique for investigating cortical neuronal activity, assessing brain injuries, and quantitatively evaluating brain functions. In 2015, researchers introduced a high-speed functional PAM capable of three-dimensional, high-resolution brain imaging in mice with an A-line rate of 100 kHz, enabling visualization of capillary-level cerebral vasculature, oxygenation, blood flow, and oxygen metabolism under both resting and stimulated conditions [111]. In 2022, Duke University proposed an ultrafast functional PAM (UFF-PAM) system capable of imaging whole-brain hemodynamics and oxygenation with a volumetric imaging speed of 2 Hz and spatial resolution of approximately 10 μm across a 11×7.5×1.5 mm^3 FOV. This system successfully captured dynamic hemodynamic responses during hypoxic and stroke-like conditions [112]. Additionally, researchers from the University of Virginia developed an awake PAM method by positioning mouse heads on air-suspended balls, enabling cerebral imaging in conscious animals. This innovative approach allows for comparative studies of cerebral hemodynamics between anesthetized and awake states, long-term monitoring, and investigations into cerebrovascular changes in obesity

models [113-116]. At Southern University of Science and Technology, an ultrafast, portable, high-resolution PAM system was used to study cerebrovascular structures and functional responses in rhesus monkeys, capturing vascular dilation and contraction under hypoxic conditions [117], as well as neurovascular coupling responses induced by electrical stimulation [118]. Table 2 summarizes the comparison of parameters among commonly used brain functional imaging modalities.

Table 2. Comparison of brain imaging technologies

Imaging methods	**Field of view**	**Resolution**	**Functional information**	**Speed**
CT	Whole-brain	Millimeter-scale	/	Slow
fMRI	Whole-brain	Millimeter-scale	Structure and anaerobic hemoglobin	Slow
OCT	Whole-brain in small animal	Micrometer-scale	Structure, unlabeled blood oxygen and flow rate	Relatively fast
2PM	Millimeter range	Micrometer-scale	Structure and function, fluorescent labeling required, slower functional imaging	Moderate
PACT	Whole-brain in small animal	Hundred micrometer-scale	Structure, oxygenation and metabolic function, specific probes respond to specific functions	Rapid
PAM	Millimeter range	Micrometer-scale	Structure, flow rate and blood oxygen without labeling	Relatively fast

1.3.2 Liver diseases detection and monitoring

PAI holds significant potential for applications in the detection, diagnosis, treatment monitoring, and surgical guidance of hepatocellular carcinoma (HCC), providing rich functional and molecular information to aid clinical decision-making. For instance, PAI can offer high-contrast and high-resolution images, facilitating the early detection of liver cancer. On one hand, HCC is often associated with abnormal angiogenesis. PAI can assess the

vascular architecture and oxygenation status of tumors by detecting the absorption characteristics of hemoglobin, thereby providing insights on tumor growth and invasion [119, 120]. This capability aids in distinguishing tumor tissues from normal liver tissues. On the other hand, by incorporating targeted molecular probes, it can be used to detect specific molecular markers associated with liver cancer [121, 122]. This approach not only enhances the specificity and sensitivity of imaging but also contributes to early cancer screening and the development of personalized therapeutic strategies. During the treatment of HCC, photodynamic and photothermal therapies are commonly employed. When combined with targeted drugs, PAI not only exerts therapeutic purposes but also enables real-time monitoring of treatment responses [123-125]. In surgical interventions for liver cancer, it can provide real-time tissue contrast, assisting surgeons in accurately identifying and excising tumor tissues while preserving as much healthy liver tissue as possible [126].

Assessing liver function reserve (LFR) is a crucial parameter for numerous diseases. Variations in ICG concentration serve as a classical indicator of LFR, given its selective hepatic uptake and clearance. For instance, in liver resection surgery, LFR assessment aids in determining the extent of resection and predicting clinical outcomes. Luo, Yan et al. proposed using a real-time PACT system to monitor ICG concentration variations in normal and partially hepatectomized (PH) rabbits to evaluate LFR. After ICG injection, the temporal PA changes in ICG concentration closely matched invasive spectrophotometric measurements. Additionally, differences in ICG clearance rates were observed between the two groups [127]. Furthermore, in various chronic diseases such as hepatitis, liver fibrosis [128], and alcoholic fatty liver disease [129], photoacoustic monitoring of ICG metabolism and clearance curves is commonly used to assess liver function. This study highlights the clinical potential of PACT for noninvasive, in vivo LFR assessment.

Furthermore, liver has a rich blood supply and a complex network of microvasculature, which often undergoes changes in vascular structure and blood oxygenation under pathological conditions. Therefore, PAM can effectively identify these changes and aid in the diagnosis and monitoring of diseases [130, 131].

1.4 Research objectives and thesis structure

1.4.1 Research objectives

Brain voltage visualization

In neuroscience research, PAI has demonstrated prominent advantages, including label-free detection, high spatial resolution, and excellent imaging contrast, thereby yielding significant advances in brain imaging. However, current experiments predominantly infer neuronal activity indirectly via neurovascular coupling, without directly capturing true neurophysiological processes. Alternative approaches depend on calcium-ion responses as proxies for neuronal electrical activity, but these methods suffer from limitations associated with voltage-sensitive indicators' sensitivity and photostability, while genetically encoded probes face ethical barriers limiting human applicability. Hence, achieving *in vivo*, whole-brain monitoring of neuronal electrical activity with high spatiotemporal accuracy is crucial. Such capabilities hold profound significance for pathological research, diagnosis, localization of epileptic foci, and surgical navigation in diseases like epilepsy.

Liver fibrosis detection

Chronic liver diseases, if not detected and intervened at early stages, may progress into irreversible critical conditions such as cirrhosis and HCC, posing significant threats to life expectancy. Notably, hepatopathies account for over 15% of disease prevalence in China, with approximately 25%-40% of cases progressing to varying degrees of hepatic fibrosis. Conventional imaging modalities exhibit inherent limitations in early hepatic disease screening due to their non-specific characteristics and insufficient sensitivity, thereby restricting early diagnostic efficacy. This underscores the imperative need to develop novel early diagnostic and monitoring modalities.

As previously mentioned, the liver serves as the hemodynamic exchange hub with abundant capillary structures, where incipient pathological alterations often manifest as subtle microarchitectural changes that are prone to oversight. PAI demonstrates distinct advantages in label-free vascular angiography, while its thermoelastic effects under PA phenomena provide a physical foundation for biomechanical characterization. The integration of vascular imaging and biomechanical quantification through photoacoustic technology establishes a novel paradigm for hepatic disease surveillance. This multimodal approach promises to deliver quantitative diagnostic tools for monitoring chronic liver disease progression,

potentially revolutionizing early-stage pathological assessment through synergistic analysis of microvascular remodeling and tissue viscoelastic alterations.

1.4.2 Thesis structure

This thesis comprehensively reviews the advantages and limitations of current radiological diagnostic modalities, while highlighting the principles, merits, and application contexts of PAI. We demonstrate PAI's potential in cerebral functional mapping and hepatological disease diagnosis/monitoring. To address existing challenges, we propose two innovative paradigms: 1) a wide-field whole-brain imaging modality for direct electrophysiological monitoring in epilepsy, validated for real-time signal tracking and epileptogenic zone localization (Chapters 2-4); 2) a high-resolution photoacoustic microscopic elastography (PAEM) modality enabling multiparametric assessment of hepatic fibrosis progression through lobular vascular architecture analysis and time-of-flight (ToF)-based biomechanical quantification (Chapters 5-6). The principal contributions are structured as follows:

Chapter 2 systematically validates voltage-sensitive dyes' (VSD) optical response at cellular levels. We first elucidate epileptogenesis mechanisms and conventional VSD applications, followed by detailed cellular experimental protocols. Results demonstrate synchronized fluorescence-photoacoustic dual-modal responses to membrane potential fluctuations, with rigorous mechanistic analysis confirming the operational principles of selected DiSC3(5) VSD.

Chapter 3 employs in-vivo murine fluorescence imaging to verify cerebral electrophysiological responses in epileptic models. Comprehensive methodologies encompass animal preparation, drug-induced epilepsy model, and signal acquisition/analysis. The in-vivo fluorescence dynamics corroborate cellular-level observations, establishing translational consistency across scales. But the poor spatial-temporal resolution motivates the subsequent rapid PA brain mapping approach.

Chapter 4 details a custom PA system configuration (resolution: ~110 μm; FOV: 5.5 cm; depth: 4 mm) for whole-brain vascular mapping. We demonstrate noninvasive monitoring of epileptiform discharges and precise localization of hyperexcitable foci through spatiotemporal correlation of photoacoustic signals with seizure events, suggesting potential for intraoperative navigation.

Chapter 5 presents an optimized PAM system for hepatic lobular microarchitecture characterization. While high-resolution vascular imaging enables early fibrosis screening

(significant difference in 1 to 3-week fibrotic models), structural parameters alone prove insufficient for advanced staging. This limitation motivates the subsequent biomechanical approach.

Chapter 6 introduces ToF-based PAEM for quantitative stiffness mapping throughout fibrotic progression. Experimental validation reveals significant hepatic stiffness differentiation at initial fibrosis stage (1-week model), surpassing shear-wave elastography (SWE) in sensitivity. Progressive stiffness escalation and clear tumor demarcation in hepatocellular carcinoma models confirm the technique's diagnostic versatility.

Chapter 7 critically evaluates the clinical implications and technical challenges of the proposed methodologies, outlining future optimization strategies for translational implementation. We further discuss how these advancements may reshape research paradigms in neuroimaging and hepatology, providing actionable roadmap for next generation theragnostic development.

This thesis establishes a methodological framework bridging electrophysiological monitoring and biomechanical quantification through photoacoustic innovations, offering novel solutions for precision medicine in neurological and hepatic disorders.

Chapter 2 Cellular-Level Voltage Response Validation

Chapters 2-4 are reproduced with some adaptations from published paper "Weiran Pang, Bowen Zhu, Honghui Li, Yingying Zhou, Chi Man Woo, Xiazi Huang, Tianting Zhong, Hsuan Lo, Laiyou Wang, Puxiang Lai, and Liming Nie*, "Direct Monitoring of Whole-Brain Electrodynamics via High-Spatiotemporal-Resolution Photoacoustics with Voltage-Sensitive Dye". Laser & Photonics Reviews, 18(10): 2400165 (2024). The contributions of authors are as follows: W. P., L. N. and P. L. proposed the idea and designed the experiments. W. P. performed the experiments, collected raw data, analyzed the data, prepared the figures for the manuscript, and wrote the original manuscript. B. Z. and H. L. helped conduct part of the in vitro experiments. Y. Z., C. M. W., X. H., and T. Z. helped with the result discussion, text revision, and formatting. H. L. and L. W. supported with neurological advice. L. N. and P. L. funded and supervised the project. All authors were involved in the analysis of the results and manuscript revision.*

In the following three chapters, a robust voltage-sensitive dye (VSD)-based whole-field photoacoustic brain detection (WF-PABD) platform is proposed, enabling direct evaluation of voltage dynamics across the whole brain, forming as PA-VSD. WF-PABD is equipped with a 512-element ring-array ultrasound detector capable of 360-degree scanning, providing a large FOV (~5 cm), high spatial resolution (~110 μm), and rapid imaging acquisition. The proposed VSD remained ~75% photostability after 30-mins laser exposure, much greater than most calcium sensors. The optical voltage-response mechanisms are validated and the capability of PA-VSD to directly screen seizures is established. It has been demonstrated that by investigating connectivity among different brain regions, it allows to identify the precise location of active epileptic foci as well as the electrical conduction pathways and their directionality through fast temporal visualization. In summary, this study not only addresses the need for non-invasive, high-resolution, long-term, and direct monitoring of brain voltage but also empowers exciting venues for PA applications in neuroscience.

2.1 Introduction to epilepsy and voltage-sensitive indicators

Understanding brain function and diseases requires studying electrical signal communication across vast populations of neurons in diverse regions. A comprehensive view of the time-varying whole-brain activity at multiple spatial scales and depths is essential. Current research focuses on abnormal neuronal discharges in central nervous system disorders such as epilepsy. Clinically, seizures are characterized by aberrant synchronized firing of hyperexcitable cortical neuron populations [132], which can be life-threatening in severe cases. Prolonged monitoring of whole-brain voltage dynamics could therefore advance assessment of disease progression and enable precise, timely intervention.

To investigate spontaneous neurotransmitter events driven by voltage fluctuations in pathophysiological states, membrane potential studies via electrical recording or optical imaging with voltage-sensitive dyes (VSDs) have been developed [133-135]. The patch-clamp technique [136] remains the gold standard for accurate *in vitro* cell membrane potential detection but is challenging to implement *in vivo*. Electroencephalography (EEG) [137] is widely used to track the brain electrical activity. However, its spatial resolution is limited by electrode number and distribution. Recently, super-resolution fluorescence (FL) microscopy (particularly two-photon microscopy, 2PM) combined with near-infrared genetically encoded calcium indicators (GECIs) has merged as a preferred method for visualizing brain voltage. This approach enables high-resolution action potential measurements in conscious animals [138-142], but is restricted to narrow fields of view (FOV) at superficial depths, e.g., imaging dozens of neurons within hundreds of microns [143]. Due to light scattering in overlying tissues, optical methods (including 2PM) suffer from limited FOV and shallow penetration depth (~1.5 mm even with multiphoton techniques [142]). Thus, the need for wide-field, deep-penetrating, high-resolution, and high-speed monitoring of neural voltage dynamics remains unmet.

PAI, also termed as optoacoustic imaging, is an emerging hybrid imaging technique that can noninvasively map tissue with high specificity and micron-scale resolution at greater depths. It employs a pulsed laser as the excitation source and gathers the ultrasonic response to reconstruct the light absorption maps of structural and functional information of the target tissue, well eliminating the negative effects of light scattering within the tissue [37, 128, 144-149]. Its vascular specificity supports neurovascular coupling for neural voltage imaging, as evidenced in recent studies [118, 150]. However, these typically infer neuron activity indirectly through vascular or blood oxygenation fluctuations. In 2019, Sven Gottschalk et al.

combined GCaMP6-family GECI with PAI to probe deep-tissue voltage dynamics, opening new venues towards rapid, high-resolution whole-brain action potential monitoring [110]. Nevertheless, GCaMP's poor photostability limits its utility for extended recordings (usually >30 minutes) [151, 152], and its cell-type specificity restricts response scope. Ethical consideration regarding genetic encoding further constrains clinical translation of GECI-based approaches.

In addition to the ethical concerns associated with GECIs and their indirect measurement mechanism, genetically encoded voltage indicators (GEVIs) such as ArcLight also present similar ethical considerations. In contrast, alternative VSDs that directly detect membrane potential, such as DiBAC4(3), DiIC1(5), IR-780 and DiSC3(5), exhibit varying sensitivities. Based on our ex-vivo assays, DiSC3(5) demonstrates superior performance, characterized by a high signal change ratio ($\Delta A/A_0$) and relatively low photobleaching. Furthermore, its excitation wavelength at 656 nm falls within a spectral range of minimal hemoglobin absorption, making it particularly suitable for in-vivo voltage monitoring applications.

Table 3. Commonly used voltage-sensing indicators

Indicators	**Sensing target**	**Voltage-sensitive principle**	**Voltage sensitivity ($\Delta F/F_0$)**	**Voltage sensitivity ($\Delta A/A_0$)**	**Wavelength**	**Toxicity**	**Photobleaching (Time—Remain intensity)**	**Ethical risk**
GCaMP6f/7/8 [110]	Ca^{2+} (Indirect)	Ca^{2+}-induced GFP conformation change	~ 2-4%	~ 6-8%	488 nm	Safe	12 mins—60%	√
ArcLight [153]	MP	pH-sensitive GFP variant	~35% (High)	N/A	488 nm	Safe	2 s —94%	√
DiBAC4(3) [154]	MP	Anion accumulates (positive interior)	~ 5%	N/A	490 nm	Moderate safe	Undetected	×
DiIC1(5) [155]	MP	Cation accumulates (negative interior)	~ 14%	~ 12%	638 nm	Moderate safe	Undetected	×
IR780 [156]	MP	Cation accumulates (negative interior)	~ 13%	~ 5%	780 nm	Moderate safe	Undetected	×
DiSC3(5) [31]	MP	Cation accumulates (negative interior)	~ 15%	~ 19%	656 nm	Moderate safe	30 mins—75%	×

Notes: MP: Membrane potential; $\Delta F/F_0$: Fluorescence change rate; $\Delta A/A_0$: Photoacoustic change rate; The values were obtained from references or our cell experiments.

This chapter proposes a novel strategy employing a photostable VSD for direct voltage dynamics monitoring. We utilize carbocyanine DiSC3(5), 3-propyl-2-(5-(3-propyl)-2(3H)-benzothiazolidene-1,3-pentadienyl), previously applied to mitochondrial membrane potential assessment [157, 158]. Following in-vitro cell experiments, we verify the optical response characteristics and mechanistic basis of this VSD. First, we detail methods and results from cellular studies, including characterization of DiSC3(5) properties, such as optical absorption spectra, cytotoxicity, and fluorescence. Next, we modulate cellular resting membrane potentials by varying extracellular potassium concentrations to simulate graded depolarization, monitoring concomitant changes in DiSC3(5) fluorescence and photoacoustic signals. Finally, we propose a conceptual mechanism for the probe's voltage sensitivity.

2.2 Methodologies for cellular imaging

2.2.1 *Voltage-sensitive dye preparation*

The molecular weight of DiSC3(5) is 546.53 and the powder was dissolved in DMSO at a concentration of 10 mM mother solution for use, then diluted with ultrapure water to a concentration of 100 μM for in-vivo animal brain experiments and diluted in cell medium at a concentration of 10 μM for in-vitro cell experiments for daily use only. To prevent bleaching of the dye, the dye preparation was carried out under low-light conditions and the solution container was covered with aluminum foil.

2.2.2 Characterization of DiSC3(5)

Microplate readers (Spark, Tecan Austria GmbH, Austria) were used to measure the absorbance spectra. A standard curve was constructed with eight different concentrations of DiSC3(5) to assess the absorption curves spanning from 450 to 800 nm.

2.2.3 In vitro cell experiments

In the cell experiments, HEK293T and Neuro-2a (N2a) cells were used. HEK293T were cultured in basic medium (DMEM + 10% FBS + 1% P/S), and N2a were cultured in their special medium (MEM + 10% FBS + 1% P/S) at temperature of 37℃, humidity of 25-65 RH, and CO_2 content of 5%.

In CCK8 assays, each well in a 96-well plate was seeded with about 2500 N2a cells respectively and 100 μL of standard medium was added and then cultured for 4 h. The Control group did not add DiSC3(5), and the other 7 groups were added with 0.1, 0.5, 1, 1.5, 2, 3, and 5 μM DiSC3(5), respectively. The incubation continued for 24 h, and the supernatant was removed, and then added 100 μL of 10% CCK8 reagent. Then continued incubation for 2 h. The absorption values were detected under the Microplate reader (excitation: 450 nm). There were 8 parallel samples in each group, two samples with large differences were removed, and the mean and SE of mean were calculated for 6 samples.

Six concentration gradients of K+ buffers were prepared, each representing a change in cell membrane potential of 0, 20, 40, 60, 80, and 100 mV calculated by the Nernst equation. This buffer was prepared by mixing 50 mM Hanks Balanced Salt Solution (137.93 mM NaCl, 5.33 mM KCl, 4.17 mM $NaHCO_3$, 0.441 mM KH_2PO_4, 0.338 mM Na_2HPO_4, 5.56 mM D-Glucose, pH of 7.1-7.5) and 20 mM Hepes solution at a ratio of 3:2, and then adding KCl crystal to achieve K+ concentration of 5.7, 32.9, 64, 98, 137, and 492 mM, respectively.

In the quantitative experiment of cell membrane potential, HEK293T cells were cultured in 18 Wells (three rows and six columns) in a 96-well plate. 6.7 μL 3 μM DiSC3(5) was added into each well (total volume was 200 μL) for 40 mins of co-incubation, then the cell culture medium was removed and 200 μL of extracellular medium with different K+ concentrations was added into each column. Then added nothing to the first line, 5 μL 10 μM Valinomycin (Val) to the second line, and 5 μL 1 mM Gramicidin (Gra) to the third line and put them into the Microplate readers to measure the UV absorption curve.

2.2.4 Cell imaging

The same procedure was applied to the N2a FL experiment, but without Val and Gra, and eight parallel experimental groups were made. The 96-well plate was put into the IVIS Spectrum In vivo Imaging System (Perkin Elmer, USA) to measure the FL signal (excitation

of 640nm, emission of 680nm). The IVIS Spectrum software was used to circle the ROI and calculate the trend of the FL signal with the change of the membrane potential.

Photoacoustic microscopy (PAM) (G2 OR-PAM, INNO LASER, China) was used to measure the PA signal changes of DiSC3(5) in neuron N2a. On the day before the experiment, 1×10^6 N2a cells were grown in glass pe-tri culture dishes (6 dishes) with a bottom diameter of 90 mm. On the same day, 70 µL 10 µM DiSC3(5) was added to the culture medium (total volume was 7 mL) and incubated for 40 mins. Then, extracellular buffers with different K+ concentrations were respectively added into 6 culture dishes after the supernatant was sucked out. In PAM imaging, cell signals were obtained using a green laser at a wavelength of 532 nm and an energy of 0.26 mW with a range of 200 mV signal channels. The images are 900 µm × 900 µm in size, with a pixel spacing of 3 µm. All the images were reconstructed in MATLAB with our self-developed imaging algorithm.

2.3 Experimental results and discussion

DiSC3(5) has an absorption peak at 656 nm (Figure 2-1a), and the absorption increases almost linearly (R^2=0.99957) with the concentration (Figure 2-1b). We discovered that DiSC3(5) demonstrated both excellent fluorescence and photoacoustic signaling capabilities, so it is a well-fitted medium for monitoring voltage via fluorescence and photoacoustic performance.

Then, cell Counting Kit-8 (CCK8) was used for cell proliferation and toxicity research to confirm its safety. The results showed that with the increase of concentration, DiSC3(5) showed weak toxicity, but still ensured more than 85% of cell viability, which indicated that it was biosafe at the highest blood-level concentration employed in *in vivo* trials (Figure 2-1c). Hence, there was no toxicity concerns in cellular as well as in-vivo animal experiments since the concentration of DiSC3(5) that diffuses to the brain will be even lower.

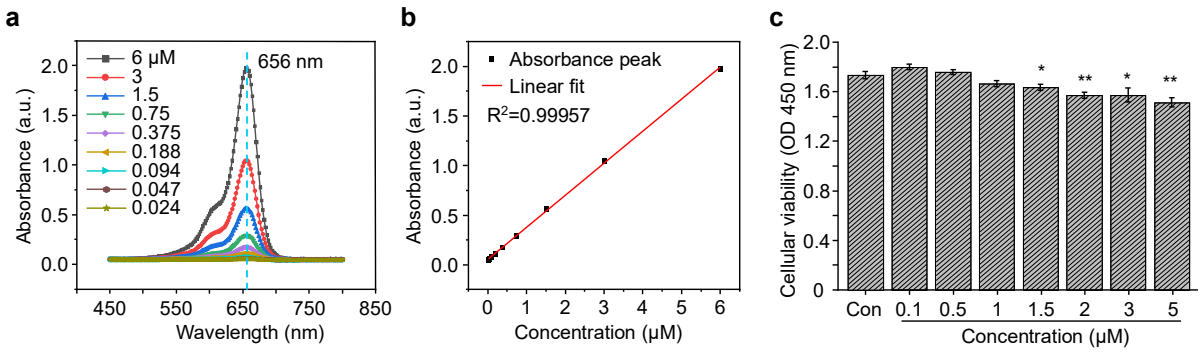

Figure 2-1. The optical property of DiSC3(5). a) Absorption spectra of DiSC3(5). b) Absorption calibration curve as a function of DiSC3(5) concentration. c) Cell proliferation and toxicity test of DiSC3(5). The error bar is standard error of mean (SEM). Con: Control group.

Before the cellular experiments, flow cytometry assays were carried out to confirm that DiSC3(5) had the capacity to actively penetrate neuronal cell membranes and generate fluorescent signals upon entrance into cells. Here, Neuro-2a (N2a) cells were employed. The results revealed that the DiSC3(5) group (Figure 2-2a) had a very strong FL signal while the control group (Figure 2-2b, without the dye) had none, showing that the co-cultured DiSC3(5)-containing cells were the sources of the main FL signal, but not the free dyes.

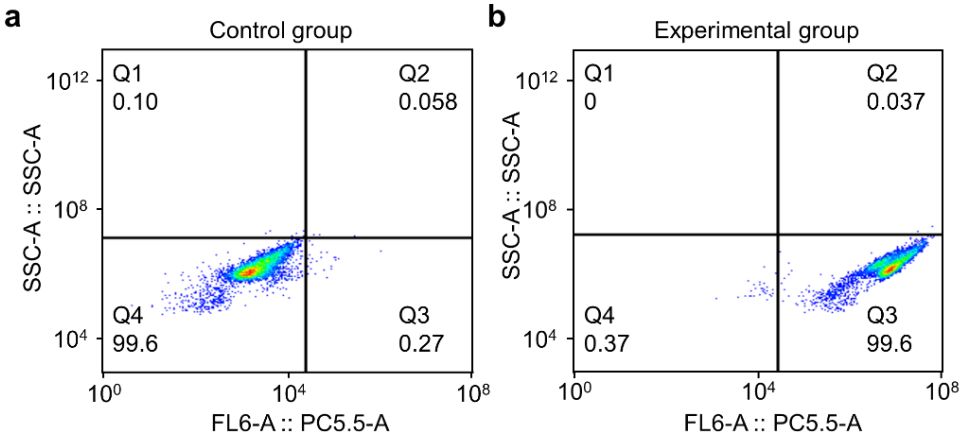

Figure 2-2. Fluorescent capability of DiSC3(5) in cellular level. a) Flow cytometry of neuronal cells without DiSC3(5). b) Flow cytometry of neuronal cells with DiSC3(5).

To test the ability of DiSC3(5) to sense voltage, an identical number of HEK-293T cells were seeded in a 96-well plate. After one day of culture, the wells were divided into 4 groups (each column acted as one group) and then filled with extracellular medium with 3, 1.5, 0.75, and 0.375 μM DiSC3(5) solution, respectively. Valinomycin (Val) was added to the first row and Gramicidin (Gra) was added to the second row to simulate the polarized and depolarized state of the cells, respectively, while the third row served as the control (Figures 2-3a-d). The optical absorption peaks at different concentrations of DiSC3(5) were shown in the bar graphs (Figure 2-3e). Lower absorbance was observed in the Val group, which is consistent

with the theory that the voltage-indicators exhibit lower absorbance in the polarized state of cells. This confirmed the ability of DiSC3(5) to respond voltage changes at in-vitro level.

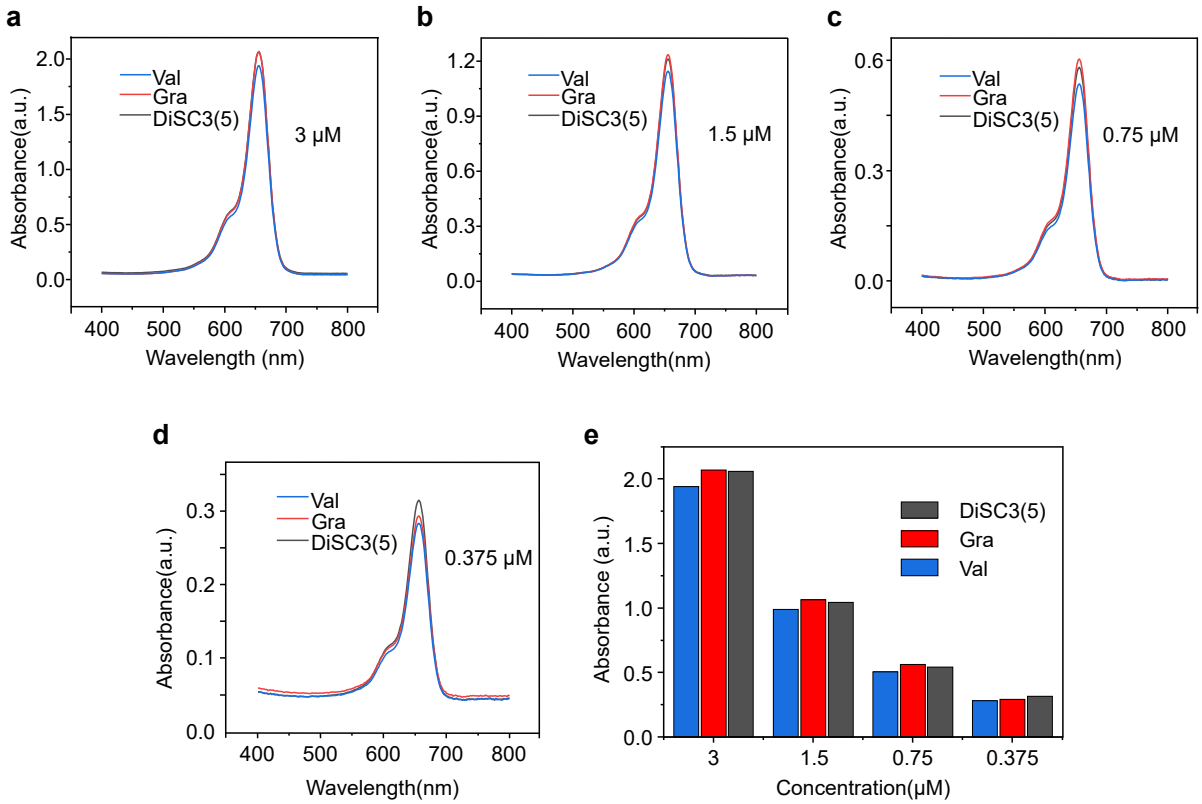

Figure 2-3. In vitro cell voltage response experiments under different concentrations of DiSC3(5). a-d) The absorption spectra under different concentrations: a) 3 μM, b) 1.5 μM, c) 0.75 μM, and d) 0.375 μM. e) The absorption peak of all groups. Valinomycin (Val) preferentially binds K+ ions and forms a lipid-soluble complex that allows K+ to enter the cell through the lipid bilayer. Val effectively increases the diffusion rate of K+ by 100,000-fold. In contrast, Gramicidin (Gra) binds and carries Na+ from one side of the membrane into the channel and diffuses to the other side of the membrane. These two substances are important carriers in membrane potential testing.

Then, the membrane potential was modulated by adjusting the K+ concentration of the extracellular medium (estimated by the Nernst equation), and meanwhile optical properties of DiSC3(5) were measured, which reflected with the changes of FL and PA signal. This allowed us to investigate connection and regularity between the FL and PA signal transformations of DiSC3(5) at different cell membrane potentials. A small animal fluorescence imaging system (IVIS Spectrum In vivo Imaging System, Perkin Elmer, USA)

was used to capture the FL images (Figure 2-4a). The signal increases with the advancing membrane potential, representing an enhancement in FL intensity with an expansion in depolarization, according to the statistical and quantitative analysis with regions of interest (ROI) of whole wells (Figure 2-4b, $n = 3$).

To check whether its PA effect also corresponds to the voltage change, PAM imaging was conducted to find DiSC3(5) variations in N2a's PA signal. Several PA images were captured under the G2 OR-PAM system (INNO LASER, China), with a scanning step size of 3 μm and an imaging area of 900×900 μm^2. The cells were clearly seen thanks to the high resolution (Figure 2-4c), and the black dash circle showed the contour of one single cell (top left). A self-written contour extraction algorithm was applied to the original image matrix, and the longest diameter of the contour was taken for computation and statistical analysis (Figure 2-5a). As can be seen, the majority of cells have a diameter of approximately 20 μm, which is consistent with the actual diameter of the N2a cell. The average full-width half-maximum (FWHM) of the PA measurements in Figure 2-5b and c (showing the A-line with the largest diameter among 10 randomly selected cells) further supported the accuracy of this observation. The PA signal steadily reduced as the resting potential was increased. The cell shape shrank and developed more hollow structures, which also suggested that the dispersion of DiSC3(5) resulted in a decreased PA signal. Subsequently, the mean single pixel intensity was calculated to reflect the average PA intensity at the different resting potentials using the images with similar cell densities ($n = 3$ in each group). As the potential changed, the results revealed a progressive drop in PA intensity (Figure 2-4d). We found that the PA response trended in the opposite direction of FL, which is in accordance with the rule of energy conservation. Coexistence of an increase of FL signal and a decrease of PA signal accompanies the appearance of nerve cell depolarization.

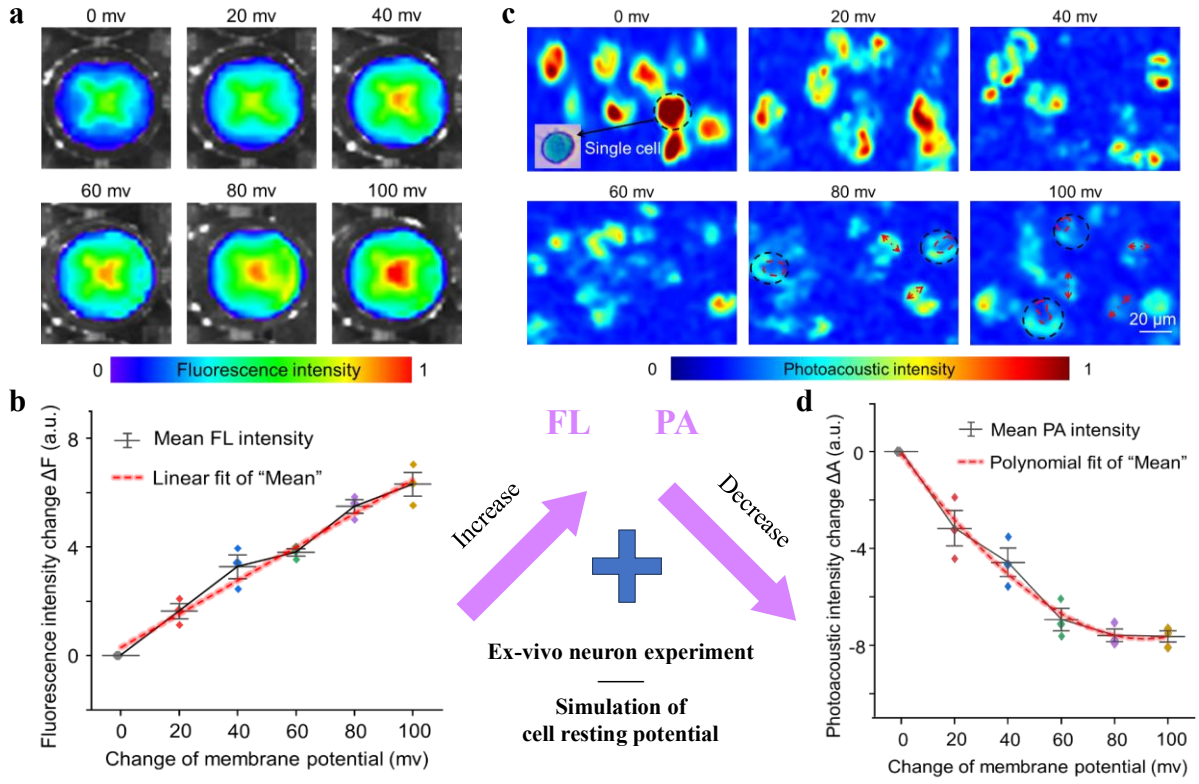

Figure 2-4. In vitro examination of the voltage response appearances of DiSC3(5). a) FL imaging of N2a with DiSC3(5) at different resting membrane potentials. b) Quantitative analysis of FL amplitude over the full FOV. c) PAM imaging of N2a with DiSC3(5) at different resting membrane potentials. d) Quantitative analysis of PA amplitude. All the error bar in the figures is SEM.

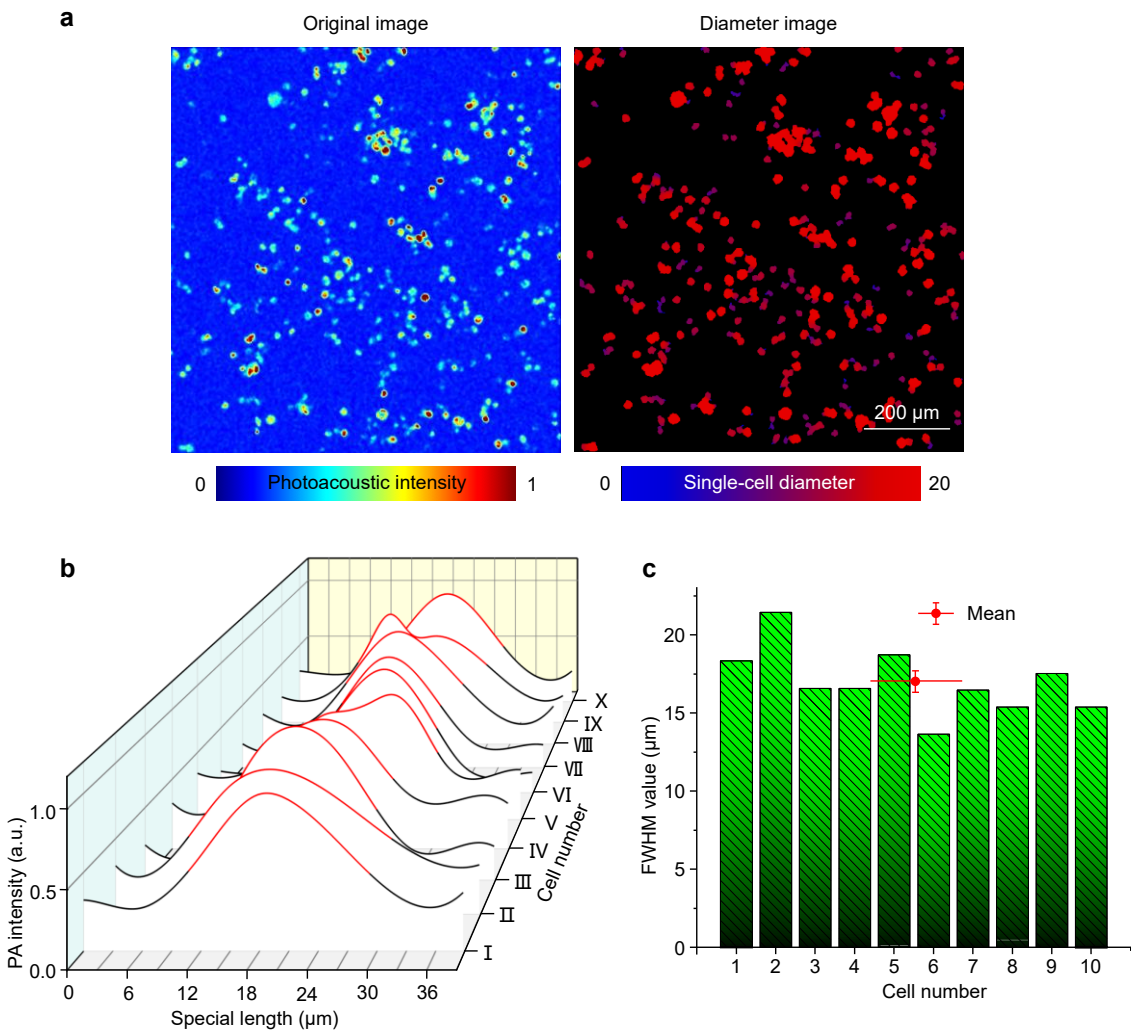

Figure 2-5. Statistics of cell diameters in PAM images. a) Cell diameter outlining and measurement. b) A-line signal of the longest diameter among 10 randomly selected cells. c) Statistics of FWHM in b. The average FWHM = 17.1 μm, which is very close to the cell diameter obtained by the algorithm in a. The error bar is SEM.

Following laser irradiation of the DiSC3(5) aqueous solution (concentration of 100 μM with 1% DMSO, Dimethyl sulfoxide), the optical absorption ratio was examined to evaluate the photobleaching effect (Figure 2-6a), and the absorption peak and ratio at 670 nm were individually recorded (Figure 2-6b, $n = 3$). It can be observed that DiSC3(5) retained around 75% of its optical absorption intensity after being continuously exposed to a pulsed laser for 30 minutes. Given this property, DiSC3(5) was exposed to relatively low laser energy due to light scattering and absorption by skin and tissue during in-vivo small animal tests, making it less susceptible to photobleaching. This means that DiSC3(5) has more stable optical

properties than most GEVIs, which is one of the most crucial qualifications for long-term in vivo monitoring.[110]

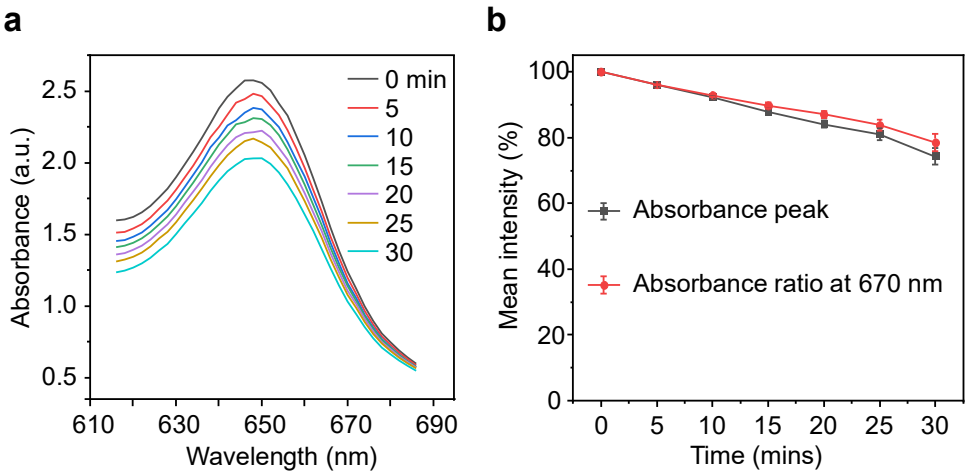

Figure 2-6. The photostability of DiSC3(5). a) Absorption spectra of DiSC3(5) solutions under different durations of laser irradiation. b) The statistics of the absorption peak and the absorption ratio at 670 nm.

2.4 Voltage-sensitive mechanism hypothesis

Most chromophores reach an excited state following absorbance of photons but release energy in the form of heat or emit other photons when the excited atoms return to their ground state. In this manner, the emitted photons may be detected as FL signals, or the converted heat generates ultrasonic waves that can be detected as PA signals, which align well with the principle of energy conservation. The cyanine dyes like DiSC3(5) are prone to agglomerate at high concentrations. There is weaker or none fluorescence in the aggregates, which is called fluorescent quench [159]. The principal of DiSC3(5) responding voltage via FL and PA changes is that cationic DiSC3(5) molecules can be actively attracted into the polarized cell at negative potentials and driven to aggregates by sufficiently high local concentrations, resulting in weaker-fluorescent aggregates, but the photoacoustic effect is instead enhanced. When a depolarization occupies, the aggregates are freed into monomers and emitted outside the cell with the ions flow, thus turning into fluorescent but weaker-photoacoustic monomers (Figure 2-7). This process is reversible and repeatable. This is because the onset of repolarization drives the dye monomers into the cell interior again and maintains the tendency for dye aggregation.

Other materials have also shown similar optical characteristics in earlier investigations [160]. Yet few have conducted meaningful studies on live animal's deep brain. Therefore, we propose an innovative attempt to use DiSC3(5) in the prolonged monitoring of electrodynamics in epileptic mice (longer than 30 mins).

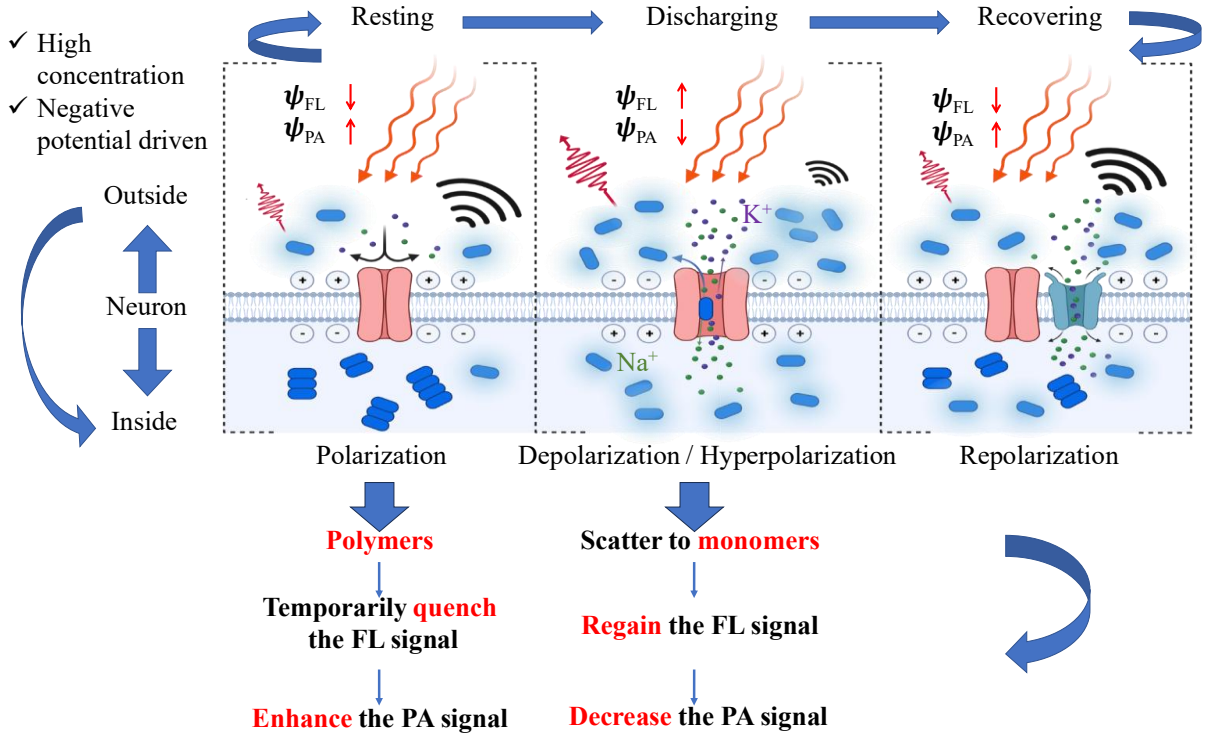

Figure 2-7. Mechanisms of VSD voltage response. DiSC3(5), a cationic VSD, penetrates the phospholipid bilayer of neuronal cell membrane and polymerizes under negative potentials, which results in temporarily quenching the FL signal while enhancing the PA signal. When the discharge reaction triggers a de- or hyperpolarization state, which drives the dye to scatter as monomers, they regain the FL signal and decrease the PA signal until repolarization.

2.5 Summary

In this chapter, we use fluorescence and photoacoustic-based cellular experiments to validate the optical response mechanism of the voltage-sensitive dye DiSC3(5). Cyanine cationic VSDs tend to aggregate at high concentrations, causing fluorescence quenching. Based on cellular experiments, we propose the following mechanism for the voltage-responsive optical behavior of DiSC3(5): In polarized cells, the negative membrane potential and osmotic pressure drive DiSC3(5) to form weakly fluorescent but strongly photoacoustic aggregates.

Upon depolarization, these aggregates dissociate into monomers with stronger fluorescence but weaker photoacoustic signals. This reversible process exhibits high photostability (>75%), making DiSC3(5) a promising long-term indicator for monitoring neuronal voltage dynamics such as in epilepsy.

Chapter 3 Structural and Functional Epilepsy Imaging *in vivo*: Fluorescence Monitoring

3.1 Animal epilepsy fluorescent imaging

Following validation through cellular experiments, we employed an in vivo small-animal epilepsy model to monitor the fluorescence and photoacoustic responses of the DiSC3(5), providing direct feedback on brain electrical activity. In this chapter, we present the experimental methods and results of in vivo fluorescence imaging.

Figure 3-1 illustrates the flowchart of animal experiments. Continuous injection of low-dose PTZ is a classical method for epilepsy modelling. In our modelling, we found that the survival rate was higher than 80%. The effectiveness of the models was demonstrated by acute and enormous EEG spikes as well as aberrant neuronal lesions in the cortex and hippocampus are. When epileptic mice carrying DiSC3(5) triggered seizures, both fluorescent and photoacoustic modes were used to detect voltage response. Their FL and PA signal changes can directly reflect the voltage dynamic fluctuations of the mouse brain. Therefore, a method can be established to localize the lesions, screen the epileptic signals, and quantify the regularity and features of the statistical signals.

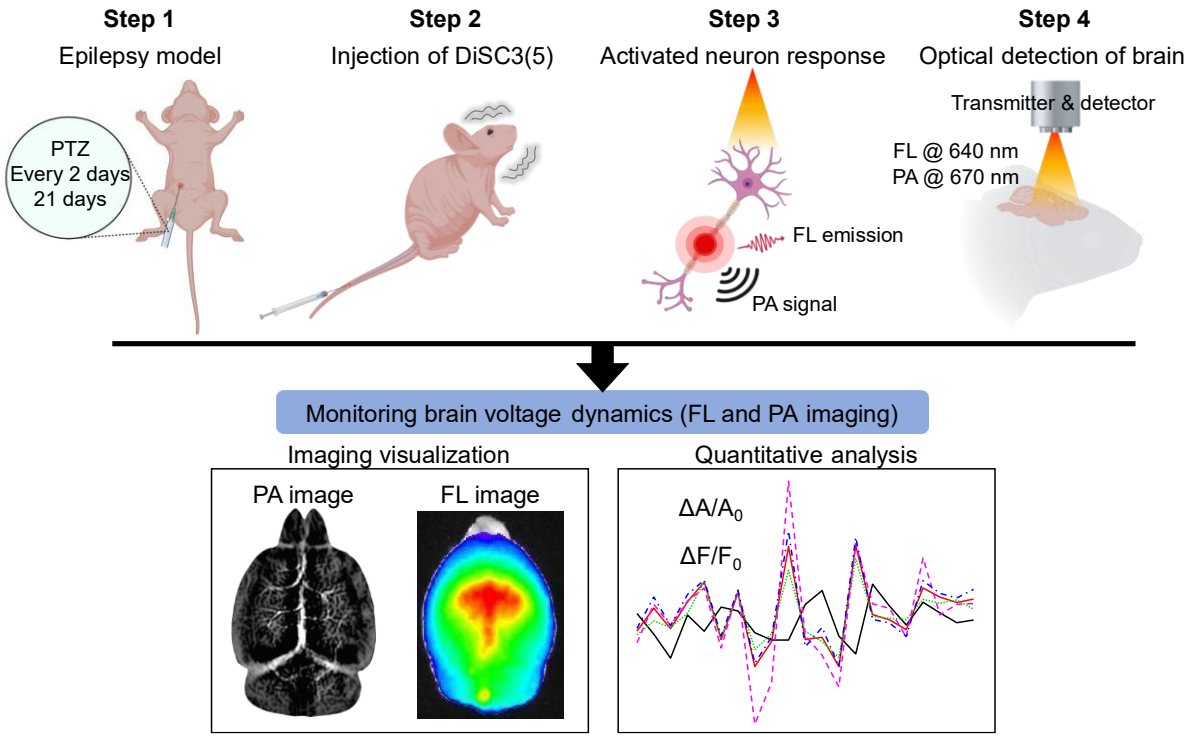

Figure 3-1. The workflow of in-vivo electrodynamics monitoring in an epilepsy mouse model. DiSC3(5), a cationic VSD, penetrates the phospholipid bilayer of the neuronal cell membrane and polymerizes under negative potentials, which results in temporarily quenching the FL signal while enhancing the PA signal. When the discharge reaction triggers a de- or hyperpolarization state, which drives the dye to scatter as monomers, they regain the FL signal and decrease the PA signal until repolarization. PTZ is an epilepsy-inducing drug. ψ_{FL} and ψ_{PA} represent the intensity values of the FL and PA signals, $\Delta F/F_0$ and $\Delta A/A_0$ are the change rate of ψ_{FL} and ψ_{PA}, respectively.

3.2 Epilepsy models and fluorescence imaging protocols

3.2.1 Animals and ethical statement

Mice aged 9 to 12 weeks weighing 25 to 35 grams were used in the studies. The BALB/C-NUDE mice were purchased from Guangdong Medical Laboratory Animal Centre (China), and wild-type ICR mice were obtained from SPF (Beijing) biotechnology co., LTD. All mice were used to the typical laboratory conditions of humidity (55%), temperature (22.1 °C), 12-hour light/dark cycle, and full access to food and water. All animal experimental protocols

were approved by the ethics committee of Guangdong Provincial People's Hospital (No. KY-N-2022-122).

3.2.2 Epileptic mouse model

Pentylenetetrazol (PTZ) is a GABA-A receptor antagonist. A single low-dose intraperitoneal injection of PTZ may elicit a mild seizure without convulsions, whereas a high dose in an animal may trigger a sudden, severe seizure and cause death. On the other hand, PTZ injections given repeatedly at low doses lower the threshold for convulsive seizures, so long-time low-dose PTZ therapy causes a severe tonic-clonic epilepsy. Therefore, successive injections of a sub-convulsive dose have been used to develop a chemical kindling epilepsy mouse model [161, 162]. PTZ-induced kindling in mice is an easy-to-use and well-accepted model for chronic epilepsy. Therefore, we selected this model for use in later studies.

The steps of the PTZ-induced epilepsy mouse model are as follows:

(1) PTZ is dissolved in sterile 0.9 percent (w/v) NaCl at a concentration of 2.5 mg/mL. PTZ should be prepared on the day of usage.

(2) Tag the mice and record their body weight for use.

(3) Calculate the volume of PTZ solution for the injection based on the body weight of the mouse and the previously determined injection dose. The PTZ injection dosage is determined by the genotype and strain of the mouse. For the wild-type ICR mice, a PTZ injection dose of 35 mg/kg is used, while a more modest PTZ dose (1.8 mg/kg) is suggested for BALB/C-NUDE mice. So, when the ICR mouse weighs 30 g, 1.05 mg of PTZ is required, means that 420 μL of a 2.5 mg/mL PTZ solution should be injected (35 mg/kg × 0.03 kg / 2.5 mg/mL = 0.42 mL), but a nude mouse of the same weight only needed to be injected with 216 μL (18 mg/kg × 0.03 kg / 2.5 mg/mL = 0.216 mL).

(4) Use a 1-mL syringe and a 27-gauge needle to intraperitoneally inject PTZ into the animal's left or right abdominal region. Midline injections should be avoided. Avoid giving oneself the same shot many times.

(5) After administering PTZ, place the animal in an observation chamber for habituation, and observe the behavior for 30 minutes. Then classify and score any anomalous behavior, following the international certification of animal epilepsy grade criteria.

(6) Inject PTZ every two days. 8-12 injections are usually enough, on average, to produce a success model. Additionally, the injections can be discontinued early if the mice reach

seizure level 5 or higher with three consecutive injections. This shows that the mice have been effectively modelled and are ready to be employed in the upcoming tests.

(7) All injection procedures should be done between 14:00 and 18:00.

The modelling process was shown in the Figure 3-2.

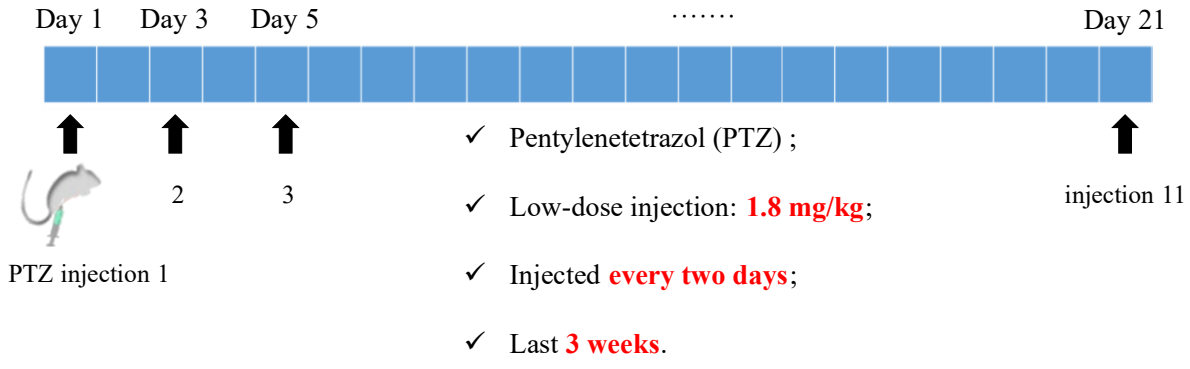

Figure 3-2. PTZ-induced epilepsy model.

3.2.3 In-vivo fluorescence imaging protocols

After an epileptic mouse was anaesthetized in the chamber (isoflurane, 1% VOL, gas flow rate of 1 cm^3/s), the mouse was placed on a holding platform and its head was secured with ear rods and then switched to a mask for prolonged respiratory anesthesia. An intravenous indwelling needle was inserted into the tail of the mouse in advance and then placed in the fluorescence apparatus (IVIS Spectrum In vivo Imaging System, Perkin Elmer, USA) to capture the head image "Before" (-130th min). Then, the mice were placed in the instrument after injecting 100 μL of a 100 μM DiSC3(5) solution through the tail vein at a rate of 20 μL/min using a microinjection pump. FL images continued to be acquired at the time points of 5 min (-125th min), 15 min (-115th min), 30 min (-100th min), 45 min (-85th min), 60 min (-70th min), 90 min (-40th min), and 120 min (-10th min) after the cycling of DiSC3(5). Then, a certain amount of 7.2 mg/ml of PTZ solution was injected intraperitoneally into the mice and continuous monitoring was performed every minute for 30 minutes. Finally, the head ROI information was extracted from the obtained time series images for quantitative analysis. In the in-vivo experiments, we chose a PTZ injection volume that was 4 times higher than the modelling to induce seizures, since PTZ-induced epilepsy was suppressed by anesthesia, which was also validated by in vivo EEG (Figure 3-3). The first row displays EEG signal monitoring in normally behaving mice without epilepsy. The signal is determined to be steady and free of any unusual electrical signals. The second row displays the EEG

signal monitoring of mice that are allowed to behave naturally while receiving a low dosage of PTZ (2.5 mg/kg). Several aberrant electrical signals are seen, mostly in the first 15 minutes. The third row shows the EEG monitoring of an anesthetized, low-dosage PTZ-induced epileptic mouse, and once more, no aberrant signals are seen. In the fourth row, epileptic mouse is monitored for EEG activity while under anesthesia and receiving a high-dose injection of PTZ (10 mg/kg). More seizures are displayed, occurring randomly within 30 minutes.

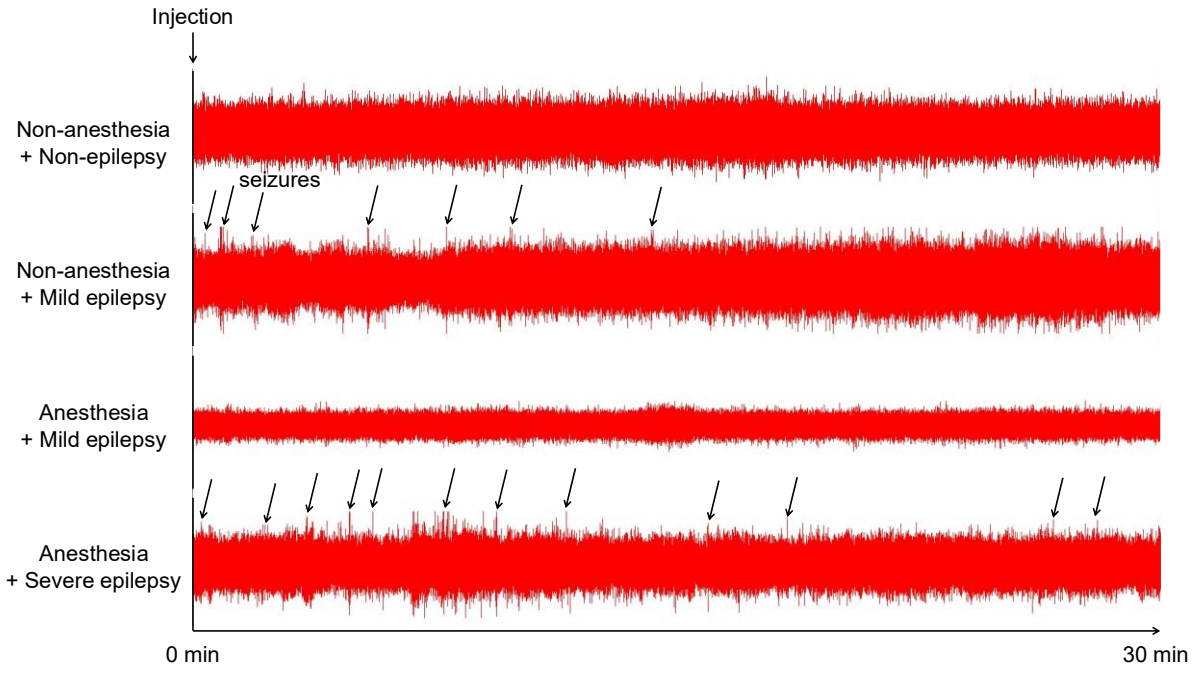

Figure 3-3. Long-time sequences of the mouse's EEG signal under various conditions.

3.2.4 Data processing and analysis

FL images and data were generated with IVIS software. The data were presented as mean ± SEM (standard error of mean). In vivo results of FL statistical analyses were performed with the Mauchly's sphericity test, and the comparisons between distinct groups were done based on a two-way repeated measures analysis of variance (ANOVA) procedure in RStudio/2023.09.0+463. $\Delta F/F_0$ was calculated with the formula: $\Delta F/F_0 = (F_i - F_0)/F_0$, where F_i is the FL intensity at i_{th} time point, and F_0 is its corresponding linear fit value.

3.3 Results: Monitoring of neuronal activity and seizure progression

After 21-days epileptic modelling, an invasive EEG monitoring in the mouse brain was conducted to validate the successful establishment of the model. As shown in Figure 3-4, prior to the PTZ injection, the EEG signal is steady. About 2-3 minutes after the PTZ injection, an aberrant electrical signal arises, and shortly after that, a large continuous electrical signal suggests a grand mal seizure (upper panel). The related high-frequency components are displayed on the thermal frequency graph below. This graph provides compelling proof that the epilepsy model works. Subsequently, the epileptic mice were euthanized, and their intact brain tissues were excised. The cortical and hippocampal CA3 regions underwent histological examination through hematoxylin-eosin (HE) and Nissl staining, followed by microscopic imaging (Figure 3-5). Results indicated that the neurons in the cerebral cortex and hippocampus of PTZ-induced epileptic mice exhibited irregular arrangements, with intensely stained neuronal nuclei and cytoplasm, reflecting pathological alterations. Similarly, abnormal Nissl bodies indicated neuronal damage, whereas neurons in the control group appeared healthy.

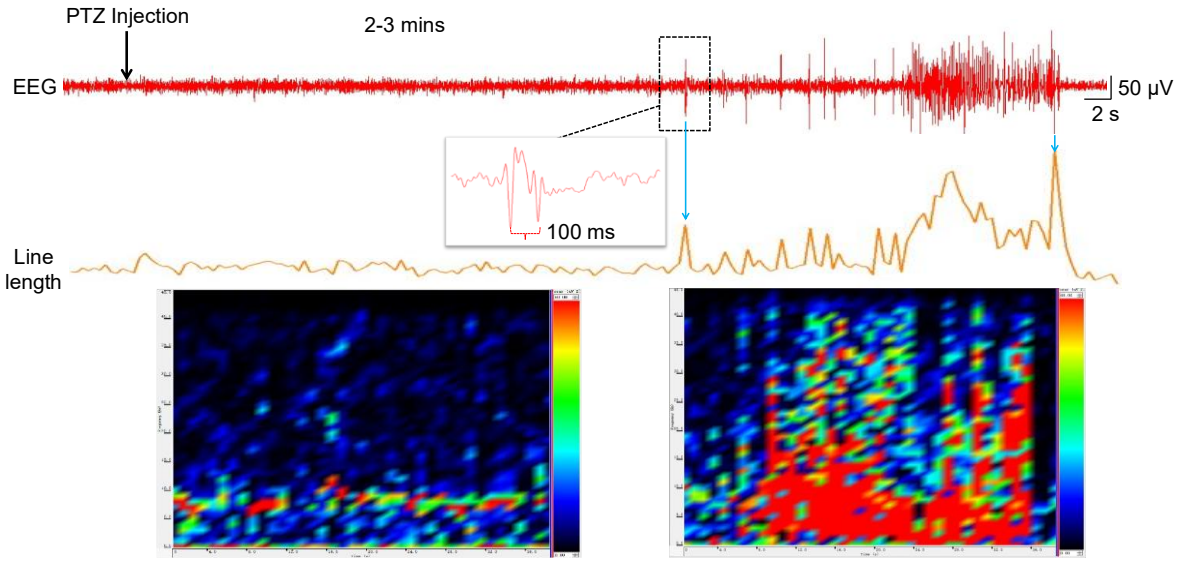

Figure 3-4. EEG monitoring of epilepsy mouse brain.

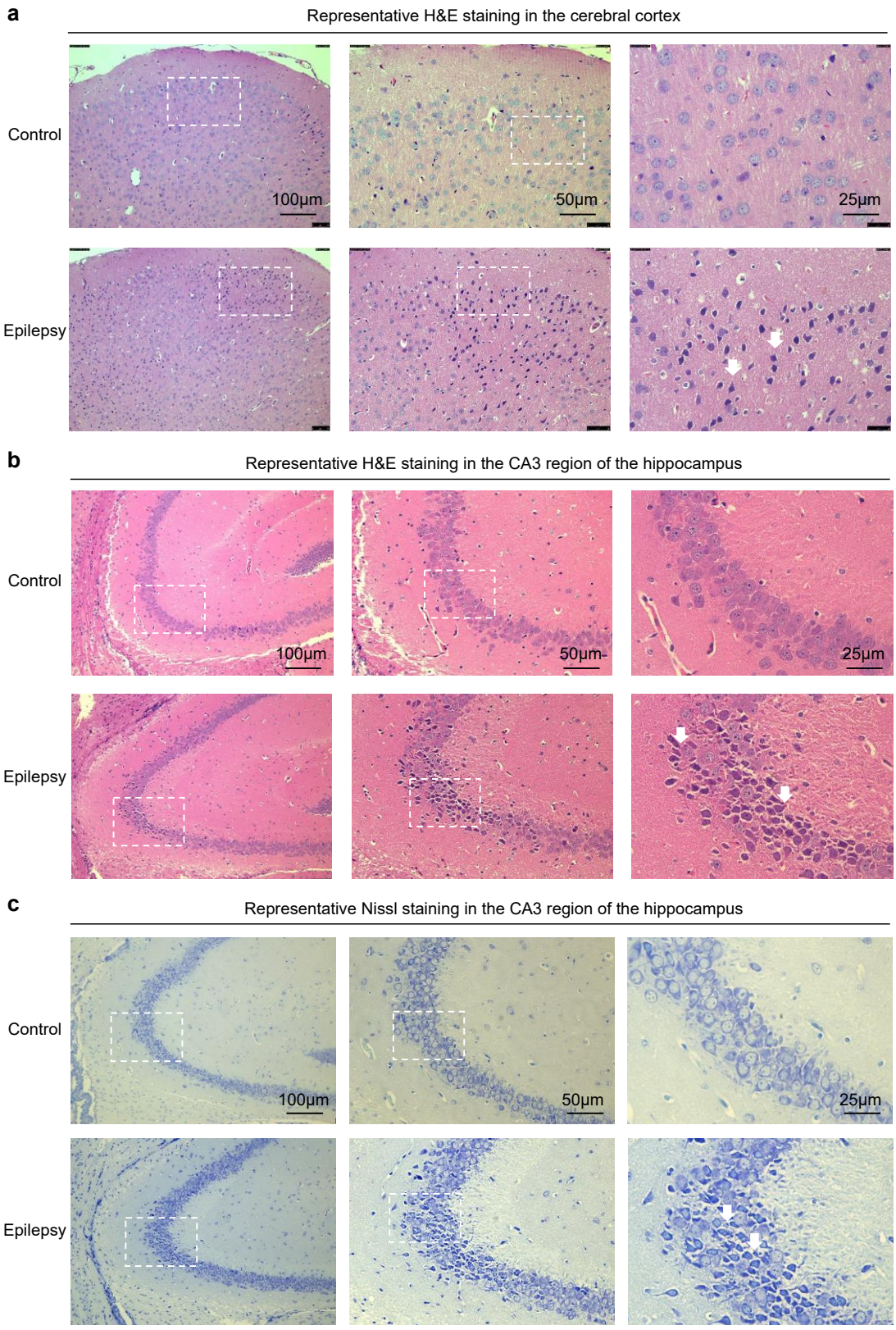

Figure 3-5. Pathological section staining of the isolated epileptic mouse brain. a) H&E staining of the cerebral cortex. b) H&E staining in the CA3 region of the hippocampus. c) Nissl staining in the CA3 region of the hippocampus.

Then, we performed FL imaging in vivo to detect the ability of DiSC3(5) that respond to the voltage dynamics in the cortex. With at least three animals in each group, three groups were set up for in vivo FL imaging: an epileptic voltage response group (DiSC3(5) + PTZ), a non-epileptic voltage response group (DiSC3(5) + NS, NS is the normal saline), and an epileptic non-voltage response group (ICG + PTZ). After injection of DiSC3(5) solution through the tail vein, the animals were observed at rest for two hours, with an excitation at 640 nm and an emission at 680 nm. It can be seen that the FL signal peaked at 5 minutes (Figure 3-6a, 125th min before injection) and then declined gradually until reaching a relatively stable condition (-40~0 min), which was caused by a number of factors. Firstly, DiSC3(5) entered the nerve cells, generated aggregation under the action of negative potential, and temporarily quenched the FL. Secondly, extra probes were disseminated throughout the brain with the blood flow and metabolized away. Thirdly, a tiny number of probes were photobleached upon slight light stimulation. All mice were subjected to FL images captured with anesthetized and immobilized heads. We utilized a PTZ injection to induce seizures, with a dosage four times greater than that used in the epilepsy modelling, since anesthesia might significantly reduce neuronal activity and the probability of seizures [163].

An intraperitoneal injection of PTZ or saline was administered, followed by continuous recording at a rate of one frame per minute (Figure 3-6a, 30 minutes after injection). We discovered that the DiSC3(5) + PTZ group exhibited clear feedback of FL signal fluctuations through quantitative statistical ROI analysis. Within approximately two minutes, the signal began to elevate, reaching its peak at 15 minutes, followed by a gradual decline and stabilization after 20 minutes (Figure 3-6b). Seizure peak periods were identified as those exceeding the linear growth trend. However, due to the limited temporal resolution of in-vivo FL imaging, only vague time intervals could be observed. The time-varying curves for the three groups are shown in Figures 3-6c and d. The two curves without brain voltage response (DiSC3(5) + NS and ICG + PTZ) exhibited significant differences in their trends when compared to the epilepsy group (DiSC3(5) + PTZ, $P << 0.05$, ***), further confirming that the rapidly increasing FL signal corresponds to voltage changes in the brain associated with seizures.

The epilepsy group displayed a significant signal augmentation within 30 minutes following the seizure episode. The CR of FL ($\Delta F/F_0$) was calculated, revealing that epilepsy group had a CR of over 9%, approximately four times higher than the other two groups (Figure 3-6e). Although, the ratio is not as high as other fluorescent imaging rates [164], it still provides

sufficient sensitivity and contrast for voltage dynamics screening. Furthermore, if specific regions are targeted, FL should allow for the detection of CRs reaching a few tens of percent, rather than using the entire brain ROI.

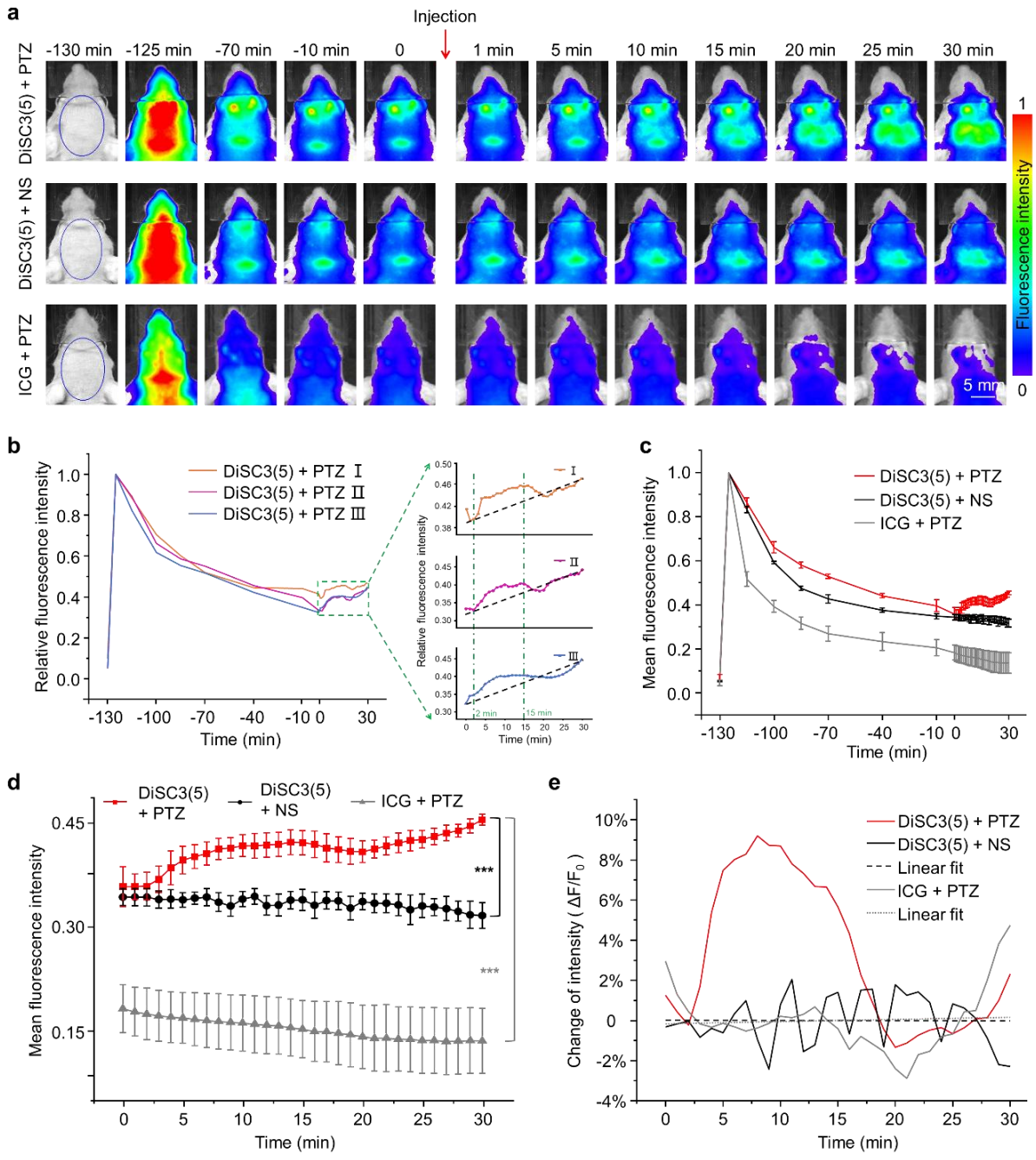

Figure 3-6. FL imaging of epileptic mouse brain based on DiSC3(5). All signals are normalized to a uniform level. a) FL Images of mouse brain voltage response. b) FL signal change curves of the experimental group (DiSC3(5) + PTZ). c) Quantitative statistical analysis of the ROIs shown in a. d) Quantitative statistical analysis of the mouse brain after injection. Experimental group has a significant difference with two control groups (p <<

0.05: ***). e) Temporal profiles of the proportionate increase in FL intensity in the mouse brain after injection. All the error bars are SEM.

Statistical analysis has been performed on three independent samples of fluorescence signals in table 3. The results indicated that all time points satisfied the normality test. Subsequently, Mauchly's sphericity test was conducted for the fluorescence groups. The results for the fluorescence group showed $p = 0.1126 > 0.05$, indicating that the sphericity assumption was met. Therefore, a repeated measures analysis of variance (ANOVA) was carried out, revealing a significant difference between the experimental and control groups ($p << 0.05$). Detailed data are presented in the table below.

Table 4. The results of analytical examination of in vivo fluorescence monitoring.

1. All time points satisfy the normality test					
2. Mauchly's test of sphericity			p > 0.05, satisfying the spherical hypothesis		
	W	p-value			
FL	0.012689	0.1126			
3. Two-way repeated measures analysis of variance (ANOVA)					
	Group	Lwr	Upr	p-value	
FL	2-1	-8.89%	-6.42%	9.43E-28	***
	3-1	-26.94%	-24.47%	1.71E-119	***

*Notes: p-value: 0 '***' 0.001 '**' 0.01 '*' 0.05 '.' 0.1 ' ' 1.W is the weight of sphericity. Lwr is the lower endpoint of the confidence interval. Upr is the upper endpoint of the confidence interval.*

3.4 Discussion of findings and summary

In the in-vivo fluorescence experiments, we observed a significant enhancement in whole-brain signals in mice during epileptic seizures, whereas no such changes were observed in the control group. These in vivo findings are consistent with our cellular-level experimental

results. Especially, the ICG + PTZ group exhibited no significant signal alterations. Although both ICG and DiSC3(5) are cyanine-based indicators, ICG lacks the electrical signal-sensitive response mechanism. Therefore, these observations further confirm that the signal changes associated with DiSC3(5) result specifically from epileptic activity.

It should be noted that while small animal FL imaging technology offers a wide FOV, its application is limited by its relatively low resolution and lengthy acquisition time. Consequently, we were only able to evaluate the duration of epileptic convulsions on a minute scale and were unable to precisely pinpoint the specific brain regions where seizures occur. Therefore, there is a need for improved localization techniques with higher spatial and temporal precision to better detect neuronal electrical activities.

Chapter 4 Structural and Functional Epilepsy Imaging *in vivo*: Photoacoustic Mapping

4.1 Introduction

Photoacoustic imaging has significantly better spatial resolution and imaging speed than in vivo fluorescence imaging, so it is more suitable for rapid tracking of structural and functional activities in the whole brain. In this chapter, we employ a whole-field photoacoustic brain detection (WF-PABD) platform adapted with the photostable DiSC3(5) (PA-VSD), to directly monitor voltage dynamics over 30 minutes (even longer if needed) in an intact epileptic mouse brain. A methodology is developed to utilize PA data analysis to provide identification and screening of epileptic signals. Regarding system validation, WF-PABD possesses a vast FOV of ~5 cm in diameter for enough covering the whole mouse brain, a high spatial resolution of ~110 μm, a fast imaging-rate of 10 Hz, and a deep penetrating depth covering all areas of interest. Following in-vivo PA-VSD investigations, we found that the fluctuations of PA signals aligned with the optical features of voltage response. PA-VSD localized epilepsy foci and screened seizures dynamics non-invasively, as well as offered guidance on electrical conduction pathways and functional communications across brain regions. Through multiple data processing, it can be discovered that epileptic signals contain more high-frequency components than calm signals have. Moreover, there exhibits a close correlation between the change rates (CRs) and high-frequency amplitudes of PA signals, showing a peak-to-peak pairing feature. It is anticipated that a new methodology can be established by capturing the CRs and discrete high-frequency amplitudes (DHF) coupling to screen epileptic sequences. The results highlight the potential of PA-VSD as a high-spatiotemporal-resolution tool for in-depth analysis of brain voltage dynamics. It is expected that the platform might serve as a springboard for further research in photoacoustic neuroscience and neuropathophysiology.

4.2 Experimental setup and imaging protocols

4.2.1 PA imaging implementations

A simplified schematic of the WF-PABD system is illustrated in Figure 4-1. In this system, we employed a wideband laser (Q-smart 450, Quantel laser, France) with output wavelengths ranging from 670 to 980 nm, 1064 nm, and 1190 to 2600 nm, operating at a laser repetition rate of 10 Hz. The pulsed light was expanded through a concave lens (LD1357, Thorlabs, USA) and uniformly irradiated onto the mouse head. High-speed PA signal detection was achieved using a fully circular ultrasonic transducer array consisting of 512 elements (Imasonic, France). The diameter of the ultrasonic ring array was ~10 cm, with a central frequency of 5.5 MHz and a bandwidth of 9.9 MHz (more than 90%). A transparent glass was placed above the ultrasonic ring array chamber, while a layer of cling film was applied beneath it. The chamber was filled with water using a pump, and a negative pressure method was employed to create a concave groove in the cling film. Anesthetized mouse was fixed in the concave groove using a holder, and the head was tightly coupled to the water chamber using ultrasound-coupling gel. This water medium facilitated acoustic coupling and ensured the propagation of PA signals. Subsequently, a 512-channel data acquisition system (DAQs, Photosound, USA) with a sampling rate of 40 MSa/s was utilized to simultaneously receive the PA signals in parallel, which warrantied an ultrafast imaging acquisition time (~10 μs/frame) to avoid respiratory and motion artifacts.

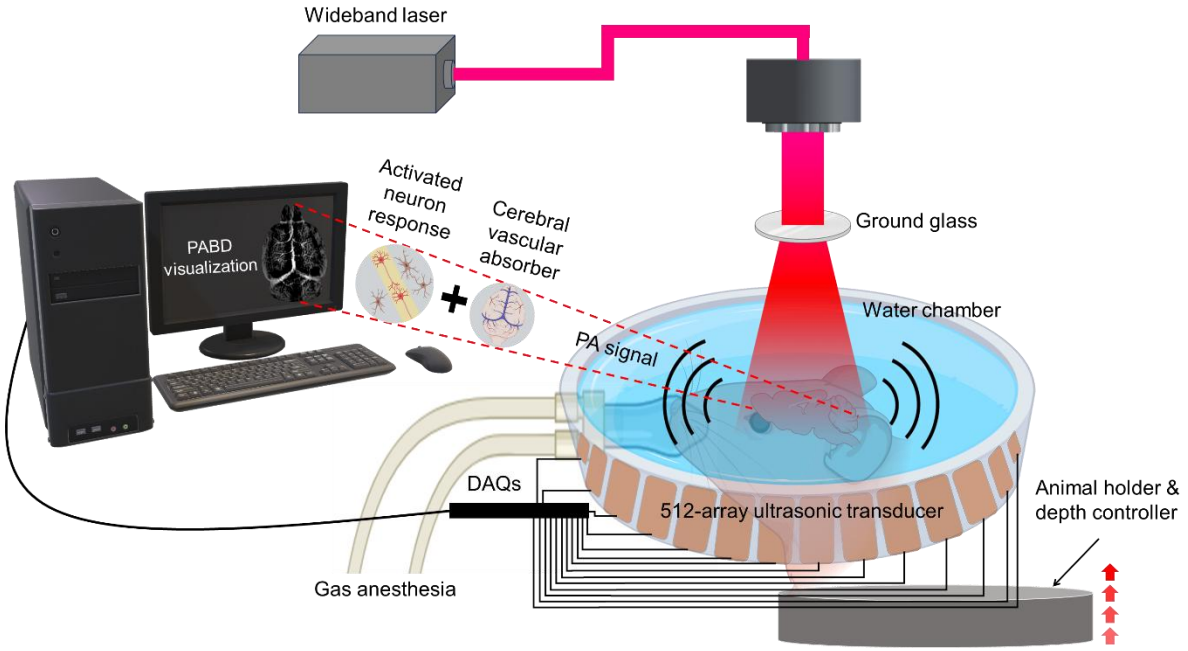

Figure 4-1. WF-PABD implementations. PA signals come from a stronger neuron response via VSDs and a weaker blood absorption.

The PA platform used a laser with an excitation wavelength of 670 nm, and a single pulse energy of about 100 mJ. An average laser fluence of 56 mJ/cm^2 is calculated when the spot size over the entire mouse brain is considered, and this falls inside the photodamage threshold [165, 166]. The detections occurred with a 40 dB gain in the following investigations. In a phantom experiment, the system was characterized to have a vast imaging range of ~5 cm in diameter and a lateral resolution of less than 110 μm at the center, and ~250 μm at the distal end. The axial resolution was also best at the center and gradually decreased away from the center (Figure 4-2). The superior resolution at the center is primarily due to the circular ultrasound array's ability to receive ultrasonic signals from all directions for targets located centrally, thus achieving the highest spatial sampling rate and the most complete imaging aperture. When the targets are away from the center, these advantages diminish, resulting in a reduction of resolution.

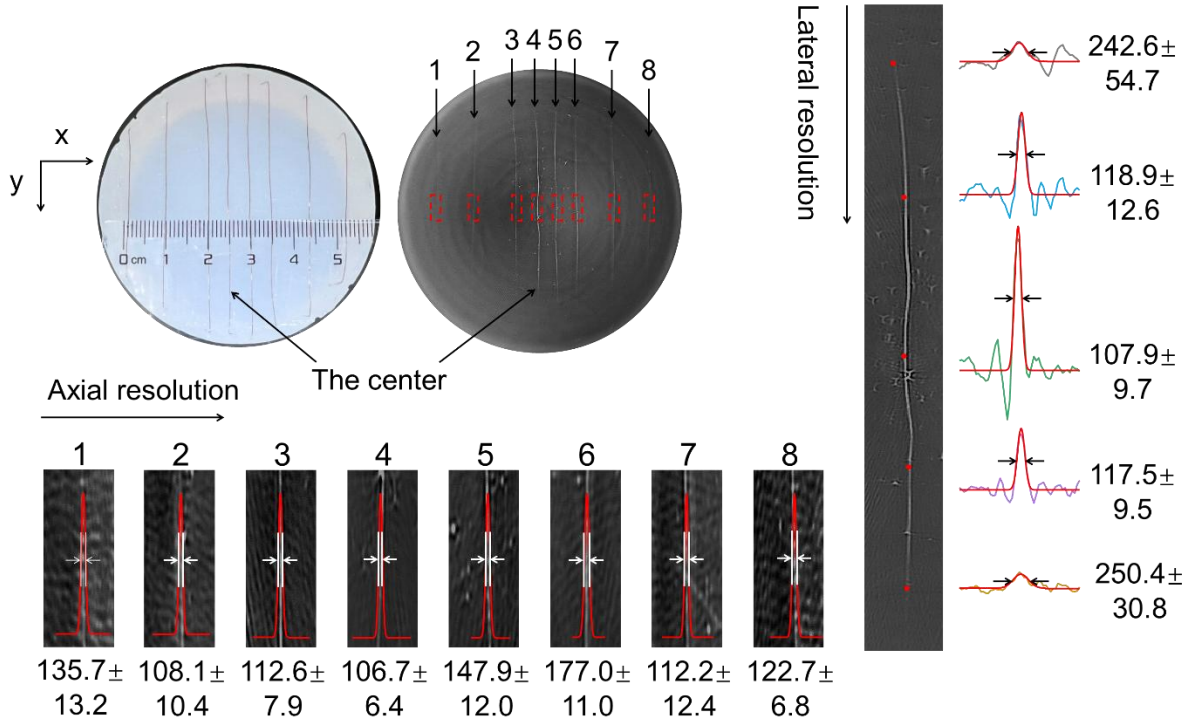

Figure 4-2. Evaluation of the axial and lateral resolutions. The units are microns.

During in-vivo detection, DiSC3(5) was intravenously administered to mice via tail vein injection to introduce the dye into the systemic circulation. As a cationic and lipophilic molecule, DiSC3(5) readily incorporates into the neuronal cell membrane. In our epileptic mouse model, the blood-brain barrier (BBB) is typically compromised due to the pathological state, thereby facilitating the extravasation and brain parenchyma penetration of exogenous molecules. Consequently, the dye successfully accumulated within neurons in the brain. This outcome was further verified by PA structural imaging of the brain vessels in vivo and fluorescence imaging of brain tissues ex vivo. In structural imaging, a mouse was placed on a holding platform, and its head was secured with ear rods and anaesthetized with a mask for prolonged respiratory anesthesia (isoflurane, 1% VOL, gas flow rate of 1 cm^3/s). An elevator was placed below to control movement and scanning of mouse brain in the elevational direction. We set the top horizontal section of the mouse cerebral cortex as the 0-depth plane, and non-invasively captured the brain images of the live mouse. The vascular and brain structures at different depths (0-4 mm) were displayed in Figure 4-3a. After the experiment, the mouse scalp was opened, and the cortex was imaged with a camera. It was found that the reconstructed PA brain vascular structures perfectly matched the actual vascular structure, even for the tiny blood vessels at the edges (indicated by the red arrows in Figure 4-3a).

Following mouse cardiac perfusion procedure, the brain (without blood) was preserved and fixed in paraformaldehyde. The visible fluorescence signal indicated that DiSC3(5) was present in the brain parenchyma, confirming the presence of the dye in neural cells in the absence of blood contamination. Then, the brain images in horizontal, sagittal, and coronal sections were obtained. It can be observed that several functional regions, such as the cortex, hippocampus, et al, can be identified from the PA images (Figure 4-3b). It shows that despite the absence of blood uptake, VSDs were still able to provide signals of sufficient contrast for brain image capturing. All those results suggested the advantages of PA-VSD, such as vast FOV, high spatiotemporal resolution, sufficient contrast, and functional information readout capabilities.

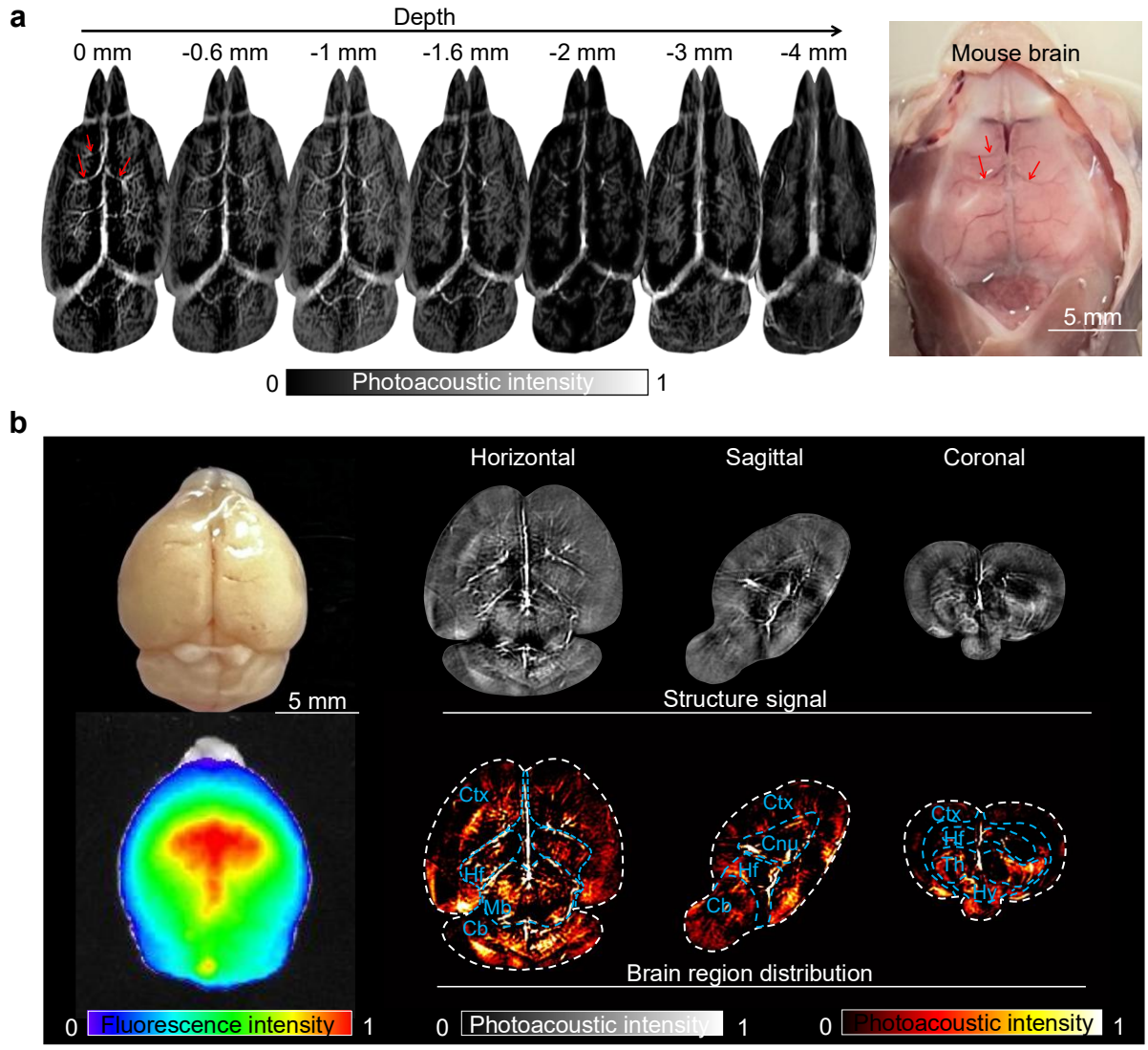

Figure 4-3. High-resolution photoacoustic visualization of the mouse brain. a) Intravital visualization of whole mouse brain at different depths (side-view with X: 310° Y: 10°). b) Images of isolated brain tissue carrying DiSC3(5) provide structural details in the horizontal, sagittal, and coronal sections and contour lines for several brain regions. Reference from Mouse Brain Atlas (75, 152, 264). Ctx: Cerebral Cortex; Cp: Caudata Putamen; Hi: Hippocampal; Th: Thalamus; Sc: Superior Colliculi; Ic: Inferior Colliculi; Bfs: Basal Forebrain Septum; Hy: Hypothalamus; Rm: Rest of Midbrain; Cb: Cerebellum; Bs: Brain Stem.

4.2.2. Imaging protocols

Based on observations from in vivo fluorescence imaging, a period of approximately 2 hours was required for the DiSC3(5) to reach a stable state within the brain. Consequently, we employed the same acquisition strategy in the PA experiments involving mice. After an epileptic mouse was anaesthetized in the chamber (isoflurane, 1% VOL, gas flow rate of 1 cm^3/s), the mouse was placed on the PA system holder and its head was secured with a toothpick and ear rods and then switched to a mask for prolonged respiratory anesthesia. An intravenous indwelling needle was inserted into the tail of the mouse in advance and then placed in the WF-PABD system to capture the head image "Before" (-130th min). Then, the mice were placed in the instrument after injecting 100 μL of a 100 μM DiSC3(5) solution through the tail vein at a rate of 20 μL/min using a microinjection pump. PA images continued to be acquired at the time points of 1 min (-129th min), 5 min (-125th min), 15 min (-115th min), 30 min (-100th min), 45 min (-85th min), 60 min (-70th min), 90 min (-40th min), and 120 min (-10th min) after the cycling of DiSC3(5). Then, a certain amount of 7.2 mg/ml of PTZ solution was injected intraperitoneally into the mice and continuous monitoring was performed for 30 minutes with an imaging speed of 10 frames/second. Finally, the head ROI information was extracted from the obtained time series images for quantitative analysis.

4.2.3 Data processing and analysis

PA images were processed and analyzed using MATLAB 2021b. The data were presented as mean ± SEM (standard error of mean). In vivo results of PA statistical analyses were performed with the Mauchly's sphericity test, and the comparisons between distinct groups were done based on a two-way repeated measures ANOVA procedure in RStudio/2023.09.0+463. $\Delta A/A_0$ was calculated with the formula: $\Delta A/A_0 = (A_i - A_0)/A_0$, where A_i is the PA intensity at i_{th} time point, and A_0 is its corresponding linear fit value. The correlation hotmaps were generated with Pearson type by the OmicShare tools, a free online platform for data analysis (http://www.omicshare.com/tools). Some icons in the schematic were from BioRender. All curves were produced using Origin 2022.

4.3 Results: Photoacoustic detection of neuronal activity and epileptic events

4.3.1 Epileptic photoacoustic signal analysis

PA imaging has proven to have great potential in achieving higher spatial and temporal resolutions for brain monitoring. We set up two groups for the PA experiments: a control group that received a saline injection, and an epilepsy group that received a PTZ injection. To allow sufficient time for DiSC3(5) to enter the brain through systemic circulation and achieve stabilized distribution, we initially observed the signals for two hours before inducing acute seizures in mice. The PA signal was low at the beginning (i.e., -129th min in Figure 4-4a) because of discrete dyes and blood dilution. Thereafter, it gradually increased and reached a relatively steady state (-40~0 min, consistent with the FL results). Both FL and PA data indicate that VSDs require at least an hour and a half to establish a stable or resting condition, suggesting that they cannot be used to immediately detect voltage changes upon entering the organism. The slower rate of stabilization in the epileptic group compared to the control group is likely attributed to the pathological manifestations of the epilepsy model, which increase neuronal activity and hinder the dyes from reaching a steady state. The PTZ-induced seizures displayed more extreme signal changes than the control group, showing a somewhat significant difference ($0.001 < p = 0.0019 < 0.01$, **). However, the overall trend was also decreasing, which was consistent with the in-vitro test results (Figure 2-4). These findings demonstrate that PA-VSD could detect seizures as early as 2 minutes in advance (Figure 4-4b, Zone 1), making it as sensitive as EEG monitoring. During the monitoring of epileptic activities, numerous large seizures occurred within a 30-minute period.

Statistical analysis has been carried out on two independent samples of photoacoustic signals. The results indicated that all time points satisfied the normality test. Subsequently, Mauchly's sphericity test was conducted, which yielded $p = 1 > 0.05$, confirming the assumption of sphericity. The repeated measures ANOVA also demonstrated a significant difference between the two groups ($0.001 < p < 0.01$). Detailed data are presented in Table 4.

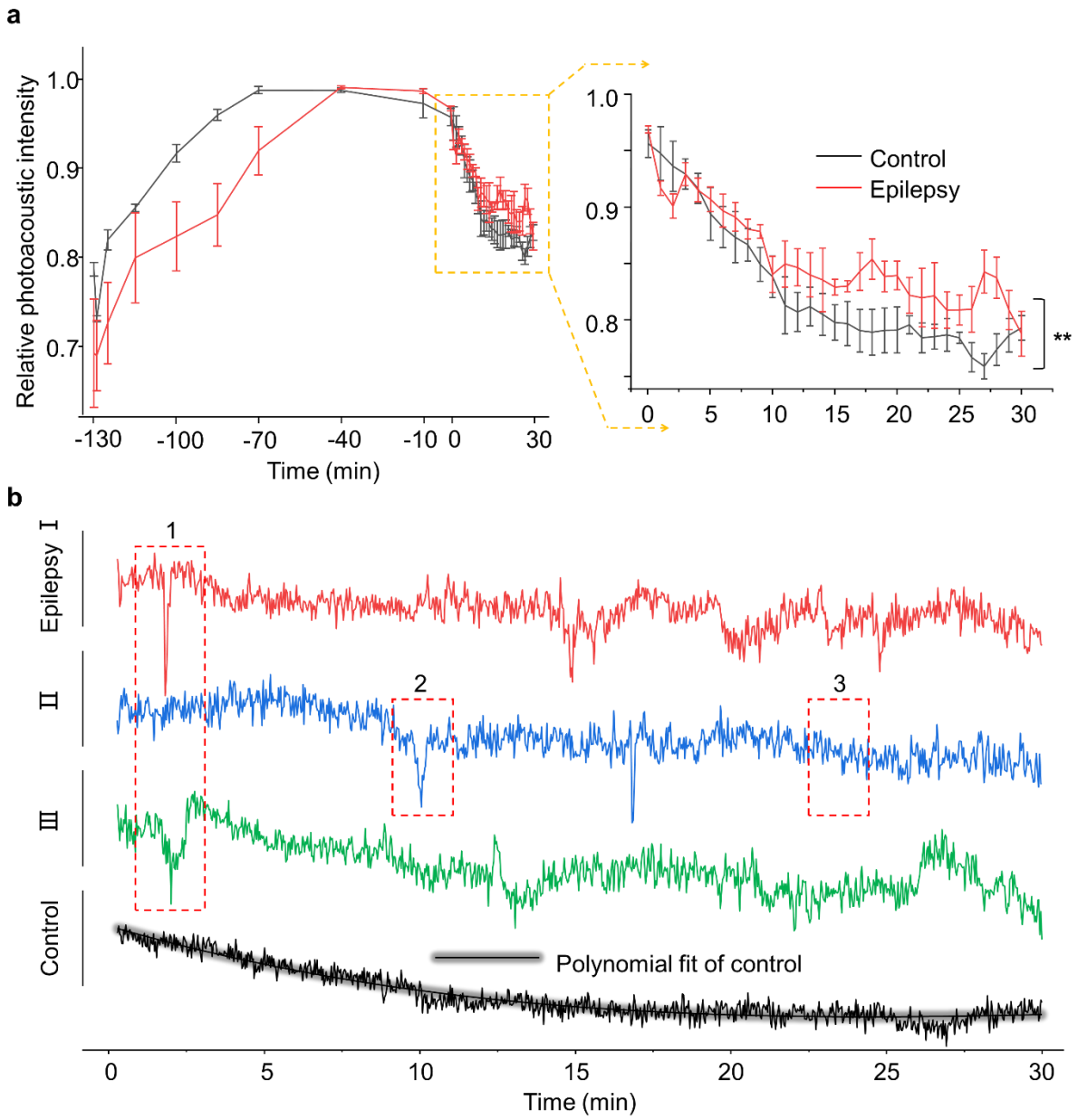

Figure 4-4. In-vivo PA-VSD monitoring of electrical activity in epileptic mouse brain. a) Comparison of whole brain PA signals in epilepsy and control groups. The yellow dashed box shows the signal changes after injection and the two groups have a significant difference ($0.001 < P = 0.0019 < 0.01$). The error bars are SEM. b) Temporal profiles of three epilepsy groups and the control group after injection. The control group is the mean data of three mice, and the black-shaded curve is its fitted curve.

Table 5. The results of analytical examination of in vivo photoacoustic monitoring.

1. All time points satisfy the normality test					
2. Mauchly's test of sphericity			p > 0.05, satisfying the spherical hypothesis		
	W	p-value			
PACT	1	1			
3. Two-way repeated measures analysis of variance (ANOVA)					
	Group	Lwr	Upr	p-value	
PACT	2-1	0.96%	4.22%	0.001947088	**

*Notes：p-value: 0 '***' 0.001 '**' 0.01 '*' 0.05 '.' 0.1 ' ' 1.W is the weight of sphericity. Lwr is the lower endpoint of the confidence interval. Upr is the upper endpoint of the confidence interval.*

Since brain voltage oscillations occur across multiple frequencies, the voltage flow associated with epilepsy consists of several waves with specific characteristics. Fourier transform is often performed to interpret the properties of obtained brain electric signals [167, 168]. Analogously, the PA signal series were processed by Fourier transform to extract more correlations amongst these groups. As can be seen in the left of Figure 4-5, the epilepsy group had more high-frequency-amplitude components than the control group, similar to the high-frequency electrical signals observed in EEG monitoring during epileptic events. Regions d', e', and f', representing epileptic 1, epileptic 2, and normal status, were chosen for independent processing, and the results were shown in the right, respectively. Normal f' does not display any discernible differences, indicating that the normal status does not exhibit the same high-frequency characteristics as the epileptic status. This provides further evidence that high frequency and high amplitude are distinctive features of epileptic signals. Therefore, by examining the frequency map of the PA signals, it is possible to spectrally separate the DiSC3(5)-induced voltage signal from the PA signals originating from normal tissues. This finding suggests the feasibility of detecting epilepsy and other electrical activities in the brain based on changes in the amplitude and spectrum of VSD-induced PA signals.

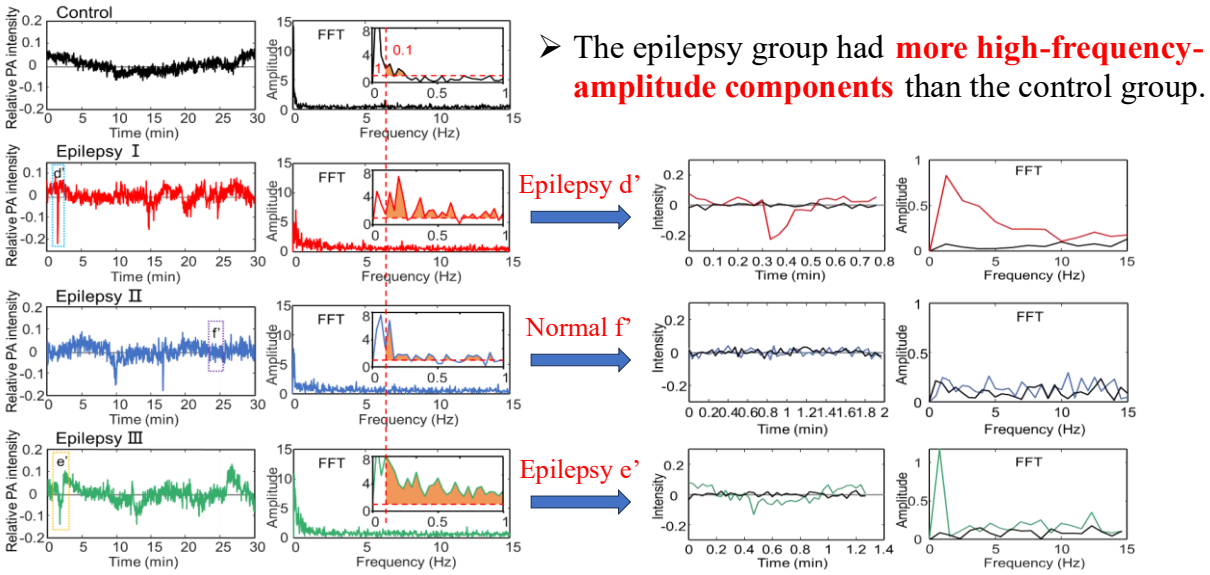

Figure 4-5. Fourier transform analysis of PA signals. The left is the time series representation of detrended PA signal and their corresponding frequency profiles for four groups (Frequency > 0.1 Hz and amplitude > 1). The right is the segmented PA signal selected on the left and their frequency profiles.

Then, we calculated the CR ($\Delta A/A_0$) to validate epilepsy. In Figure 4-6a, we selected the time series in zone 2 (Figure 4-4b) as representative of epileptic activity (marked in red), zone 3 as the calm state (marked in blue), and corresponding regions in the control group (marked in black). We adopted the ±10% interval as the baseline range for defining epilepsy because the CR in control group was more consistent and most of the change was present in this interval. The presence of bottom peaks (< -10%) suggests the occurrence of seizures, as the electrical signal exhibits a photoacoustic weak signal characteristic. As observed, the epileptic group displays a significant difference compared to the control and calm groups. To further analyse the high-frequency components, the discrete Fourier transform was applied to extract the amplitude peaks, resulting in the production of the DHF matrix. Notably, the curves for $\Delta A/A_0$ and DHF exhibit similar trends, with a peak-to-peak overlap observed in the epilepsy group. Through our examination of their correlation (Figure 4-6b), we found a strong link between the CR and DHF factors. The asterisk peaks marked in red indicate more severe epileptic pulses. Consequently, a new methodology can be established through coupling the CRs and DHF of PA signals to screen epileptic sequences.

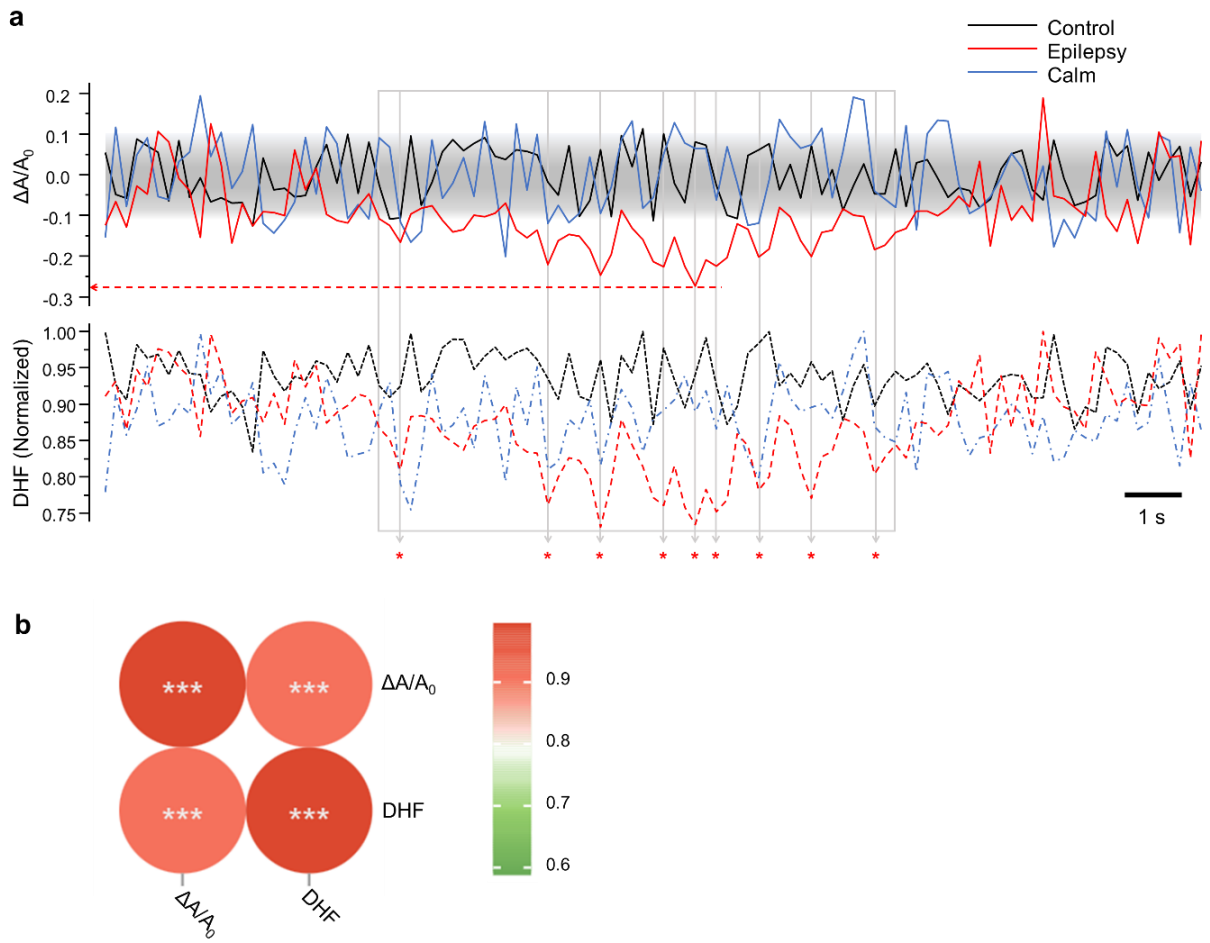

Figure 4-6. Quantitative analysis of PA signals, including the CRs and DHF factors. a) The $\Delta A/A_0$ and DHF curves. Two-peak overlapping spikes indicate more severe seizures, marked with a red '*'. b) Correlation hotmap of $\Delta A/A_0$ and DHF.

4.3.2 Functional photoacoustic brain mapping

For further investigation, we chose Zone 2 (Figure 4-4b) with obvious seizures for functional connection analysis. We first displayed the PA images. The 'Gray' image is the original image reconstruction result ("0 s" in Figure 4-7a), and the 'Jet' is the pseudo color result for the deduction of the 0 s image matrix from that at the current time point. Given that we utilized the absolute value of the image matrix, a redder hue corresponds to a more negative value and a weaker signal. As seen, there was a noticeable increase in brain activity between the 5th and 13th seconds, with bright regions demonstrating the exact localization of the seizures. Starting from the 5th second, area 1 started to light up and rapidly transmitted to areas 2 as

well as 3 at 7 s (Figure 4-7a). Then, the Allen Mouse Brain Atlas was used to identify 58 brain regions corresponding to PA brain images (Figure 4-7b) and make them separate ROIs. 210 frames of raw data were extracted, and the time series of the 58 ROIs were computed respectively. A two-by-two correlation analysis was carried out, shown in Figure 4-7c. Based on the association hotmap, the 58 brain regions could be divided into 7 categories. Sets 6 and 7 have relatively negative correlation since they are entirely composed of limbic brain regions or near the superior sagittal sinus (black dotted box in Figure 4-7c, e.g. 31, 44, 45, 29, 58 ROIs). The brain areas in sets 4 and 5 show modest correlations, suggesting that these are the much calmer regions in epilepsy and may not be involved in electrical signal transmission in this period. Electrical communication is more likely to occur in sets 1-3, which are the regions with substantial association. We were surprised to find that the active areas of the left hemisphere in Figure 4-7a coincide with the brain regions in set 3. Those regions presented certain neighboring correlations and conductance. For instance, ROI 3-5-9-8-10-13-25 formed as an electrical signal transport channel. Combined with high-temporal-resolution PA time profile, we can see the direction of transmission (red dotted arrow in Figure 4-7a and b). Next, we examined the temporal correlations of 13 brain regions in set 3 (Figure 4-7d). A great degree of coherence can be seen in all periods, which may be attributed to coordinated and fast-transmitting electrical communication. Photoacoustic electroneuron imaging may identify not only the precise location of nerve impulses but also the pathway and orientation of signal conduction through high spatiotemporal visualization.

In specific locations, we calculated the CRs of three areas, respectively (from 5-13th seconds). The results showed that area 3 exhibited the strongest epilepsy compared to the others, which suggests the presence of the most severe epileptic foci, corresponding to ROI 24,25 (Figure 4-7e). Considering that surgical treatment has been effective for some epilepsy cases in the past years, this approach could potentially assist in guiding epilepsy surgery by providing a more precise localization of the active epileptic foci.

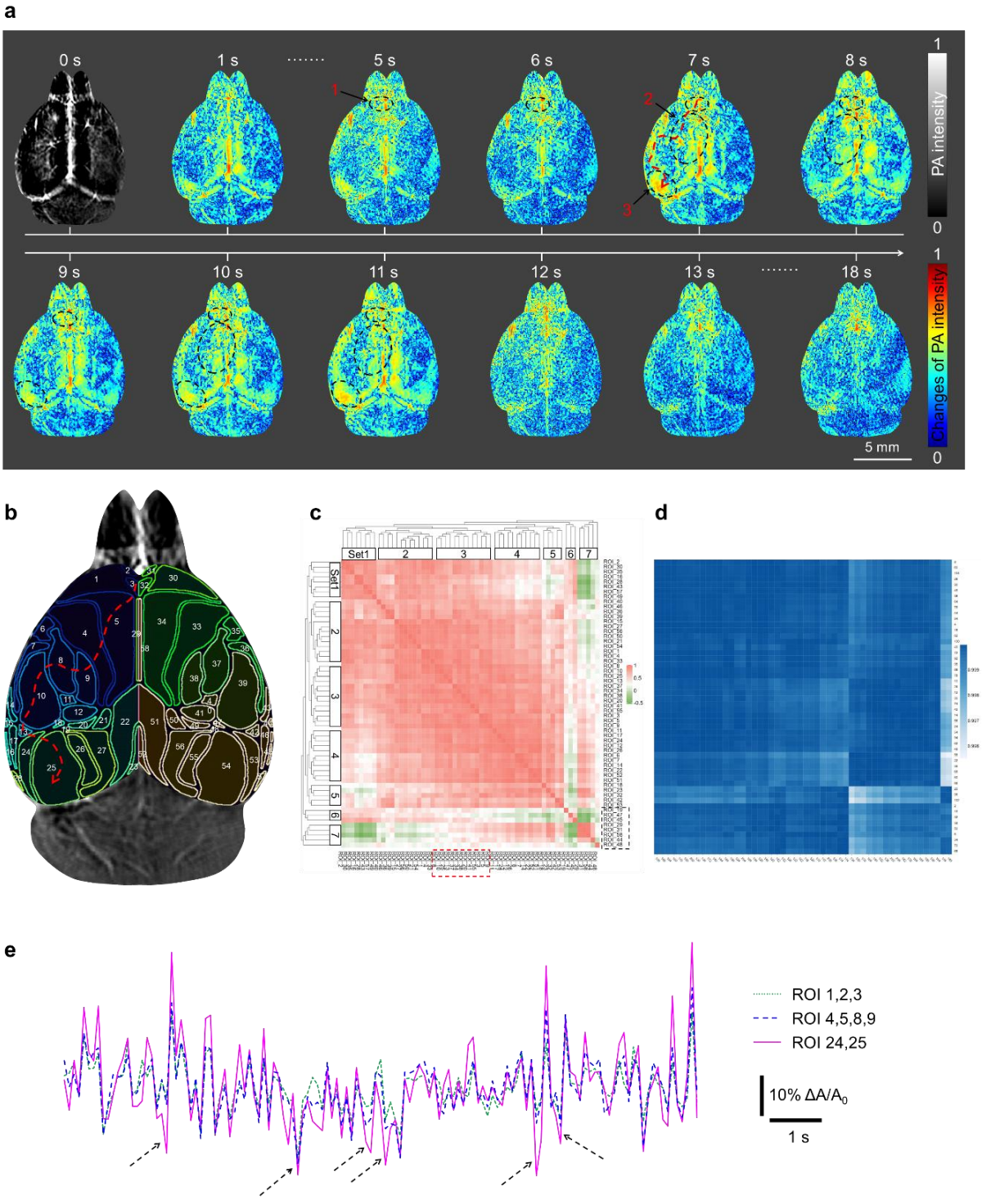

Figure 4-7. PA-VSD reveals precise location of epilepsy dynamics, as well as the pathway and orientation of signal conduction. a) Photoacoustic reconstructed images exhibited in chronological order. The changes of PA intensity distribution indicate epileptic localization, and the time series indicates the directionality of signal conduction. b) Photoacoustic image with brain regions, totaling 58 ROIs. c) Correlation analysis of two-by-two regions. d) 210-frame temporal correlation of 13 brain regions in set 3 (red dotted box in c). e) The time series of segmented 5-13th seconds, and their separated areas calculations. Area 1

corresponds to ROIs 1,2,3, Area 2 corresponds to ROIs 4,5,8,9, and Area 3 corresponds to ROIs 24,25.

All experimental results demonstrate that the PABD brain imaging system exhibits significant advantages over whole-body fluorescence imaging. It enables high-resolution, rapid dynamic imaging with high molecular specificity, thereby providing outstanding capabilities for functional brain studies.

Table 6. Comparison between FL and PABD imaging

Methodologies	**Resolution**	**Imaging speed**	**Depth**	**Field of view**	**Pros and cons**
FL imaging (IVIS)	1-3 mm	1 frame/min	Whole body	Whole body	◦ Whole-body FL quantification ◦ Low resolution ◦ Slow speed
PABD imaging	110-250 μm	10 frame/sec	~4 mm	~5 cm	◦ High resolution ◦ High speed for dynamic imaging ◦ Molecular specificity

4.4 Summary

Optical imaging methods have gained significant popularity in neuroscience in recent years [135, 169, 170]. However, acquiring in vivo signals remains a critical challenge in optical brain imaging. Traditional methods for imaging mouse brains often involve invasive procedures such as skull thinning or craniotomies, which are not suitable for clinical applications [171-174]. Additionally, strong light scattering in brain tissue limits the generation of high-resolution images at deeper levels. Although shifting to longer excitation wavelengths, such as the Near-infrared II window, can increase penetration depth, specialized fluorophores only extend the depth limit to near one millimeter [142]. Therefore, there is still

a need for the development of non-invasive, wide-field, deep-penetrating, high-resolution, high-speed, and in vivo brain imaging techniques.

In this work, VSD-type indicators are sought for, whose optical properties are tailored to directly reflect electrical impulses or membrane potentials. These indicators have been widely used for assessing cell behavior, and their safety and photostability for biological use have been extensively investigated [175-177]. One example of VSD is DiSC3(5), which we experimentally confirmed to exhibit sensitive PA and FL responses, making it suitable for brain voltage detection. Unlike gene-encoded dyes, DiSC3(5) avoids ethical concerns in human trials and clinical validation. It directly responds to voltage changes by monitoring PA and FL signals, without relying on calcium ion concentration. Importantly, the ingestion of DiSC3(5) and exposure to light are harmless to living organisms. Furthermore, our FL and PA electrodynamic tests demonstrated that it exhibited sufficient photostability (>75%) for 30-mins continuous monitoring. While full-field FL imaging offers excellent signal intensity sensitivity, its application for brain voltage monitoring is limited due to inadequate temporal and spatial resolution and the inability to provide depth information.

In contrast, PA imaging offers notable benefits and features to meet these criteria [129, 178, 179]. This work is the first trial to employ a high-spatiotemporal-resolution WF-PABD for prolonged monitoring and tracking of the VSD response to reflect brain activity in vivo. Specifically, a generalized VSD indicator DiSC3(5) was employed to conduct PA imaging under a single wavelength excitation of 670 nm, which is under a noticeably reduced blood absorption background and making the DiSC3(5) signal changes more representative of brain voltage variations. The designed platform can provide an effective FOV of about 5 cm in diameter, which is adequate to image the entire mouse brain and potentially a portion of human brain [180]. Then this platform yields an ultrahigh acquisition speed of 10 μs/frame, which can overcome the motional artifacts and hence allows for monitoring under free motion status. Considering the time needed for data transmission and storage, 10 Hz imaging speed was obtained for rapid monitoring of dynamics. Collectively, in vitro cellular studies, fluorescent in vivo imaging, and EEG research were employed to support the analysis and forecast made by PA-VSD epilepsy monitoring system. In vitro experiments demonstrated the voltage response properties of DiSC3(5). The results show a clear increase in FL intensity and a decrease in PA intensity with a growing level of depolarization. Similar signal enhancement was observed in fluorescence imaging of in vivo epileptic mice, significantly differing from the non-epilepsy and non-VSD groups, confirming that the signal changes

during seizures were triggered by VSD. In addition, we used the classical PTZ induction method to construct mouse epilepsy kindling model and performed EEG monitoring to assess the occurrence of epilepsy seizures. By employing PA-VSD, we can pinpoint the epileptic foci and determine regions with more active epilepsy activity, potentially providing guidance for surgical navigation and treatment. Interestingly, by combining high-temporal-resolution visualization and investigating brain region correlations, we obtained results on electrical conduction pathways and directions in certain regions, which can contribute to the study of nerve function and electrical conduction. Overall, we believe that the proposed PA-VSD framework can provide high-spatiotemporal-resolution visualization, accurate lesion localization, and valuable insights into brain function communication through whole-brain neuronal voltage activities, with far-reaching implications for in vivo neurophysiological investigations.

Nonetheless, there is still some space for improvement. For example, in the current configuration, the mouse's head is anesthetized and fixed in a precise position to maintain motionless in experiment, mainly due to the limitations from the structure and weight of the ring-piezoelectric-ultrasound transducer. The recent development of optical-fibre-based ultrasound sensors provides potential for future advancements towards in vivo monitoring of free-moving animals [60, 181]. Moreover, the thick and opaque shells of large mammals and the human brain pose challenges for pulsed light penetration and the generation of PA signals with sufficient signal-to-noise ratio in situ. In this regard, switching to longer wavelengths (such as far infrared regimes) and combination with fast optical wavefront shaping solutions [182, 183] will boost the penetration depth and show the potentials for deep brain imaging. This work is an early endeavor to image and monitor the electrodynamics of brain disorders, such as epilepsy. With further engineering, the platform may pave the way for visualizing and investigating into other voltage-related brain diseases, leading to impactful progress in fundamental and clinical neuroscience research.

Chapter 5 Structural Characterization of Liver Fibrosis via Photoacoustic Imaging

Chapters 5-6 are reproduced with some adaptations from the manuscript "Weiran Pang, Qi Zhou, Yang Qiu, Haofan Huang, Jiali Chen, Tianting Zhong, Yingying Zhou, Liming Nie* and Puxiang Lai*, "Multi-Parametric Photoacoustic Elastomicroscopy: Quantitative Elasticity Mapping and Microstructural Analysis for Early-Stage Hepatic Fibrosis Detection". Journal of Physics: Photonics (2025), Accepted. The contributions of authors are as follows: W. Pang, Y. Zhou, and P. Lai proposed the idea and designed the experiments. W. Pang performed the experiments, collected raw data, analyzed the data, prepared the figures for the manuscript, and wrote the original manuscript. Q. Zhou and J. Chen helped conduct part of the animal experiments. Y. Qiu helped with writing the algorithm. H. Huang, T. Zhong helped with the result discussion. L. Nie and P. Lai funded and supervised the project. All authors were involved in the analysis of the results and manuscript revision.*

Early detection of hepatic fibrosis remains a critical unmet need due to the limited sensitivity of conventional elastography in capturing microstructural and biomechanical changes. In this study, we developed photoacoustic elastomicroscopy (PAEM), a multi-parametric imaging platform that synergizes high-resolution photoacoustic microscopy with time-of-flight (ToF)-based elastography to quantitatively map tissue stiffness and visualize fibrotic microarchitecture. Validated using PDMS phantoms and a drug-induced murine fibrosis model, PAEM can detect early-stage fibrosis through microstructural biomarkers—pseudo-lobule formation and crevice-area expansion, with a relatively high area under the curve (AUC) > 0.91. However, architectural ambiguity in advanced fibrotic stages gradually reduces PAEM's diagnostic accuracy, necessitating complementary reliance on ToF-based measurements for auxiliary staging. In our results, ToF-based elasticity biomarkers revealed progressive stiffness increases with a significant velocity increase of 3.7% in 1-week fibrosis. Furthermore, experimental PAEM outperformed shear wave elastography (SWE) in early-stage sensitivity by identifying significant stiffness changes, quantitatively 7-fold greater velocity differential sensitivity than SWE (5.39% vs. 0.77% change), between healthy and 3-week fibrotic liver tissue. All-stage fibrosis exhibited considerable stiffness rise (AUC > 0.95), correlating strongly with histopathological severity and serum examination. By integrating structural and mechanical biomarkers, PAEM offers a translational tool for early

diagnosis, longitudinal monitoring, and staging of hepatic fibrosis, which can potentially be extended for wider applications in tumor margin delineation and other fibrotic pathologies in soft tissue.

5.1 Introduction to liver fibrosis detection

Liver fibrosis, a progressive condition, characterized by the excessive accumulation of extracellular matrix (ECM) proteins, is driven by chronic liver injury due to various etiologies such as viral hepatitis, alcohol abuse, and non-alcoholic fatty liver diseases [184], exemplifies this diagnostic challenge. Hepatic injury initially triggers capillarization of liver sinusoidal endothelial cells (LSECs), a structural alteration detectable through high-resolution imaging modalities. For instance, PAM has enabled monitoring of vascular architectural changes in early-stage fibrosis, revealing a significant decrease in capillary density as early as the first week post-injury [131]. This underscores the potential of early structural metrics as robust biomarkers. Subsequent hepatocyte damage initiates inflammatory responses and cell death, leading to the activation of quiescent hepatic stellate cells (HSCs). These activated HSCs undergo transdifferentiating into myofibroblasts, which excessively synthesize and secrete collagen-rich ECM components while simultaneously inhibiting matrix degradation pathways, resulting in pathological ECM accumulation. As fibrous scars progressively form bridging septa and disrupt the native lobular architecture (pseudo-lobule formation), the liver exhibits increased mechanical stiffness and functional impairment, ultimately driving the progression toward cirrhosis. This measurable change in tissue stiffness provides a distinct biomechanical parameter for diagnosis. Importantly, early-stage fibrosis remains partially reversible upon removal of the underlying etiology, highlighting the critical value of early detection. In summary, the longitudinal progression of liver fibrosis offers multi-parametric diagnostic opportunities: early structural changes and advanced mechanical alterations jointly enhance diagnostic accuracy.

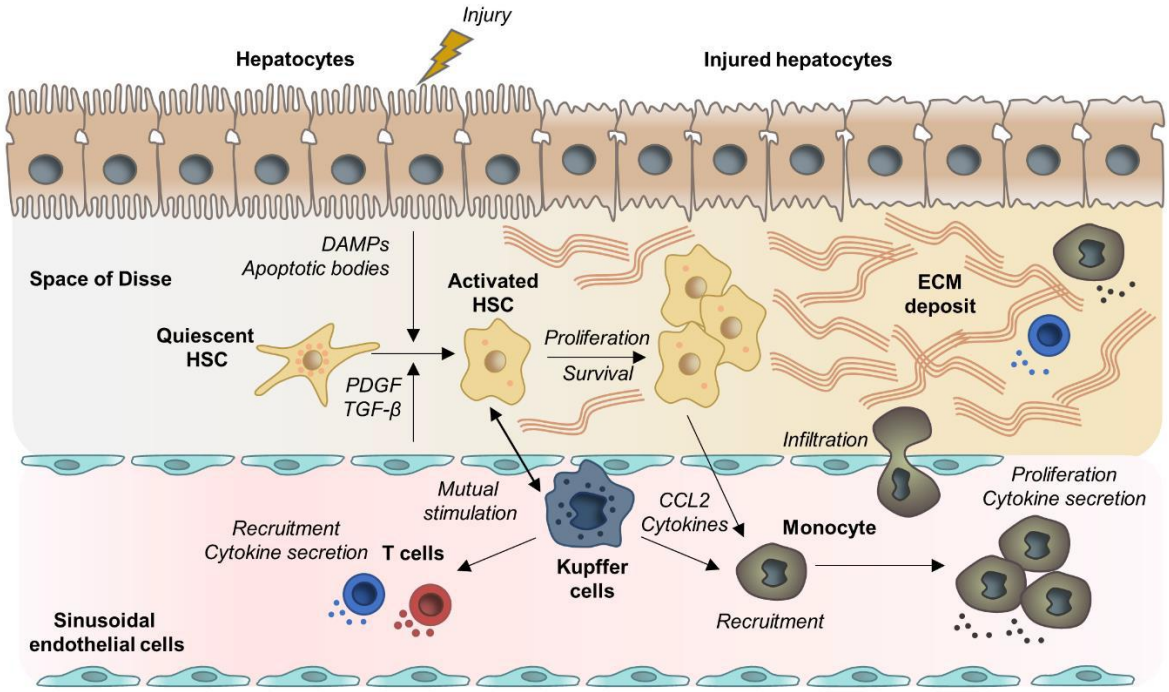

Figure 5-1. The pathogenesis of hepatic fibrosis [185]. Chronic liver injury induces the release of damage-associated molecular patterns (DAMPs) and apoptotic bodies, which subsequently activate hepatic stellate cells (HSCs) and promote the recruitment of immune cells. A network of multidirectional interactions involving activated HSCs, Kupffer cells, and innate immune cells drives the transdifferentiation of HSCs into highly proliferative myofibroblasts. These myofibroblasts are primarily responsible for excessive synthesis and deposition of extracellular matrix (ECM) proteins.

Pathologically, fibrosis begins with localized extracellular matrix remodeling that subtly alters tissue viscoelasticity – a signature undetectable by conventional elastography until cirrhosis develops [186]. Current staging relies on invasive biopsy or single-parametric imaging tools like shear wave elastography (SWE) and magnetic resonance elastography (MRE), which struggle to resolve early microarchitectural changes such as pseudo-lobule formation and diffusion collagen deposition [186-188]. Early intervention during this reversible phase could prevent progression to end-stage liver disease, yet no clinically viable method currently bridges the gap between cellular-scale biomechanics and organ-level stiffness mapping.

Given that PAI is highly sensitive to the endogenous absorption of hemoglobin, it serves as a favorable modality for vascular imaging of the liver. In this chapter, we employ PAM to

image liver tissue sections at various stages of fibrosis progression and analyze the structural features of hepatic lobules and pseudo-lobules, which can serve as one of the parameters for evaluating liver fibrosis [189].

5.2 Methods and materials

5.2.1 PAM system design

PAM is a promising imaging modality that combines the principles of PAI [100, 190] and high-resolution imaging capability. The PAM system (Figure 5-2) is a custom-built platform integrating pulsed laser excitation, high-resolution acoustic detection, and precision scanning for microstructural imaging. A Q-switched Nd: YAG laser (532 nm wavelength, 1 kHz repetition rate) serves as the light source, generating pulsed illumination with a single-pulse energy of 500 nJ (0.5 mW average power). The laser beam is expanded using a 4f optical system (L_1 and L_2 lens, 5×) to achieve uniform illumination. The expanded beam is reflected by a dichroic mirror and focused through an objective lens (NA = 0.13, working distance = 50 mm) onto the sample via a custom acousto-optic coupling module. This module features dual reflective planes to align the optical excitation path with the acoustic detection axis, minimizing signal loss.

PA signals generated by thermoelastic expansion are focused by a spherical acoustic lens in the front edge of the acousto-optic coupling module (the edge to focus is about 5 mm) and detected using a plane ultrasonic transducer (Olympus, V214-BC-RM, 50 MHz central frequency, 60% bandwidth, Japan). Signals are amplified by a 40 dB receiver (Inno Laser, China) and digitized at 500 MS/s (Alazar Tech, ATS9352).

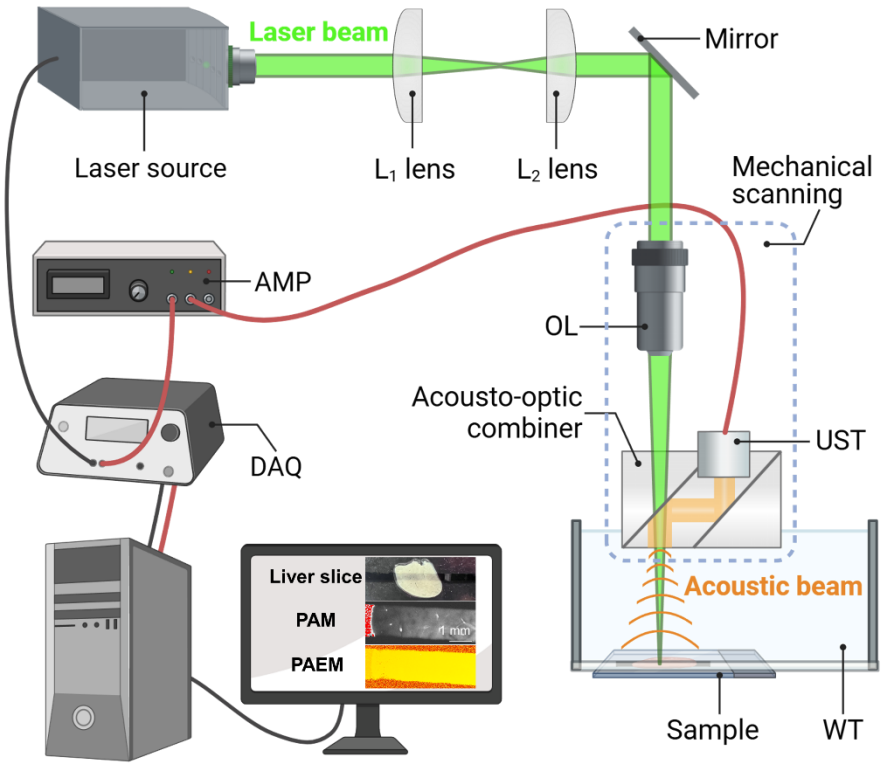

Figure 5-2. Schematic diagram of the PAM setup. AMP: Amplifier, DAQ: Data acquisition (sampling rate 500 MS/s), OL: Objective lens, UST: Ultrasonic transducer (central frequency 50 MHz, bandwidth 60%), WT: Water tank.

The lateral resolution of the PAEM system was quantified using a razor blade edge test. As shown in Figure 5-3, we acquired the maximum intensity projection (MIP) of the blade's PA image. A line profile was extracted from a region of uniform signal intensity along the blade edge (white line), and the raw data were fitted to an Edge Response Function (ERF). The derivative was subsequently subjected to single-peak Gaussian fitting. The Full Width at Half Maximum (FWHM) of the resulting Gaussian curve was calculated as the system's lateral resolution, measured at approximately 7.5 μm.

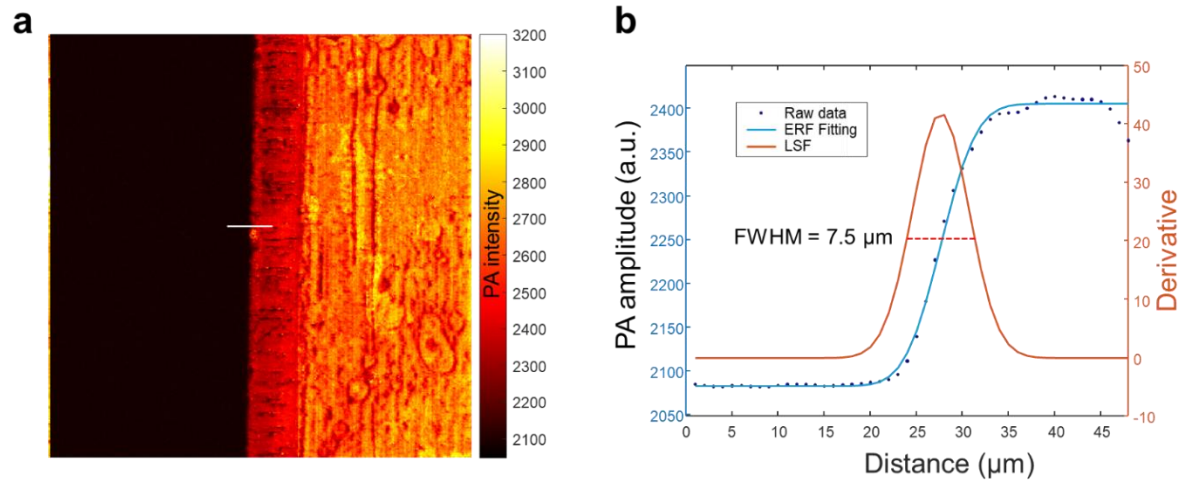

Figure 5-3. PAEM system resolution. a) PA image of a razor blade. b) The estimated system lateral resolution, measured at approximately 7.5 μm.

Then, a raw photoacoustic response perpendicular to major blood vessels was extracted (red line). Also using the ERF method, the FWHM of the fitted curve was determined as the small-vessel resolvability in the liver sections—yielding a value of 22 μm (Figure 5-4). This resolution level is sufficient for capillary-scale visualization within liver tissue sections and hold high-resolution imaging of liver.

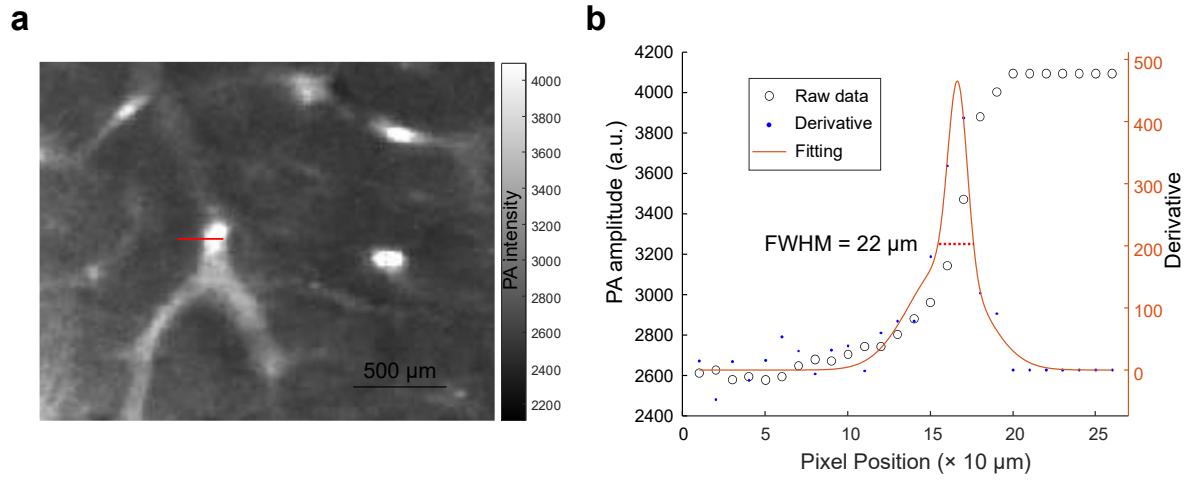

Figure 5-4. Capillary resolution estimation. a) Liver PA image with massive vascular structure. b) The estimated small-vessel resolvability, measured at approximately 22 μm.

5.2.2 Animal models and fibrosis induction

All procedures followed the National Institutes of Health Guidelines for the Care and Use of Laboratory Animals (China) and were approved by Guangdong Provincial People's Hospital (No. KY2023-1184-01). Healthy C57BL/6 mice (7 weeks old, 18-21 g, half male and half female) were purchased from the Laboratory Animal Center of Guangdong Province (China). We included about 120 mice in this study with 8 excluded due to acute hepatitis mortality. All mice were used to the typical laboratory conditions of humidity (55%), temperature (22.5 °C ± 0.5 °C), 12-hour light/dark cycle, and full access to food and water. In these mice, different stages (weeks 1-16; $n \geq 5$) of liver fibrosis were induced by intraperitoneal injection of a 20% carbon tetrachloride (CCl_4) solution (CCl_4, Macklin; 1.5 mL/kg, dissolved in olive oil at a 4:1 (Volume/v) ratio) three times per week for 1, 2, 3, 4, 6, 8, 12, and 16 weeks, respectively. Control mice were injected with olive oil (1.5 mL/kg) at the same points. These mice were evaluated 48 hours after their last CCl_4 injection to ensure the acute effects of CCl_4 did not affect the measurements and were used to assess the PAM in staging liver fibrosis. Then they were humanely killed with histologic and serum analyses after imaging.

5.2.3 Imaging protocols

PAM imaging: Fresh liver sections (300 μm thickness) are adhered to glass slides pre-marked with a 4 mm-wide black waterproof marker line. A thin layer of tissue preservation solution is applied to minimize dehydration. These samples are covered with plastic wrap stretched taut over a water tank holder, forming a sealed chamber with minimal water volume (<10 mL) to avoid pressure-induced tissue deformation. The wrap contacts the sample without compression, preserving native stiffness.

A motorized X-Y stage (X: Voice Coil Motor, SMAC Corporation, USA; Y: Stepper Motor, GMT Global Inc., Taiwan) scans the sample with 10 μm step resolution, enabling high-resolution elasticity matrix acquisition across multiple axial planes. We calculated the imaging resolution as approximately 22 μm, enabling the clear visualization of liver microvasculature with vessel diameters around 30 μm. The scanning head is fully submerged in a water chamber to ensure acoustic coupling. Each 10×10 mm^2 FOV is acquired at a B-scan rate of 5 Hz, requiring 3.3 minutes per full C-scan. A-line signals are sampled at 512 points per scan line. Raw PA signals are processed using a custom algorithm in MATLAB (MathWorks) to reconstruct MIP maps.

5.2.4 Histological and serum analysis

All model animals were sacrificed on the third day following the completion of modeling injections at weeks 1, 2, 3, 4, 6, 8, 12, and 16 ($n \geq 5$ per time point). Blood and liver tissue samples were subsequently collected. Anticoagulated blood was left to stand at room temperature for 2 hours, followed by centrifugation at 4°C, 3000 rpm, for 10 minutes to obtain the supernatant. The supernatant was labeled and stored temporarily at -80°C. After two days of freezing, the samples were sent to a testing laboratory (Wuhan Servicebio Technology Co., Ltd.) for the measurement of Alanine Aminotransferase (ALT) and Aspartate Aminotransferase (AST) levels, which are both important biomarkers for assessing liver function and detecting liver fibrosis.

The freshly excised liver tissues were washed with saline to remove any residual blood, weighed, and photographed. They were then divided into two groups. The first group was placed in a MACS tissue storage solution (Miltenyi, Order No.: 130-100-008) and temporarily stored in an ice box. Subsequently, the liver tissues were sliced into 300-micron thick sections using a vibrating blade microtome (Leica Biosystems, VT1000 S, with a blade travel speed setting of 0.05 mm/s and vibration frequency of 70 Hz and positioning resolution < 1 μm). The freshly cut liver sections were immediately placed under a PAM device for scanning and data collection to ensure the liver's stiffness remained consistent with its physiological state. The other group was placed in a container filled with 4% paraformaldehyde fixation solution and stored at 4°C for preservation. Once all liver tissues from the animals (1-16 weeks models) were collected, they were sent to a biological services company (Wuhan Servicebio Technology Co., Ltd.) for HE staining, Masson staining, and scanning, ensuring consistency in the staining background.

5.2.5 Data processing and statistics

PA images were reconstructed as MIP maps of PA signals. In structural analysis, low-absorption regions corresponding to collagen fiber crevices were extracted from the PA image via thresholding to generate a binary mask. Using distance transform-derived watershed seed points, a gradient-modified watershed algorithm segmented these regions as irregularly shaped pseudo-lobules. Randomized color coding was applied to adjacent regions to prevent chromatic ambiguity. Pseudo-lobular features were subsequently quantified via area-equivalent diameter measurements.

5.3 Results: Structural differentiation between healthy and fibrotic liver tissues

The physiological results show that, as fibrosis worsens, the liver surface exhibits an uneven, granular texture (Figure 5-5a and b). Histopathological staining remains the gold standard for fibrosis diagnosis. As shown in Figure 5-5c, Masson's trichrome staining reveals an increase in fibrous collagen (blue staining), which divides the hexagonal hepatic lobules into multiple small, irregular pseudo-lobules. This represents one of the common structural alterations associated with liver fibrosis. Then, we calculated the collagen proportionate area (CPA) of the liver staining, which also increases with the fibrosis advancing (Figure 5-6).

In addition to microstructural changes, we also recorded body weight and organ wet weight during the progression of liver fibrosis. Although fibrotic mice display significantly lower body weights compared to normal controls, the fibrotic liver becomes enlarged in later stages (Figures 5-7). The observed organ enlargement was consistent with the pathological course of the disease. Elevated serum ALT and AST levels further indicate hepatic inflammation and injury (Figures 5-8). ALT and AST are two common biomarkers of liver injury. From the onset of modeling, both ALT and AST levels exhibited a sharp increase during the initial weeks, likely due to drug-induced fibrosis triggering the liver's intrinsic protective mechanisms as it attempted to repair the damage. However, during the later stages (weeks 12-16), both ALT and AST levels slightly declined, indicating irreversible liver damage. This pattern has been consistently reported in multiple studies on liver fibrosis [131].

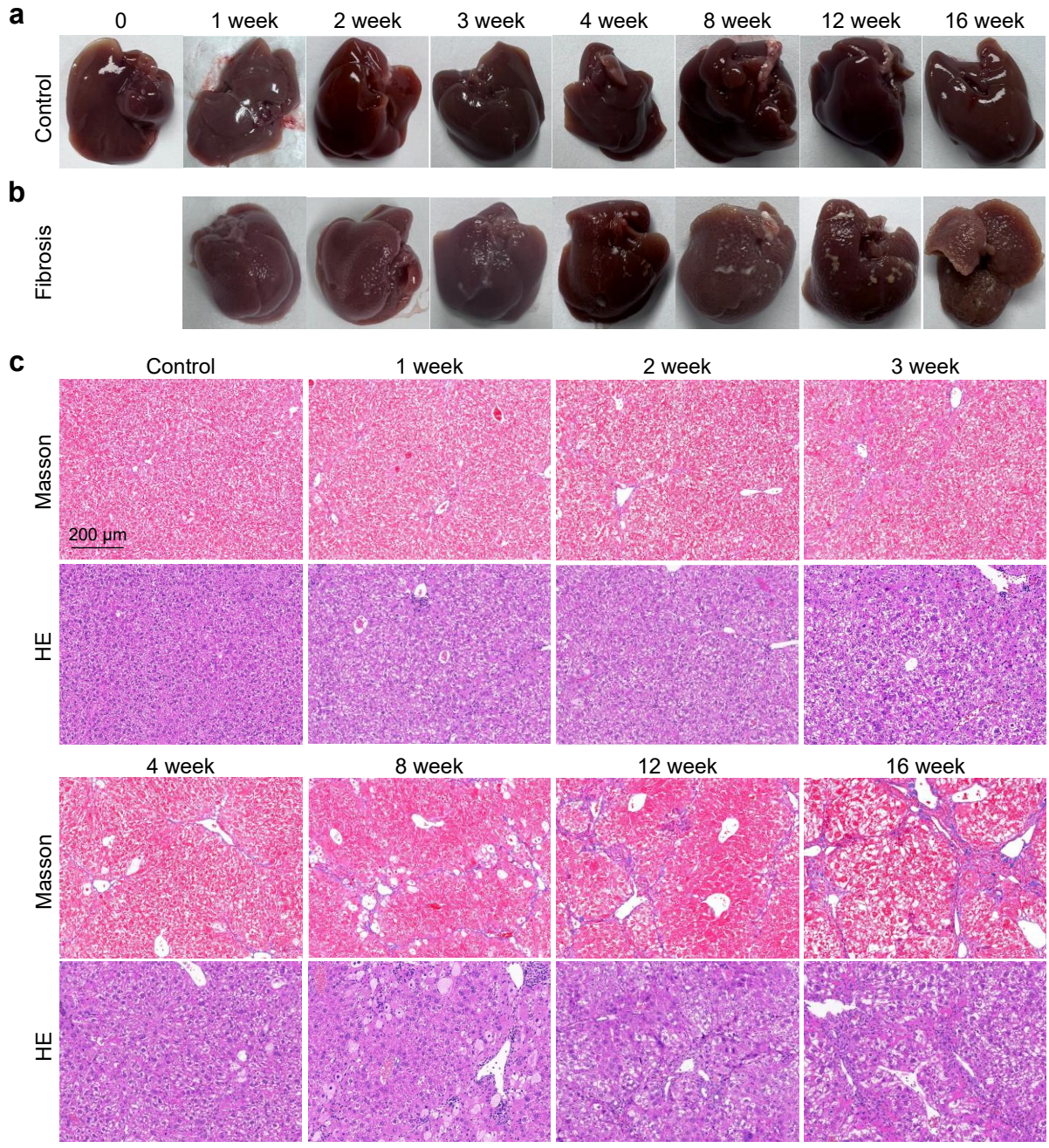

Figure 5-5. Progress in hepatic fibrosis modelling and histological validation. a) Liver surface image of the Control group. b) Liver surface image of the Fibrosis group. c) Corresponding liver tissue sections stained with H&E and Masson's trichrome. With progressive hepatic fibrosis, the liver surface becomes increasingly uneven. Histological sections reveal collagen fiber proliferation (blue staining), with hepatic lobules gradually disrupted and replaced by pseudo-lobules.

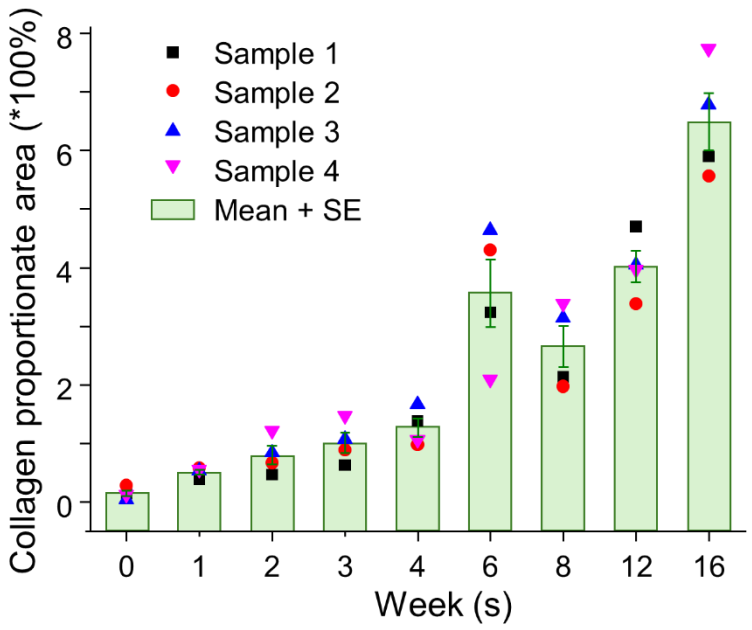

Figure 5-6. Quantification of CPA by Masson's staining. Each group included four samples, and the results showed a gradual increase in collagen fiber area percentage, indicating progressive fibrosis.

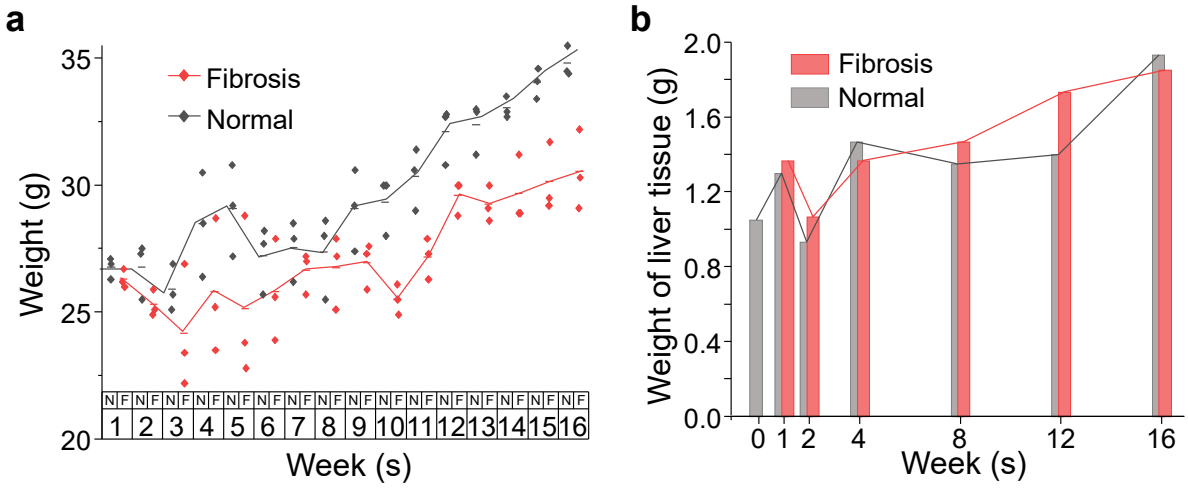

Figure 5-7. Body weight and liver wet weight of modelled mice. a) Body weight. b) Liver wet weight.

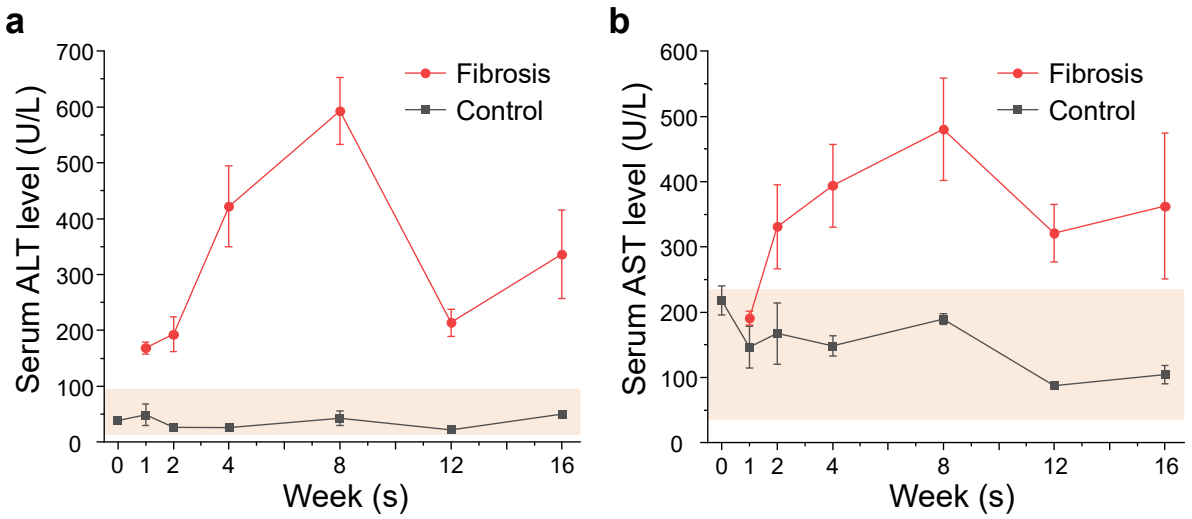

Figure 5-8. Serum biochemical indicators of liver function in modelled mice. a) ALT. b) AST.

Then, we conducted PAM imaging of fibrotic liver sections. Fresh liver tissues were sectioned uniformly into 300-μm thick slices using a vibratome. These slices were then carefully laid on glass slides marked with a black marker. As illustrated in Figure 5-8, the PA structural images reveal the formation of additional pseudo-lobules. We employed an algorithm to extract the skeleton of the pseudo-lobule crevices, hereafter referred to as "Crevices". The first column displays the original PA MIP images, from which a ROI approximately 6 × 5 mm² was selected. Using the algorithm, we extracted the skeleton of the crevices, which closely resembled the structure of accumulated collagen fibers (Figure 5-5). These crevices likely partition the hepatic lobules into multiple pseudo-lobular structures. The third column shows the merged images, clearly demonstrating that the crevices precisely correspond to the dark regions in the PA images. Based on these skeletons, we segmented the internal architecture of the liver section and applied random color encoding to each region, as shown in the fourth column. These segmented structures were interpreted as hepatic lobules or pseudo-lobules. We then measured the maximum diameter of each structure and used a normal distribution to statistically analyze the number of lobules/pseudo-lobules within different diameter intervals. The results indicated that as fibrosis progressed, collagen fiber accumulation disrupted the original lobular architecture, forming multiple irregularly shaped pseudo-lobules. Moreover, the diameters of these pseudo-lobules gradually decreased with

disease severity. This observation was consistent with histological validation from tissue sections.

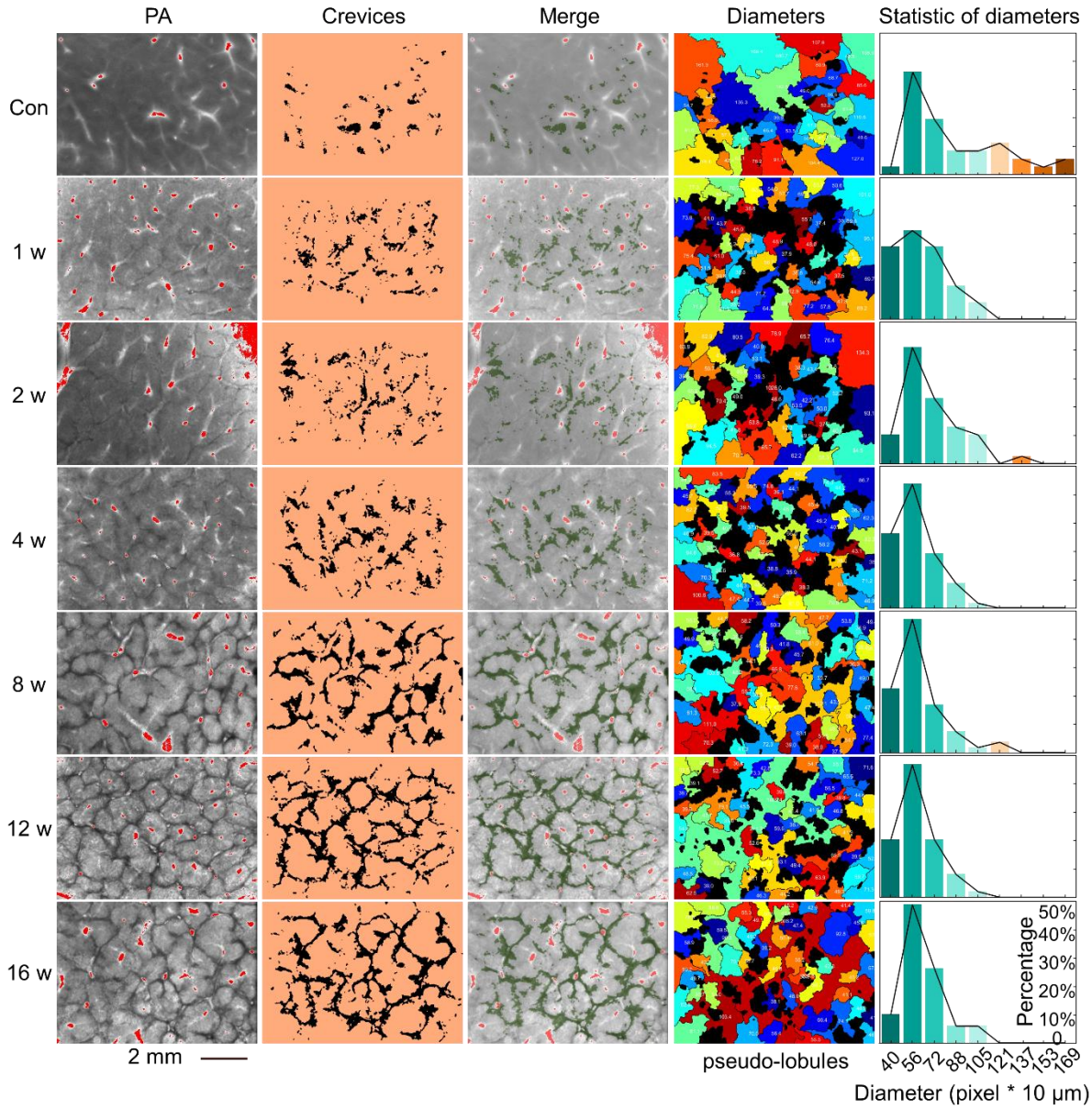

Figure 5-9. PAM structural imaging reveals microarchitectural remodeling in fibrotic liver sections. In progressive fibrosis stages (control, weeks 1-16), pseudo-lobule formation (color-coded regions) and crevice expansion (white arrows) are evident as fibrosis advances.

After that, we calculated the crevices area and relative proportion, observing a relatively linear increase (Figure 5-10a), which is in line with the CPA calculations. As observed in the maximum diameter of pseudo-lobules, the most frequently observed diameter was 560.6 μm; as fibrosis progressed, the overall lobule diameters gradually decreased while the proportion

of regions with a 560.6-μm diameter increased (Figure 5-10b). Finally, we analyzed the distribution of these diameters based on a normal distribution. The fitted curves indicated that early-stage liver fibrosis (1-4 weeks) could be distinctly differentiated, whereas advanced fibrosis (4-16 weeks) exhibited no clear pattern or significant differences (Figure 5-11). These results indicate that relying solely on changes in liver structure, such as the area of Crevices and diameter statistics, allows for the detection and distinguish of early-stage fibrosis. However, advanced liver fibrosis obscured structural patterns, necessitating complementary elasticity metrics for accurate staging.

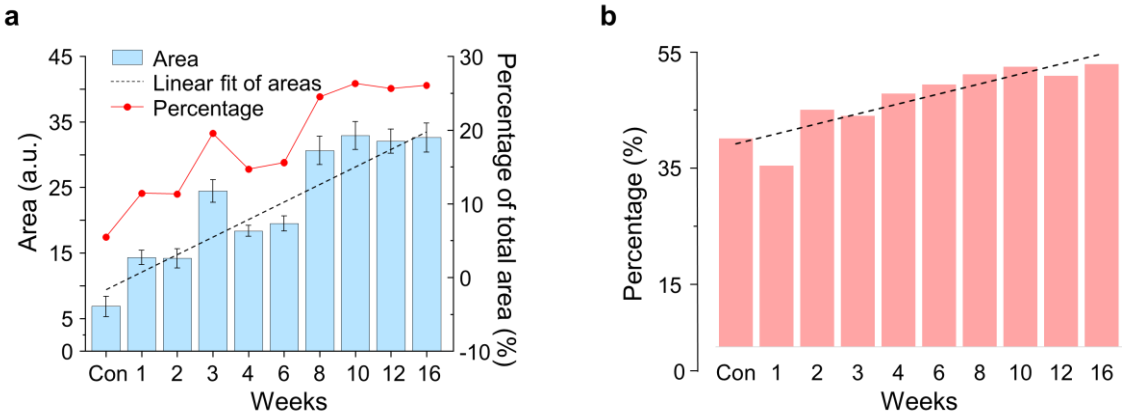

Figure 5-10. Quantitative analysis of crevices and diameters. a) Quantification of crevice area proportion shows a linear increase during mild to moderate fibrosis (weeks 1-6), plateauing in advanced stages. b) Histogram of pseudo-lobule diameters identifies a dominant size (560.6 μm), with reduced mean diameters in early fibrosis (dashed line).

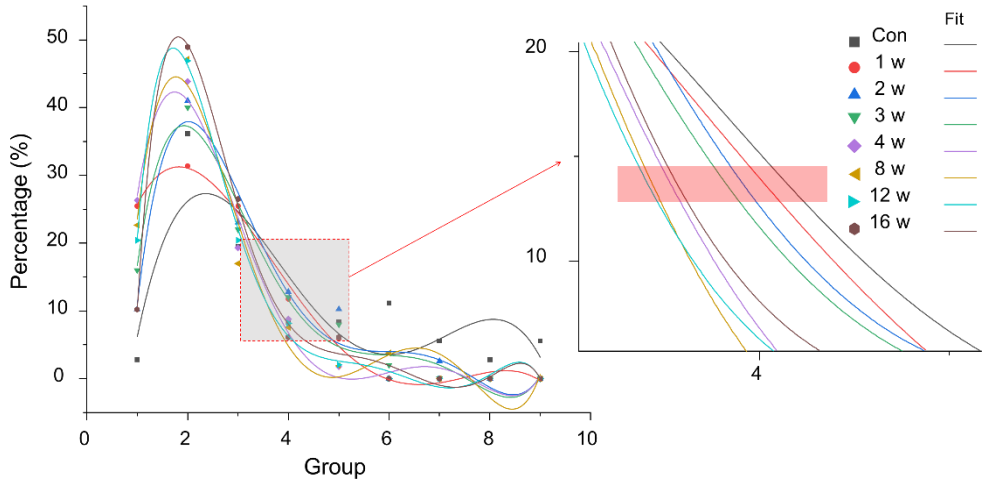

Figure 5-11. Normal distribution fitting of diameters highlights distinct clustering in early stages (weeks 1-4) versus overlapping distributions in advanced fibrosis (weeks 4-16).

5.4 Discussion and summary

The liver is a vital organ responsible for metabolism, detoxification, secretion, and storage. However, it is often referred to as a "silent" organ, as early-stage damage typically presents without symptoms and is easily overlooked, as in conditions such as hepatitis, fatty liver disease, and liver fibrosis. Various diseases can induce fibrotic proliferation, altering the physiological state of the liver in terms of both structure and biomechanical properties. Therefore, early detection and intervention are critical for liver disease reversal, given the liver's remarkable regenerative capacity. Current clinical imaging modalities are limited in their ability to assess liver pathology at the microstructural level. As the liver is highly vascularized, numerous studies have shown that microstructural changes often preceded other external manifestations in the early stages of liver disease [131]. Accordingly, this chapter proposes the use of high-resolution PAM to analyze liver microstructure, offering potential advantages for early disease diagnosis.

In this chapter, we performed high-resolution PAM scans on liver sections with varying degrees of fibrosis. With a resolution of up to 7.5 μm, PAM is capable of identifying most microvasculature in liver. During fibrosis progression, collagen fiber proliferation disrupts the original hepatic lobular architecture, resulting in the formation of multiple pseudo-lobules. In PA images, collagen fibers appear as low-absorption (dark) regions, and their distribution corresponds well with histological sections. The total area of these dark regions increases with fibrosis severity. The diameters of hepatic lobules and pseudo-lobules gradually decrease, with the main distribution centered around 560.6 μm. Furthermore, we observed that early-stage liver fibrosis (weeks 1–3) could be clearly distinguished based on the fitted diameter distribution curves. However, this distinction becomes less apparent in the mid-to-late stages. These findings suggest that microstructural analysis alone may not be sufficient for comprehensive disease diagnosis; instead, it should be complemented with additional parameters—such as biomechanical measurements—to enable full-stage evaluation of liver fibrosis.

Chapter 6 Elasticity Assessment of Liver Fibrosis and Hepatocellular Carcinoma Using Photoacoustic Elastomicroscopy with Time-of-Flight (ToF)

6.1 Brief review of elastic imaging techniques

6.1.1 Conventional elastography methods

Tissue elasticity has emerged as a crucial biomarker for early disease diagnosis, with pathological stiffness often preceding macroscopic structural changes in conditions such as cancer and fibrosis. While palpation historically provided the first clinical insights into tissue mechanics, its subjective nature and lack of quantification [191-193] spurred the development of elastography techniques, including magnetic resonance elastography (MRE), ultrasound elastography (USE) [194] and optical coherence elastography (OCE). Among these, MRE enables noninvasive stiffness mapping but suffers from limited spatial resolutions (~1 millimeter), hindering its ability to detect microstructural collagen deposition in early liver fibrosis [194, 195]. Furthermore, the substantial capital expenditure and per-procedure operational costs have constrained clinical adoption compared to USE. Ultrasound-based methods like shear wave elastography (SWE) and transient elastography (TE) offer real-time quantitative imaging but also face limited resolution. Evidence indicates that both MRE and SWE, when optimized with appropriate diagnostic thresholds, achieve sensitivity around 90% for detecting advanced-stage fibrosis [196], however lose accuracy in early-stage fibrosis and obese patients, where stiffness gradients are subtle and heterogeneous [197]. Conversely, OCE is achieves micron-scale resolution but is restricted to superficial tissue regions such as ocular tissues and skin due to optical scattering [198, 199]. Investigators quantified shear wave OCE sensitivity by assessing velocity variance in repeated phantom measurements, demonstrating reliable detection of shear wave speed (SWE) changes below 4% with statistical significance [200, 201]. Atomic force microscopy (AFM) provides nanoscale mechanical characterization but remains invasive and incompatible with in-vivo applications

[202]. These limitations underscore the unmet needs for a modality combining deep-tissue penetration, microscopic resolution, and multi-parametric sensitivity to both structural and mechanical biomarkers.

6.1.2 Photoacoustic elastography in biomedicine

As an emerging variant based on the PA effect, photoacoustic elastography (PAE) utilizes laser-induced ultrasound signals to encode both optical absorption and mechanical properties [203]. Current PAE implementations can be categorized into three paradigms: stress-strain analysis, where external mechanical loading is applied to measure tissue deformation via photoacoustic tracking [204-206]; phase/frequency-domain methods, correlating viscoelastic properties with phase delays or resonance frequency shifts in photoacoustic waveforms [207, 208]; time-of-flight (ToF) or time-domain techniques, exploiting sound speed variations in tissues to infer stiffness changes [209, 210]. Stress-strain PAE, exemplified by Hu *et al.* [206], quantifies absolute Young's modulus by analyzing displacement fields under controlled compression. While effective for skin and breast tissues, this approach struggles in soft, fluidic organs like the liver due to challenges in achieving uniform stress distribution and avoiding tissue damage [211]. Phase-domain methods, such as Yang et al.'s elasto-viscography [207] detect stiffness differences by measuring the laser-induced thermoelastic phase delays. Although sensitive to microscale viscoelasticity, these methods require complex signal processing and high-frequency transducers, limiting their depth penetration in turbid tissues [208]. Time-based PAE, as demonstrated by Yuan *et al.* [209] offers non-contact elasticity sensing by analyzing the ultrasound propagation delays. However, existing implementations lack microscopic resolution (>500 μm) and fail to integrate structural biomarkers (e.g., collagen architecture) with mechanical readouts—a critical gap for detecting early fibrosis where microstructural remodeling precedes bulk stiffness changes [131, 212]. Furthermore, most PAE systems focus on single-parametric elasticity metrics, neglecting the synergistic diagnostic value of combining mechanical and morphological data. For hepatic applications, these limitations are compounded by the liver's acoustic heterogeneity and the sub-millimeter scale of early fibrotic features (*e.g.,* sinusoidal capillarization, sub-300 μm pseudo-lobules) [131], which conventional PAE cannot resolve.

Table 7. Comparison of conventional elastography methods

Technologies	Principle	Resolution	Penetration depth	Imaging speed	Pros & cons
MRE	A vibrating plate induces shear waves into the body. A modified MRI sequence images the wave propagation.	~1 mm	Whole organ (unlimited by depth)	Slow (Several minutes)	✓ Can assess entire liver volume × Slow × Expensive
USE: SWE and TE	**SWE:** Shear waves are acoustically pushed into tissue + shear wave speed (SWS: faster in stiff tissue) is measured.	1-5 mm	2-6 cm	Fast (Real-time)	✓ Inexpensive ✓ Widely available ✓ Real-time × Low sensitivity in early stage
	TE: A mechanical vibration creates a shear wave + SWS is measured.	~1 cm	2-6 cm	Very Fast (Single measurement)	
OCE	Uses the coherence gating of light (OCT) to measure microscopic tissue displacement in response to a mechanical or acoustic stimulus.	1-10 µm (Cellular level)	1-2 mm	Fast (but small FOV)	✓ Ultra-high resolution ✓ Ideal for research & ophthalmology × Shallow depth
PAE	Thermoelastic expansion generates an ultrasound wave. Stiffness affects the phase, amplitude, frequency or time of flight (ToF) of this signal.	5-200 µm	1-3 cm	Moderate	✓ Unique biochemical specificity (can target chromophores like collagen) ✓ Combines functional/ molecular contrast with mechanical data

6.1.3 Motivation

Addressing the critical limitations of single-modality investigation by traditional PAE or microstructural analysis with PAM mentioned in Chapter 5, in this chapter, we introduce photoacoustic elastomicroscopy (PAEM), a high-resolution platform integrating ToF-based elasticity mapping with microstructural analysis for multi-parametric liver fibrosis

assessment, positioning PAEM as a translational tool for fibrosis staging, tumor margin delineation, and therapeutic monitoring. By synergizing PAM's optical resolution (~7.5 μm) with acoustic wave propagation physics, PAEM simultaneously quantifies stiffness gradients and visualizes fibrotic microarchitecture in a label-free manner [189]. We validate PAEM's precision using phantoms with tunable mechanical properties and demonstrate its clinical utility in a longitudinal murine fibrosis model. Our results establish PAEM's superiority over SWE in early-stage detection and achieve quantitative fibrotic measurement of full stage, enabled by correlating crevice-area expansion (structural biomarker) with ToF-derived stiffness progression (mechanical biomarker). This dual-parametric approach addresses the critical limitations of single-modality elastography, positioning PAEM as a translational tool for fibrosis staging, tumor margin delineation, and therapeutic monitoring.

6.2 ToF principles and methods of elasticity measurement

6.2.1 ToF-based PAEM measurement

PAEM uses the PAM system in Chapter 5 and leverages ToF differences to quantify relative stiffness variations in liver tissues. When pulsed laser irradiates the liver sample, the black marker background absorbs the light and generates ultrasonic signals via the thermoelastic effect; the weak absorption of the liver section is negligible in comparison. The ultrasound propagates through the liver slide and travels back to the ultrasound transducer, with the propagation time defined as ToF. However, due to variations in stiffness within the liver samples, the ultrasound velocity differs, leading to variations in propagation time within the tissue and, consequently, differences in arrival time at the ultrasound transducer. A single B-scan should ideally encompass both the signal cover with the liver section and the background region without liver tissue (Figure 6-1a). To quantify the differences, we calculate ToF_1 in the background region and ToF_2 in the sample section, and the difference between them ($\Delta ToF = \left| ToF_1 - ToF_2 \right|$) serves as a proxy for stiffness, with shorter ToF indicating higher sound speed and greater tissue rigidity (Figure 6-1b). This approach offers a high resolution as traditional OR-PAM, integrating structural and biomechanical properties for fibrosis assessment. So, PAEM provides multi-parametric capabilities of simultaneous cellular-scale structure visualizing and organ-level stiffness mapping.

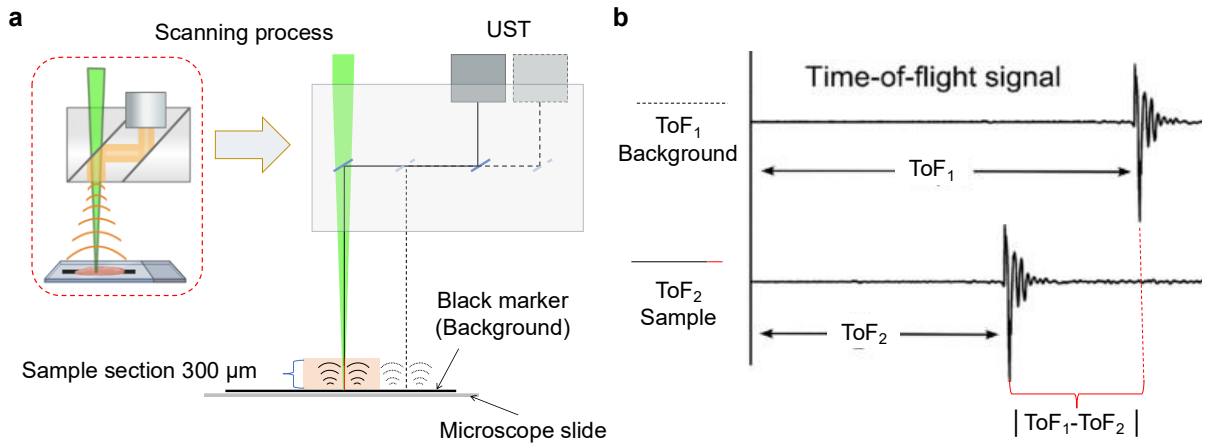

Figure 6-1. ToF-based elasticity measurement principle. a) Representative B-scan of a liver section, highlighting ToF differences between the background (black marker, ToF_1) and sample section (ToF_2). b) Calculation of ΔToF ($|ToF_1 - ToF_2|$), reflecting ultrasound velocity variations due to sample stiffness.

6.2.2 Study design

As shown in Figure 6-2, we assessed the degree of liver fibrosis based on the comprehensive evaluation of multiple parameters and to investigate whether the proposed PAEM could serve as an effective tool for sensing and diagnosing liver fibrosis. The diagram illustrates the integration of PAEM with histopathological and serum biomarker analyses in a CCl4-induced liver fibrosis mouse model. Similarly to the animal experiments in Chapter 5, we established a drug-induced liver fibrosis mouse model by regularly administering a mixture of CCl_4 and olive oil via intraperitoneal injection. Then, various parameters were recorded at different time points, including body weight, liver wet weight, serum liver function markers, and liver histology. Additionally, we performed PAEM imaging of the liver, key stages include: (1) PAEM imaging of 300-μm thick liver sections to capture structural changes (e.g., pseudo-lobule formation and crevices area), (2) elasticity mapping via ToF-based measurements and clear margin delineation, and (3) correlation of PAEM-derived stiffness and microstructural metrics with histology (Masson's trichrome staining) and serum liver function markers (ALT/AST). This multi-parametric approach enables comprehensive detection of early fibrosis progression while demonstrating strong correlation with established diagnostic standards. PAEM's unique capacity to integrate structural, biomechanical, and biochemical data offers complementary value to conventional methods, highlighting its potential for non-

invasive longitudinal monitoring of hepatic fibrosis. This synergistic capability facilitates more timely diagnosis and precise staged management of fibrosis progression.

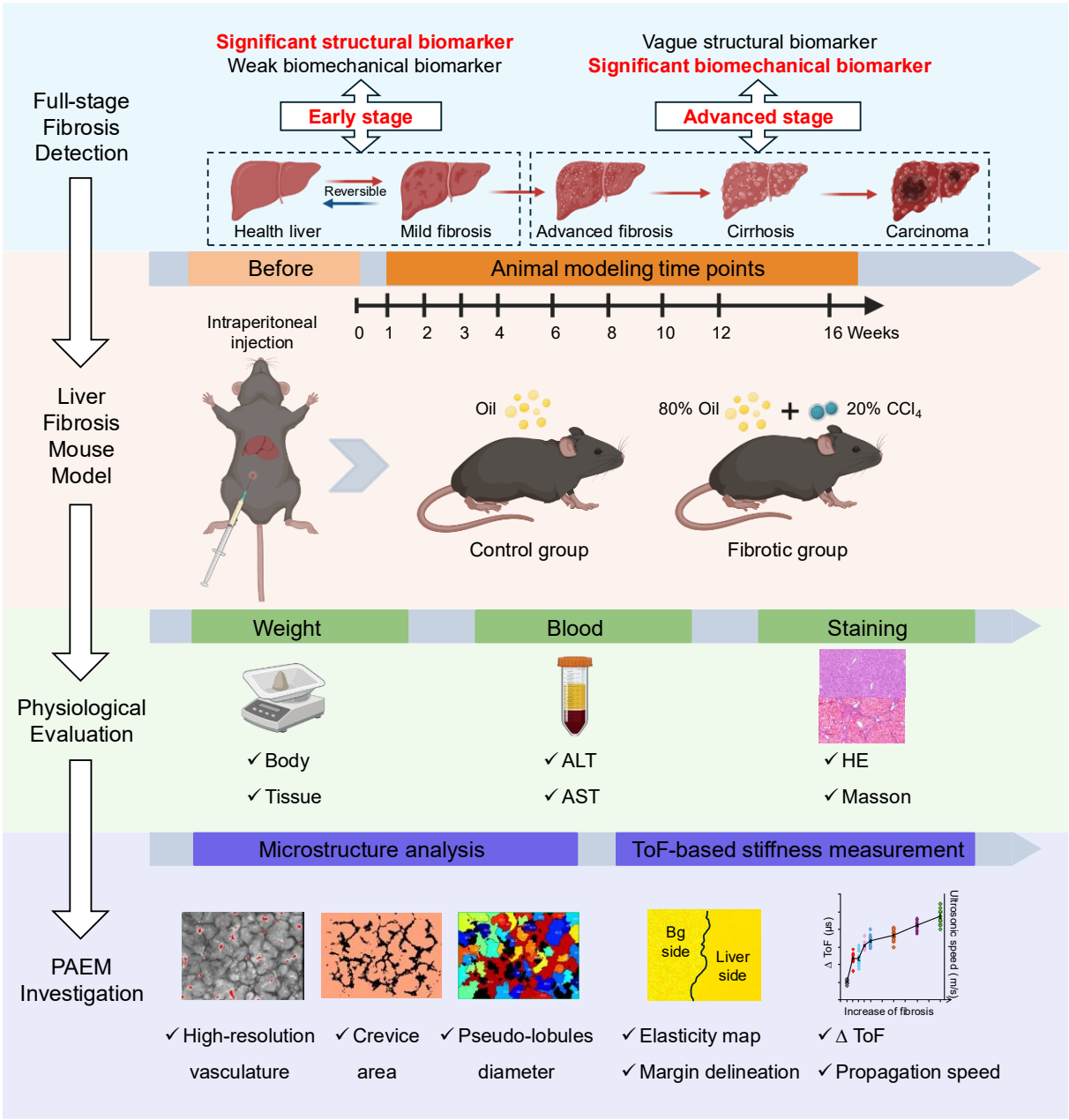

Figure 6-2. Schematic workflow of multi-parametric PAEM imaging and sensing for mouse liver fibrosis assessment. Using CCl_4-induced hepatic fibrosis models (stages: 1-16 weeks), we implemented a multi-parameter diagnostic strategy. During early stages (1-4 weeks), high-resolution PAEM structural analysis was prioritized to detect microarchitectural alterations—which precede measurable biomechanical changes—as primary biomarkers. In advanced stages (> 4 weeks), where tissue stiffening supersedes structural evolution, ToF-based elasticity measurements quantitatively tracked mechanical property progression. Fibrosis staging throughout the disease continuum was validated against histopathological

grading and physiological parameters, demonstrating the significant advantage of our multiparametric approach for comprehensive fibrosis assessment.

6.2.3 Phantom preparation

Five polydimethylsiloxane (PDMS, Sylgard 184, Dow Inc., Midland, MI, USA) phantoms mimicking liver stiffness gradients were fabricated by varying the base-to-curing agent ratios (Weight/w): M1 (4:1), M2 (6:1), M3 (10:1), M4 (14:1), and M5 (18:1). These mixtures were stirred at 200 rpm for 15 minutes using a magnetic stirrer to ensure a homogeneous mixture. Then, the mixture was left to stand at 4°C for 2 hours before being cast into pre-designed rectangular molds (grooves dimensions: width 10 mm × length 50 mm × thickness 300 μm). Finally, the samples were placed in a vacuum chamber and cured at room temperature for 48 hours to achieve complete crosslinking, which different stiffness films could be obtained.

6.2.4 Imaging protocols

SWE: Healthy and 3-week fibrotic mice were used to perform SWE imaging. Animals were anesthetized with 1% VOL isoflurane, gas flow rate of 1 cm^3/s. All mice underwent SWE examinations at a frequency of 18 MHz using Canon Aplio i900 Ultrasound System (Canon Medical System, Japan), equipped with a i18LX5 plane probe. The imaging depth was fixed at 3 cm, and the circle region of interest (ROI) diameter was set to 3 mm. The 2D SWE image was shown as a color-coded signal overlaying with the B-mode image. 13 ROIs were performed to determine the liver stiffness measurements (LSM) values. The color-bar of the SWE image ranged from 0 to 85 kPa.

PAEM imaging: It is identical to the settings as PAM imaging in 5.2.3. ToF elasticity maps were computed as $\Delta ToF = ToF_{background} - ToF_{liver}$, which reflects the variation in sound speed across different liver regions. This relationship can be further expressed as $\Delta ToF = d/v_{background} - d/v_{liver}$, where d presents the sample thickness. Accordingly, assuming an ideal sound speed of 1500 m/s in water ($v_{background}$), the acoustic velocities within different liver lobes can be quantitatively estimated.

6.2.5 Data processing and statistics

SWE examinations and LSM values were obtained from the system-installed software. PA images were reconstructed as MIP maps and ToFs were calculated with mean maximum peak of PA signals. All PA data was processed with algorithms developed by us based on MATLAB. ΔToF was calculated with the formula $ToF_{background}$ - ToF_{liver}, where six ROIs of 500 * 500 μm were randomly selected in each sample (three for background and three for liver). In each group, there were 11-25 samples used for calculation of mean values and their standard error. ΔToF values analyses were performed with Shapiro-Wilk test, and the comparisons between groups were based on a one-way ANOVA procedure in OriginPro 2022. Incorporating leave-one-out cross-validation (LOOCV) in ROC curve analysis for AUC computation significantly enhances the robustness of diagnostic model performance evaluation. Some icons in the schematic were from BioRender. All curves were produced using OriginPro 2022.

6.3 Validation results and discussion

6.3.1 SWE examination of liver fibrosis

SWE was employed to image the livers of normal mice and mice subjected to a three-week liver fibrosis induction model. The ultrasonic probe was moved transversely from the upper abdomen (around the xiphoid process) to the lower abdomen (above the bilateral kidneys) for continuous imaging. In B-mode, the liver structure was visualized, while the SWE mode displayed the liver stiffness as a color-coded map (Figure 6-3a, b). Measurements were performed 13 times for each subject across three distinct imaging planes. In each plane, a 3-mm diameter ROI was chosen in areas of relatively homogeneous liver parenchyma for calculation and statistical analysis. All ROIs were maintained at consistent anatomical positions whenever possible. However, when vascular structures or connective tissues were present within the imaging plane (which may confound elasticity values), ROIs were repositioned to more homogeneous areas of hepatic parenchyma to ensure measurement accuracy (see Position 3 in Figure 6-3a).

The limited spatial resolution of SWE (commonly used in clinic) precludes its ability to resolve microstructural features, as it primarily infers Young's modulus elasticity values through measurements of shear wave speed (SWS) within tissues. Early-stage liver fibrosis is characterized by predominant microstructural remodeling rather than quantifiable elasticity

alterations. This fundamental pathological progression renders SWE insensitive to incipient fibrotic changes—both structurally and in terms of measurable elasticity variations—during initial disease phases. Our experimental measurements of liver stiffness via SWE in both healthy controls and 3-week fibrotic mice quantitatively confirmed this pattern (healthy: SWS 1.5954 ± 0.0581 m/s vs fibrotic: SWS 1.6077 ± 0.0566 m/s, $p = 0.62 >> 0.05$). As demonstrated in Figure 6-3c, SWE revealed no significant differences in tissue elasticity; however, histopathological analysis identified substantial collagen fiber deposition (Figure 6-3d-e). Enhancing early diagnostic sensitivity and preventing irreversible late-stage hepatic damage represent critical objectives in chronic liver disease management. This underscores an urgent need to develop noninvasive diagnostic adjuncts capable of detecting incipient fibrosis and enabling longitudinal monitoring of disease progression.

In summary, our experiments suggest that while SWE is effective in assessing moderate-to-advanced liver fibrosis, SWE-derived LSM showed limited sensitivity to microstructural changes in early fibrosis, consistent with clinical reports [213, 214]. These findings underscored the need for advanced modalities like PAEM to resolve subtle biomechanical alterations.

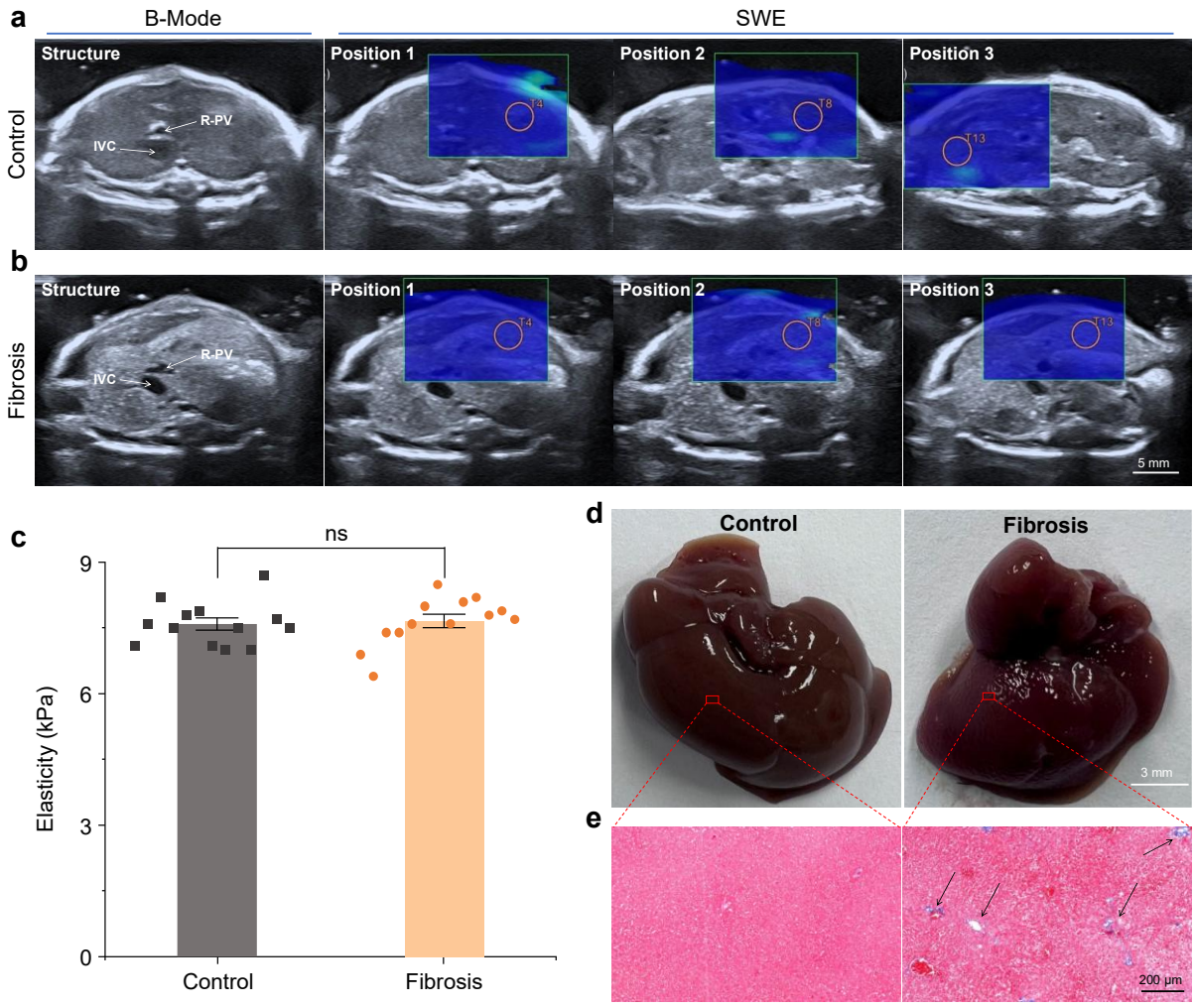

Figure 6-3. SWE imaging and histopathological validation of liver fibrosis. a-b) B-mode ultrasound and corresponding SWE elasticity maps of normal (a) and fibrotic (b) mouse livers. SWE color-coded stiffness maps overlay B-mode images, with ROIs marked as red circles. IVC: Inferior vena cava; R-PV: Right branch of portal vein. c) Quantitative LSM derived from SWE shows no significant differences between control and early-stage fibrotic groups. d-e) Photos and the corresponding Masson staining of healthy and fibrotic livers. As seen, fibrotic liver tissue exhibits collagen accumulation in portal areas (arrows), corroborating early structural remodeling despite undetectable SWE stiffness changes. Scale bars: 200 μm.

6.3.2 PAEM elasticity validation using PDMS films

To assess the capability of PAEM in measuring elasticity, validation experiments with AFM and PAEM measurements were conducted using PDMS thin films with varying

compositions. We employed PDMS materials spanning five distinct stiffness gradients. These were fabricated by varying the base-to-curing agent weight ratio (M1-M5 ratios: 4:1, 6:1, 10:1, 14:1, and 18:1, respectively) and cast into 300 µm-thick films for phantom experiments. Figure 6-4a presents the surface morphology of one PDMS thin film, showing a relatively smooth texture, which ensures uniformity in elasticity measurements. AFM force-displacement curves were obtained (Figure 6-4b), and the compressive Young's modulus was calculated based on the Hertz contact model, allowing for quantitative elasticity analysis. The correlation between measured Young's modulus and PDMS composition is depicted in Figure 6-4c, showing a decreasing trend in stiffness as the PDMS ratio increases. This trend aligns with known material properties, where a higher ratio results in a softer, less cross-linked elastomer [215].

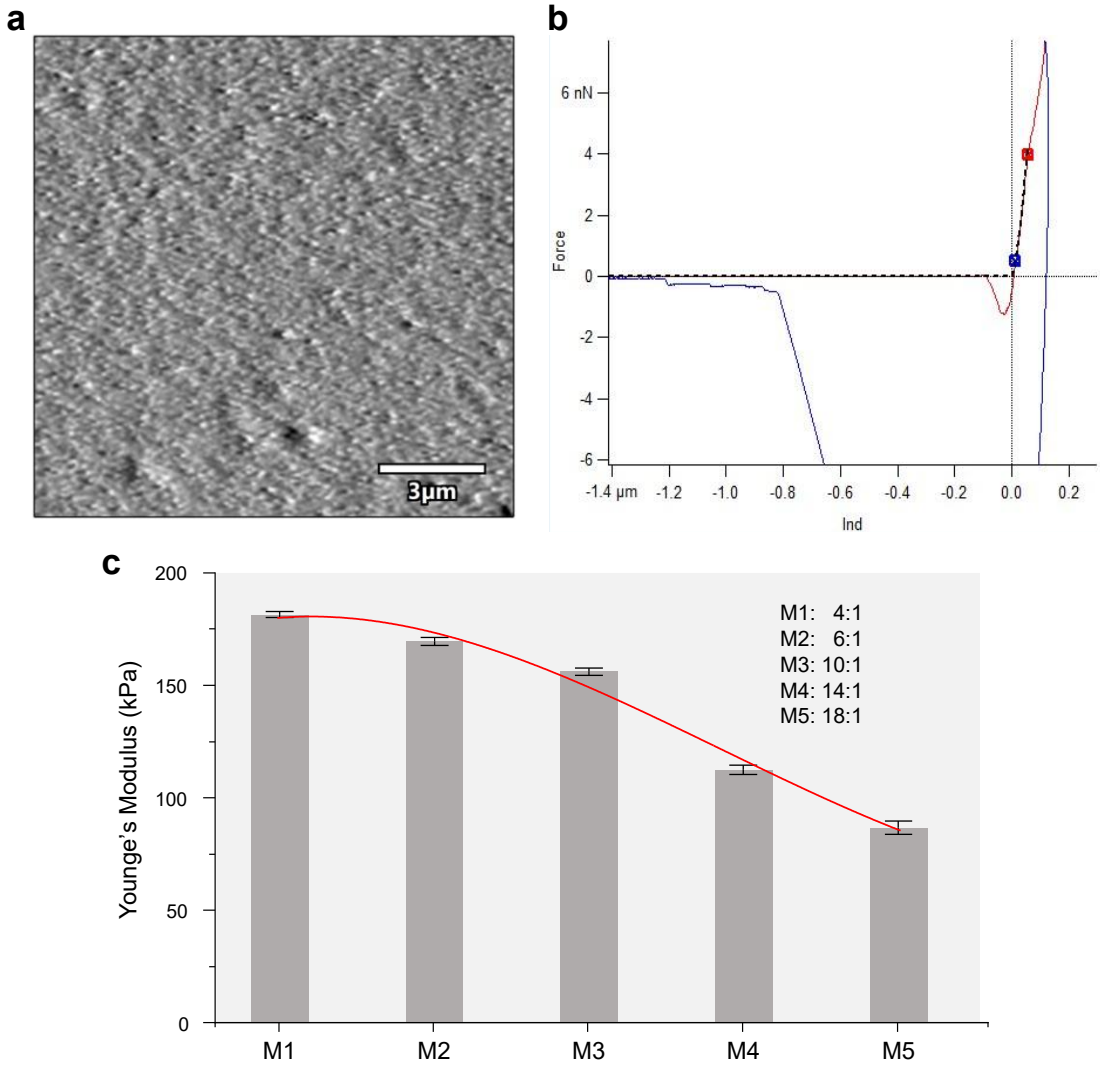

Figure 6-4. AFM elasticity assessment using PDMS phantoms with tunable stiffness. a) AFM surface morphology of a PDMS thin film, showing uniform topography. b)

Representative AFM force-displacement curve for PDMS elasticity quantification. Young's modulus was calculated using the Hertz contact model (dashed line: fitted curve). c) Young's modulus of PDMS films (M1-M5) decreases with increasing base-to-curing agent ratios.

Photoacoustic images of the PDMS thin films (Figure 6-5a) visualized the internal structural features. By extracting the depth profile (x-z plane) along the green line drawn on the PA image, we observe that the ToF at the film location is significantly greater than the ToF baseline in the background (green box in Figure 6-5a). This occurs because: the crosslinking reaction of PDMS affects its mechanical and acoustic properties, including the internal speed of sound within the material. The decrease in the crosslink density results in the decrease in the hypersonic sound velocity [216]. PDMS polymers or elastomers typically exhibit a natural sound speed of approximately 1000–1200 m/s, which is significantly lower than the 1500 m/s speed of sound in water. As a result, the measured ToF in PDMS is greater than that in the background (A-line direction in Figure 6-5a). Furthermore, as the PDMS ratio increases, the material becomes softer, leading to a slower sound propagation speed within the films.

The ToF elasticity maps were generated by identifying the temporal positions corresponding to the average maximum amplitude along the depth (z-direction) within the PA matrix, which were used to provide quantitative elasticity mapping. Within each film, three spatially non-overlapping regions of interest (ROIs) were randomly selected for ΔToF calculation, with three additional ROIs similarly chosen in the background region. As illustrated in Figure 6-5b, all ROIs were positioned in areas exhibiting relative homogeneity. Calculated as $\Delta ToF = \left| ToF_{background} - ToF_{PDMS} \right|$, ΔToF increased progressively from the stiffest (M1) to the softest (M5) PDMS samples (Figure 6-5c). As known, the ΔToF is inversely proportional to the ultrasound propagation speed in PDMS films; this implies that it is also inversely proportional to Young's modulus. This PA-ToF measurements trend shows strong agreement with the measured Young's modulus data by AFM, confirming the reliability of this method for elasticity assessment in biological tissues.

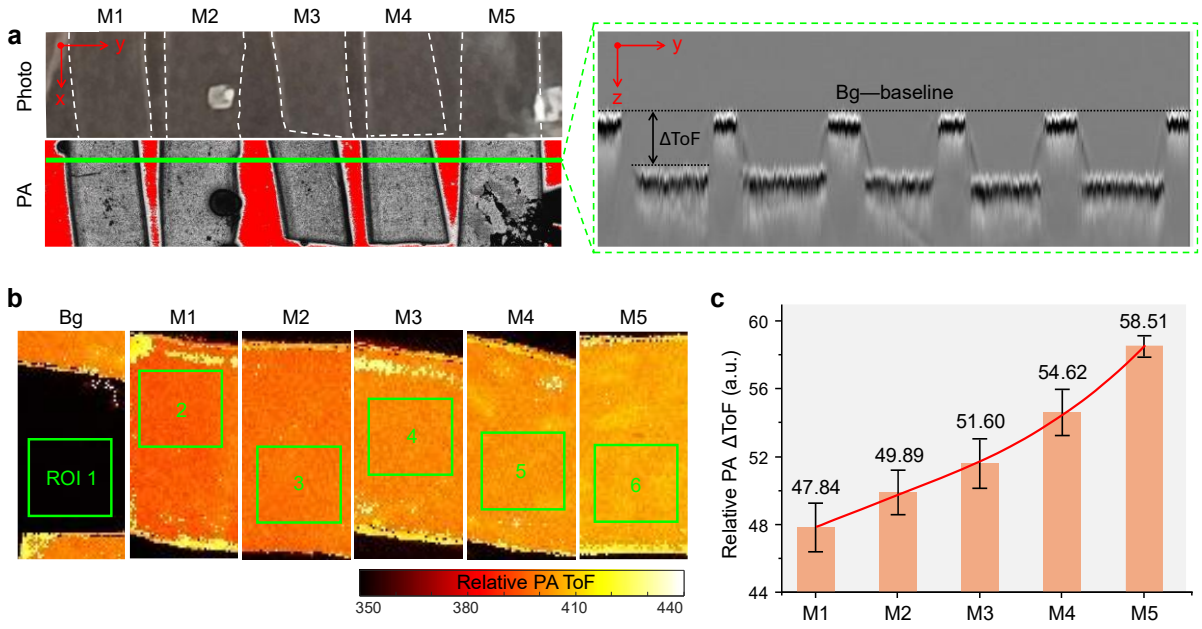

Figure 6-5. PAEM elasticity validation using PDMS phantoms with tunable stiffness. a) PA structural images of PDMS films (Bg: background). b) PAEM-derived ToF elasticity maps, color-coded to reflect stiffness variations. c) ΔToF increases with softer PDMS formulations, inversely correlating with Young's modulus. PAEM's ToF measurements align with AFM data, confirming its reliability for elasticity mapping in biological tissues.

6.3.3 ToF-based PA sensing of liver stiffness

We extracted the mean ToF peak values along the A-line direction from the 3D matrix of the PA signal, forming a new image matrix that represents the elasticity map. For each liver sample, ToF values were randomly selected from both the liver side and the background side. Specifically, three ToF values from the liver side and three from the background side were chosen, and the ΔToF was calculated as the difference between $ToF_{backgroud}$ and ToF_{liver}. Since the ultrasound longitudinal wave speed (LWS) within the liver tissue is proportional to liver components and stiffness (collagen deposition), and the speed is directly related to ΔToF, it is reasonable to assume that ΔToF correlates positively with liver stiffness. Thus, the changes in stiffness were reflected by the variation in ΔToF values. The sample size for each week was $n \geq 11$. One-way ANOVA showed that the data followed a normal distribution.

Assuming the ultrasound propagation speed in water to be 1500 m/s ($v_{background}$), we calculated that the LWS in normal liver tissue was approximately 1539 m/s, which is consistent with previously reported values for healthy liver tissue [217]. As seen (Figure 6-6),

early stages (weeks 1–2) showed modest ΔToF increases (0.012 ± 0.004 μs, ν_{liver} ~1596 m/s), which may be attributed to protective hepatic mechanisms and immune responses that counteract fibrosis development during this potentially reversible phase. Significant stiffness changes emerged at week 3 (ΔToF = 0.015 ± 0.003 μs and ν_{liver} = 1622 m/s, $p << 0.05$). The statistically equivalent SWE velocities (0.0123 m/s increase) align with known limitations in early fibrosis detection. Conversely, PAEM detected a significant 83 m/s increase (1539→1622 m/s) in 3-week fibrotic livers, demonstrating 7-fold greater velocity differential sensitivity than SWE (5.39% vs 0.77% change). Additionally, our methodology detected a significant ΔToF shift within the first week, corresponding to an LWS variation of 57 m/s (from 1539 to 1596 m/s) - representing a 3.7% velocity increase. This quantifiable early-stage alteration demonstrates the superior detection sensitivity of the PAEM approach, indicating significant advantages of our methods over conventional elastography. The ToF-based methodology offers dual capabilities: sensitive incipient fibrosis detection (Stage: 1-3 weeks) and quantitative LWS-based stiffness mapping across all fibrotic phases (Stage: 1-16 weeks)— LWS rising from 1,596 m/s (week 1) to 1,704 m/s (week 16), consistent with irreversible parenchymal stiffening for liver tissues [217].

As examined by receiver operating characteristic (ROC) curve, ToF measurements could differentiate between normal, early fibrosis, and advanced fibrosis stages with a high sensitivity and specificity (area under the curve: AUC > 0.95, Figure 6-6b). Compared to ROC analysis of structural features, ToF-based measurements demonstrate consistently high diagnostic sensitivity and specificity across all fibrotic stages. In contrast, structural analysis maintained elevated sensitivity only during earlier phases (Figure 6-6c). We therefore conclude that multiparametric integration—encompassing both microarchitectural and biomechanical properties—is essential for comprehensive fibrosis assessment.

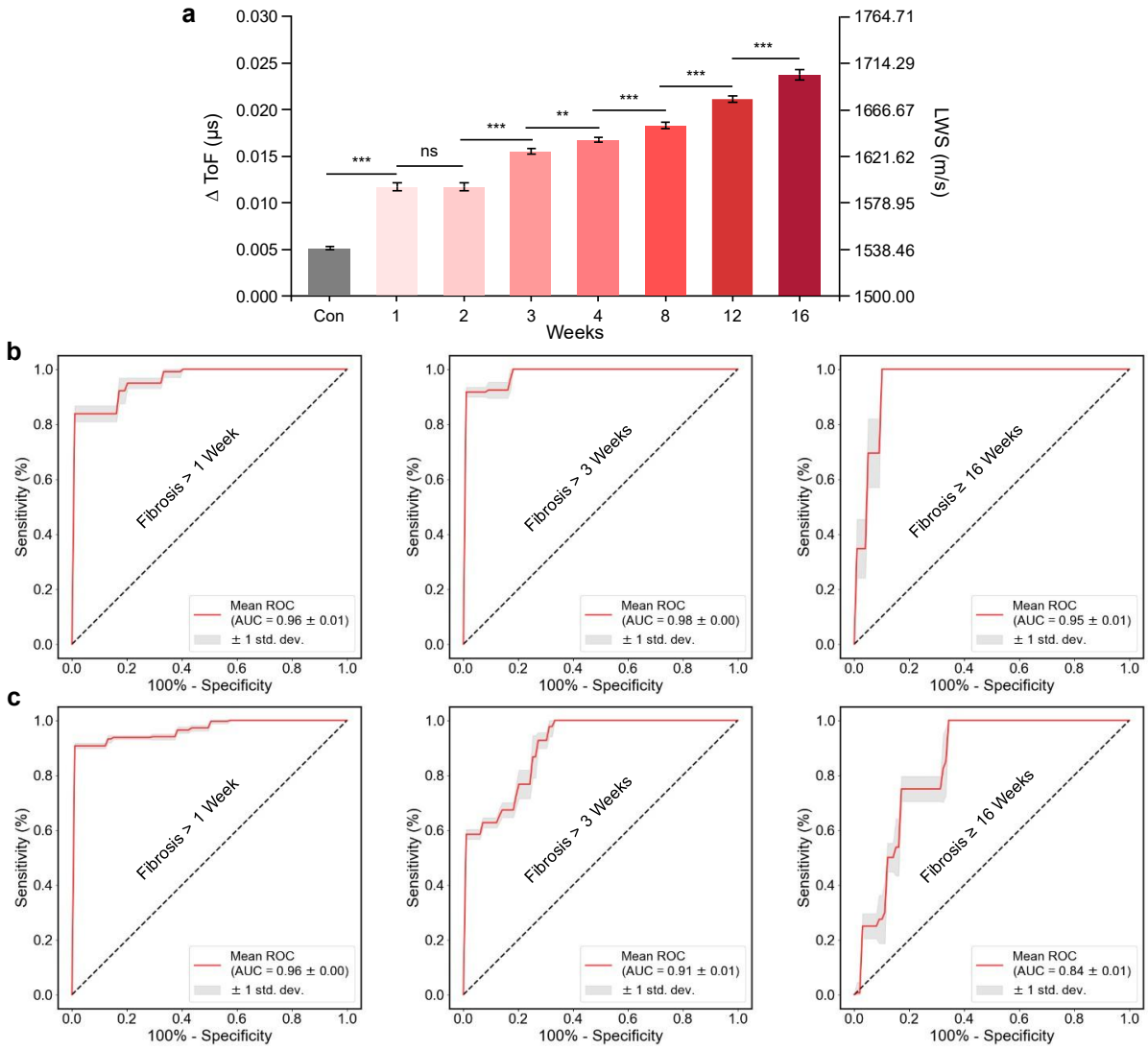

Figure 6-6. ToF-based PAEM elastic sensing tracks progressive liver stiffening during fibrosis. a) Longitudinal changes in ΔToF and ultrasound speed across fibrosis stages confirm distinct elasticity differences between different fibrosis stages. b) Elastic ToF measurements evaluate hepatic fibrosis staging through ROC curve analysis. c) Structural crevices-area calculations evaluate hepatic fibrosis staging through ROC curve analysis.

In summary, PAEM achieves early diagnosis and therapeutic monitoring through dual complementary pathways feature classification (Figure 6-7):

(1) Microstructural evaluation pathway (Up panel):

- Raw 3D PA data undergo reconstruction to visualize hepatic architecture
- Algorithm-driven extraction of fibrosis-induced crevices skeletons partitions the parenchyma into discrete sub-structures

- Quantitative analysis of two key morphological biomarkers: Crevices area (sub-threshold pixels) – reflecting collagen deposition; Lobules diameter (colored) – indicating parenchymal remodeling
- These structural parameters show diagnostic sensitivity primarily in early fibrosis stages (weeks 1-4)

(2) ToF-based stiffness pathway (Down panel):

- ToF data extracted from the 3D PA matrix are reconstructed into elasticity maps
- Paired measurements from liver ROIs and background ROIs yield ΔToF values
- Conversion to ultrasound propagation speed (ΔToF → vliver) provides direct quantification of tissue stiffness
- This biomechanical parameter exhibits progressive elevation from week 3 onward, correlating with irreversible fibrotic progression

Critically, the convergence of these orthogonal datasets – structural (spatial) and elastic (mechanical) – creates a diagnostic matrix where early-stage sensitivity (structural) and late-stage specificity (elastic) synergistically enhance detection accuracy. The superimposed regression curves in Figure 6-7 demonstrate how integrated parameter analysis resolves diagnostic ambiguities: Structural parameters plateau in advanced fibrosis while elasticity metrics maintain discriminative power, enabling comprehensive staging across the fibrotic continuum. So, multi-feature classification can increase diagnostic accuracy.

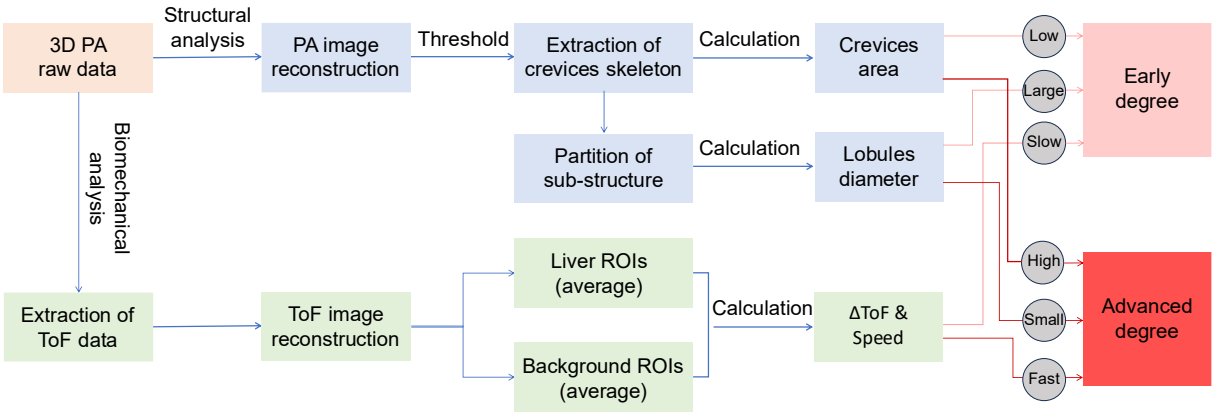

Figure 6-7. Combined application of PAEM in staging fibrosis. Early and advanced stages of liver fibrosis can be distinguished through multi-feature classification.

6.3.4 Tumor Margin delineation via PAEM

If liver fibrosis is not treated early, it can progress to severe hepatocarcinogenesis. The results above demonstrate that ToF-based PAEM is highly sensitive to early-stage liver fibrosis and has capability for monitoring fibrosis progression via sensing of multi-parametric structural and elastic information. This method may further offer benefits of distinguishing hepatocellular carcinoma (HCC) from adjacent normal tissue. Structural imaging highlighted irregular tumor boundaries (Figure 6-8a), while elasticity maps revealed a stiffness gradient increasing toward the tumor core (Figure 6-8b). These findings aligned with histopathology (Figure 6-8c), demonstrating PAEM's dual capability in resolving both morphological and biomechanical hallmarks of malignancy. Such high-resolution and high-sensitivity elasticity sensing underscores its potential for precise tumor margin identification and stiffness-guided diagnosis of hepatic malignancies.

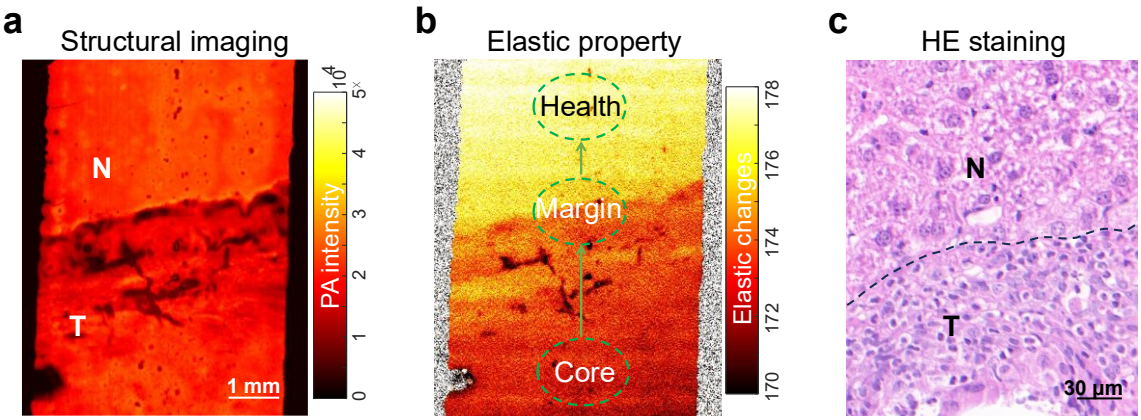

Figure 6-8. PAEM delineates tumor boundaries through combined structural and elastic imaging. a) PA structural image of a liver section containing adjacent tumor (T) and normal (N) tissues, revealing irregular tumor margins. b) PAEM elasticity map demonstrates a progressive stiffness gradient, with elevated rigidity in the tumor core (red-orange) compared to surrounding normal parenchyma (yellow-white). c) Corresponding H&E staining validates the histopathological boundary (dashed line) between tumor and normal regions.

6.4 Summary

Early diagnosis of liver fibrosis is crucial for halting disease progression and improving patient outcomes. However, conventional techniques such as biopsy and USE face limitations

in sensitivity, resolution, and practicality for longitudinal monitoring. To address these challenges, we developed PAEM, a multi-parametric imaging platform that synergizes high-resolution structural visualization with ToF-based biomechanical sensing. PAEM demonstrated exceptional sensitivity to early fibrotic changes in a CCl4-induced mouse model, detecting microstructural remodeling (e.g., pseudo-lobule formation, crevice expansion) and incremental stiffness increases (ΔToF = 0.015 ± 0.003 μs at Week 3, $v_{liver} \approx$ 1622 m/s) that conventional SWE failed to resolve. By integrating high-resolution, high-sensitivity elasticity mapping with histopathological and serum biomarker analyses, PAEM achieved comprehensive fibrosis staging, bridging the gap between microscopic tissue alterations and macroscopic clinical metrics.

Notably, PAEM's ability to delineate tumor margins via stiffness gradients underscores its versatility beyond fibrosis, offering potential applications in oncology for boundary definition and treatment planning. Two essential prerequisites must be emphasized for the proposed PAEM methodology: First, sample thickness must be precisely known and spatially uniform, as it serves as a fundamental parameter for LWS calculations. Second, during PAEM detection, non-compressive contact must be maintained to prevent external force-induced deformation, since both mechanical stress and thickness variations constitute significant confounding variables in LWS computation. Future work will focus on enhancing PAEM's imaging depth [218] and real-time processing capabilities to enable *in vivo* clinical translation. For example, the capacity for precise tumor core-to-margin demarcation holds significant promise for intraoperative guidance—particularly in defining resection boundaries during cancer surgery. Additionally, extending its utility to other fibrotic diseases (e.g., pulmonary, renal) and incorporating artificial intelligence-driven image analysis [219, 220] could further automate diagnostics and refine staging accuracy. In summary, PAEM represents a transformative advancement in elasticity-driven diagnostics, combining the resolution of PAM with the functional insights of elastography. Its capacity for high-resolution, high-sensitivity, multi-parametric tissue evaluation positions PAEM as a powerful tool for precision medicine, with broad applicability in early disease detection, therapeutic monitoring, and mechanistic studies of fibrosis and malignancy.

It also has some limitations. Primarily, an increase in tissue stiffness (elastic modulus) significantly enhances ultrasound propagation speed, while an increase in tissue density tends to reduce it. This relationship is well-defined mathematically, commonly expressed as $v = \sqrt{E/\rho}$, where E represents the elastic modulus (positively correlated with sound velocity)

and ρ denotes density (inversely correlated with sound velocity). In most soft tissues, changes in stiffness exert a far greater influence on sound velocity than changes in density. For example, during hepatic fibrosis progression, the stiffness of the liver increases substantially—often by several-fold—whereas the density may only slightly increase due to collagen deposition. According to the formula, the pronounced increase in the numerator (E) combined with a marginal rise in the denominator (ρ) results in a net significant increase in sound velocity (v). This physical principle underpins ultrasound velocity-based elastography techniques for detecting fibrosis. Thus, in this study, the relatively minor influence of density on sound velocity was neglected, and the velocity calculated based on ToF was used as a proxy for changes in tissue stiffness. Future work may incorporate multi-parametric influences of soft tissues to compute accurate elastic moduli, similar to those provided by SWE.

Chapter 7 Conclusion and Future Directions

7.1 Summary of research achievements

Advancing brain science is critical not only for deciphering human cognition and addressing neurological disorders but also for driving innovations in artificial intelligence and neuromorphic computing. Concurrently, chronic liver diseases remain a global health burden, where early detection and intervention are pivotal for disease reversal. This study establishes PAI as a foundational platform to achieve two pivotal objectives: (1) longitudinal monitoring and spatiotemporally resolved mapping of epileptiform electrophysiological signals in deep murine brain structures, and (2) quantitative biomechanical characterization of hepatic lobular architecture and tissue elasticity during fibrotic progression in murine models. Our findings demonstrate PAI's dual capabilities as a diagnostic and surveillance tool, particularly in neurological pathologies and stiffness-associated organ diseases, exemplified by its potential in tracking hepatic fibrosis evolution toward hepatocellular carcinoma. This work bridges functional neuroimaging with viscoelastic tissue profiling, proposing a multimodal paradigm for precision medicine.

In photoacoustic brain function mapping, we present the first trial employing a high spatiotemporal-resolution WF-PABD for prolonged monitoring and tracking of the VSD response, which directly reflects brain activity in vivo. Specifically, a generalized VSD indicator DiSC3(5) was employed. Through cellular experiments, we discovered that it exhibits good fluorescence and photoacoustic dual responsiveness, with the two responses being opposite in relation to changes in membrane potential, following the principle of energy conservation. We then summarized the optical response mechanism of the probe. Subsequently, we validated this mechanism using fluorescence imaging in epileptic mice. However, due to the slow speed and low resolution of fluorescence imaging, we improved the method by proposing the use of high-resolution PAI combined with DiSC3(5) to achieve long-term, non-invasive detection of whole-brain electrical signals in mice (PA-VSD). We conducted PA imaging under a single wavelength excitation of 670 nm, which is under a noticeably reduced blood absorption background and making the DiSC3(5) signal changes more representative of brain voltage variations. The designed platform can provide an

effective FOV of about 5.5 cm in diameter, which is adequate to image the entire mouse brain and potentially a portion of human brain [180]. Then this platform yields an ultrahigh acquisition speed of 10 μs/frame, which can overcome the motional artifacts and hence allows for monitoring under free motion status. By employing PA-VSD, we can pinpoint the epileptic foci and determine regions with more active epilepsy activity, potentially providing guidance for surgical navigation and treatment. Interestingly, by combining high-temporal-resolution visualization and investigating brain region correlations, we obtained results on electrical conduction pathways and directions in certain regions, which can contribute to the study of nerve function and electrical conduction. Overall, we believe that the proposed PA-VSD framework can provide high-spatiotemporal-resolution visualization, accurate lesion localization, and valuable insights into brain function communication through whole-brain neuronal voltage activities, with far-reaching implications for in-vivo neurophysiological investigations.

In photoacoustic hepatic disease diagnosis and monitoring, we proposed a novel method for simultaneously screening liver vascular or lobule microstructure and measurement of biomechanical property. Specifically, hepatic fibrosis murine models spanning early to advanced stages were established for multiparametric longitudinal monitoring. CCl_4-induced liver fibrosis primarily causes cellular injury and necrosis in the central venous region of the hepatic lobules, eventually leading to the formation of myofibroblast-like cells [131]. Persistent inflammatory attacks can exacerbate microscopic cellular lesions, leading to structural and biomechanical changes. Structurally, vascular and lobular deformation preceded biomechanical alterations during fibrogenesis. In early-stage fibrosis, we observed progressive destruction of hepatic lobules starting from week 1, accompanied by the formation of pseudo-lobules with reduced diameters via high-resolution OR-PAM. At the microarchitectural level, PAM effectively differentiated fibrosis progression during weeks 1-3. However, pseudo-lobular diameter variations lost discriminative power in advanced fibrosis staging. We therefore developed ToF-based PAEM to quantify hepatic stiffness across fibrosis grades. Since hepatic stiffness positively correlates with acoustic wave propagation velocity, we utilized ToF of PA signals through liver sections as a quantitative stiffness indicator. Longitudinal ToF-PAEM measurements revealed progressive acoustic velocity elevation in hepatic fibrosis progression: healthy liver (1539 ± 12 m/s), week 1 (1596 ± 18 m/s), week 3 (1621 ± 15 m/s), and week 16 (1704 ± 22 m/s), demonstrating significant correlations with histopathological changes and superior early diagnostic

sensitivity versus SWE. The integrated analysis of pseudo-lobular microstructural changes and ToF-based stiffness quantification established a multiparametric framework that achieved high sensitivity for early fibrosis detection and tumor margin delineation, yielding clinically translatable biomarkers.

7.2 Limitations and prospects for clinical translation

In the realm of fundamental research, molecular imaging technologies have established an irreplaceable role in biomedical sciences. Looking toward clinical applications, significant progress has already been achieved. For the central nervous system, although various imaging modalities enable non-invasive brain detection, direct visualization of intracranial structural and functional information remains elusive. Additionally, accurately characterizing the mechanical properties of soft tissues continues to present challenges in sensitivity and precision, underscoring the critical need for advanced imaging technologies.

Photoacoustic imaging, the core methodology of this study, represents a novel hybrid modality that synergizes the high contrast of conventional optical imaging with the penetration depth of ultrasound, thereby overcoming the ballistic photon transport limitations inherent to traditional high-resolution optical techniques. While limited tissue penetration has historically constrained the clinical application of optical imaging, recent advancements in laser technology have accelerated its translational development. PACT can provide high-resolution structural and functional imaging of whole small animals, with a penetration depth of up to 4.8 cm [48]. In human tissues, PACT can clearly display blood vessels with a diameter of 258 μm with 4 cm beneath the skin surface in the human breast [221]. Transrectal ultrasound/photoacoustic dual-modality imaging of the prostate can reveal the blood vessels surrounding the human prostate, and after intravenous injection of ICG, the photoacoustic signal intensity of prostate cancer is significantly enhanced [149]. PACT can also be used for imaging human limbs, clearly displaying blood vessels and SO_2 [222]. Additionally, the Imagio® photoacoustic imaging system produced by Seno Medical has been CE certified in the European Union since April 2014 as an adjunct to mammography and is currently undergoing post-market surveillance and clinical follow-up studies in Europe. In China, PAM has been used for microvascular imaging of superficial dermal lesions in port-wine stains and has been approved by the Guangdong Provincial Medical Products Administration (approval number: 20202060111). This demonstrates that photoacoustic imaging technology has gained

the favor of many clinical practitioners and is actively being researched for clinical translation applications in various fields both domestically and internationally. It is believed that with the progress of optical technology, this technology will provide greater assistance in the diagnosis and treatment of clinical medicine.

7.3 Future research opportunities

Future work will focus on:

(1) System miniaturization: We will integrate fiber-laser ultrasound sensors to enhance portability, aiming for miniaturization and portability. Further performance optimization will be pursued, enhancing the sensitivity through acoustic lens integration and related methods, thereby achieving a higher signal-to-noise ratio.

(2) Deep-brain imaging: We intend to optimize and enhance the imaging system through multimode fiber-based laser transmission and wavefront shaping modulation techniques. This will enable minimally invasive insertion for deep brain structure and blood oxygenation imaging, aiming to simultaneously acquire multiple hemodynamic parameters.

(3) Multimodal integration: The above system will be integrated with fluorescence-based dual-modality approaches, enabling simultaneous monitoring of calcium ion electrical signals and optogenetic stimulation. This integration offers significant potential for diagnostic and therapeutic applications targeting deep and fixed brain regions. To achieve these goals, we will focus on core components, leveraging highly sensitive fiber-optic sensors in conjunction with high-energy, high-repetition-rate, multi-wavelength lasers and wavefront shaping technologies, thus enabling simultaneous multi-parametric acquisition without compromising imaging speed.

(4) AI-driven liver diagnosis: For the diagnostic framework of liver fibrosis proposed herein, based on structural and mechanical changes, artificial intelligence (AI)-driven image training will be incorporated to facilitate automatic and precise machine identification of fibrosis.

(5) Wearable devices: We will merge ultrasound, PAI, and photoplethysmography (PPG) in wearable microelectronics for real-time monitoring of subcutaneous structures, oxygenation, blood pressure, vascular elasticity, and other physiological parameters.

References:

1. Cierniak, R., *X-ray computed tomography in biomedical engineering*. 2011: Springer Science & Business Media.
2. Georgiadis, M., et al., *Nanostructure-specific X-ray tomography reveals myelin levels, integrity and axon orientations in mouse and human nervous tissue.* Nature Communications, 2021. **12**(1): p. 2941.
3. Samad A, R., et al., *Imaging and Surveillance of Chronic Aortic Dissection: Current Practice and Future Directions.* Heart Lung and Circulation, 2025(0).
4. Fullerton, G.D., *Basic concepts for nuclear magnetic resonance imaging.* Magnetic Resonance Imaging, 1982. **1**(1): p. 39-53.
5. Morris, P.G., *Nuclear magnetic resonance imaging in medicine and biology.* 1986.
6. Weiskopf, N., et al., *Quantitative magnetic resonance imaging of brain anatomy and in vivo histology.* Nature Reviews Physics, 2021. **3**(8): p. 570-588.
7. Hao, W., et al., *Three-Dimensional Vector MR Elastography for Evaluating Tissue Mechanical Heterogeneity to Assess Liver Disease Progression.* Radiology, 2025. **315**(1).
8. Tehrani, N., et al., *Localization of interictal discharge origin: A simultaneous intracranial electroencephalographic–functional magnetic resonance imaging study.* Epilepsia, 2021. **62**(5): p. 1105-1118.
9. Arnold, T.C., et al., *Low-field MRI: clinical promise and challenges.* Journal of Magnetic Resonance Imaging, 2023. **57**(1): p. 25-44.
10. Fletcher, J.W., et al., *Recommendations on the use of 18F-FDG PET in oncology.* Journal of Nuclear Medicine, 2008. **49**(3): p. 480-508.
11. Savic, I., M. Ingvar, and S. Stone-Elander, *Comparison of [11C] flumazenil and [18F] FDG as PET markers of epileptic foci.* Journal of Neurology, Neurosurgery & Psychiatry, 1993. **56**(6): p. 615-621.
12. Chételat, G., et al., *Amyloid-PET and 18F-FDG-PET in the diagnostic investigation of Alzheimer's disease and other dementias.* The Lancet Neurology, 2020. **19**(11): p. 951-962.
13. Rosenbaum, S.J., et al., *False-positive FDG PET uptake− the role of PET/CT.* European Radiology, 2006. **16**: p. 1054-1065.
14. Landhuis, E., *Ultrasound for the brain.* Nature, 2017. **551**(7679): p. 257-259.
15. Cox, B. and P. Beard, *Super-resolution ultrasound.* Nature, 2015. **527**(7579): p. 451-452.
16. Thomas, D., et al., *Investigating liver stiffness and viscosity for fibrosis, steatosis and activity staging using shear wave elastography.* Journal Of Hepatology, 2014. **62**(2).
17. Xiao-Qing, Z., et al., *US Shear-Wave Elastography Dispersion for Characterization of Chronic Liver Disease.* Radiology, 2022. **305**(3).

18. Divya, T., et al., *Advances in Optical Contrast Agents for Medical Imaging: Fluorescent Probes and Molecular Imaging.* Journal of Imaging, 2025. **11**(3).

19. Minh H, T. and F. Baowei, *Compact and ultracompact spectral imagers: technology and applications in biomedical imaging.* Journal of Biomedical Optics, 2023. **28**(4).

20. Cheng, M., Y. Mo, and G. Zheng, *Nano versus Molecular: Optical Imaging Approaches to Detect and Monitor Tumor Hypoxia.* Advanced Healthcare Materials, 2021. **10**(2): p. e2001549.

21. Soumik Saha, P., J. Yan, and C. Zhu, *in vivoPortable multi-parametric microscopy for noninvasive metabolic and vascular imaging of orthotopic tongue cancer models.* Journal of Biomedical Optics, 2025. **30**: p. S23905.

22. Qiu, Y., et al., *Collagen fibers quantification for liver fibrosis assessment using linear dichroism photoacoustic microscopy.* Photoacoustics, 2025. **42**: p. 100694.

23. Léo, P., et al., *Measuring choriocapillaris blood flow with laser Doppler optical coherence tomography.* Optics Letters, 2025. **50**(8).

24. Shoujun, Z., et al., *Near-Infrared-II Molecular Dyes for Cancer Imaging and Surgery.* Advanced Materials, 2019. **31**(24).

25. S, B. and G. S S, *Optical imaging of Renilla luciferase reporter gene expression in living mice.* Proceedings of the National Academy of Sciences of the United States of America, 2001. **99**(1).

26. Jacob T, F., et al., *Dual-comb photoacoustic spectroscopy.* Nature Communications, 2020. **11**(1).

27. Donald T, M. and K. Kazuhiro, *Cellular-Scale Imaging of Transparent Retinal Structures and Processes Using Adaptive Optics Optical Coherence Tomography.* Annual Review Of Vision Science, 2020. **6**(0).

28. Lingmei, C., et al., *Deep structural brain imaging via computational three-photon microscopy.* Journal of Biomedical Optics, 2025. **30**(4).

29. Harold L, D., *Optical Coherence Tomography - Light and Truth.* The New England Journal of Medicine, 2023. **389**(16).

30. Li, L., et al., *Single-breath-hold photoacoustic computed tomography of the breast.* Nature Communications, 2018. **9**(1).

31. Pang, W., et al., *Direct Monitoring of Whole-Brain Electrodynamics via High-Spatiotemporal-Resolution Photoacoustics with Voltage-Sensitive Dye.* Laser & Photonics Reviews, 2024. **18**(10): p. 2400165.

32. Bell, A.G., *On the production and reproduction of sound by light.* American journal of science, 1880. **3**(118): p. 305-324.

33. Kruger, R.A., *Photoacoustic ultrasound.* Medical physics, 1994. **21**(1): p. 127-131.

34. Wang, L.V., et al., *Microwave-induced acoustic imaging of biological tissues.* Review of scientific instruments, 1999. **70**(9): p. 3744-3748.

35. Hordvik, A., *Measurement techniques for small absorption coefficients: recent advances.* Applied optics, 1977. **16**(11): p. 2827-2833.

36. Maugh, T.H., *Photoacoustic spectroscopy: New uses for an old technique.* Science, 1975. **188**(4183): p. 38-39.

37. Wang, X., et al., *Noninvasive laser-induced photoacoustic tomography for structural and functional in vivo imaging of the brain.* Nature Biotechnology, 2003. **21**(7): p. 803-806.

38. Xu, Y., et al., *Reconstructions in limited-view thermoacoustic tomography.* Medical physics, 2004. **31**(4): p. 724-733.

39. Xu, M. and L.V. Wang, *Photoacoustic imaging in biomedicine.* Review of scientific instruments, 2006. **77**(4): p. 041101.

40. Xu, M. and L.V. Wang, *Universal back-projection algorithm for photoacoustic computed tomography.* Physical Review E, 2005. **71**(1): p. 016706.

41. Zhang, H.F., et al., *Functional photoacoustic microscopy for high-resolution and noninvasive in vivo imaging.* Nature biotechnology, 2006. **24**(7): p. 848-851.

42. Song, L., et al., *Fast 3-D dark-field reflection-mode photoacoustic microscopy in vivo with a 30-MHz ultrasound linear array.* Journal of biomedical optics, 2008. **13**(5): p. 054028-054028-5.

43. Buehler, A., et al., *Video rate optoacoustic tomography of mouse kidney perfusion.* Optics letters, 2010. **35**(14): p. 2475-2477.

44. Razansky, D., A. Buehler, and V. Ntziachristos, *Volumetric real-time multispectral optoacoustic tomography of biomarkers.* Nature protocols, 2011. **6**(8): p. 1121-1129.

45. Kruger, R.A., et al., *Photoacoustic angiography of the breast.* Medical physics, 2010. **37**(11): p. 6096-6100.

46. Gamelin, J., et al., *A real-time photoacoustic tomography system for small animals.* Optics express, 2009. **17**(13): p. 10489-10498.

47. Xia, J., et al., *Whole-body ring-shaped confocal photoacoustic computed tomography of small animals in vivo.* Journal of biomedical optics, 2012. **17**(5): p. 050506-050506.

48. Li, L., et al., *Single-impulse panoramic photoacoustic computed tomography of small-animal whole-body dynamics at high spatiotemporal resolution.* Nature Biomedical Engineering, 2017. **1**(5): p. 0071.

49. Yang, J., et al., *Multiplane Spectroscopic Whole-Body Photoacoustic Computed Tomography of Small Animals In Vivo.* Laser & Photonics Reviews, 2025. **19**(3): p. 2400672.

50. Li, L., J. Yao, and L.V. Wang, *Photoacoustic tomography of neural systems.* Neural Engineering, 2020: p. 349-378.

51. Wang, L.V. and H.-i. Wu, *Biomedical optics: principles and imaging*. 2012: John Wiley & Sons.

52. Maslov, K., et al., *Optical-resolution photoacoustic microscopy for in vivo imaging of single capillaries.* Optics letters, 2008. **33**(9): p. 929-931.

53. Hu, S., K. Maslov, and L.V. Wang, *Second-generation optical-resolution photoacoustic microscopy with improved sensitivity and speed.* Optics letters, 2011. **36**(7): p. 1134-1136.

54. Wang, L., et al., *Fast voice-coil scanning optical-resolution photoacoustic microscopy.* Optics letters, 2011. **36**(2): p. 139-141.

55. Yao, J., et al., *Wide-field fast-scanning photoacoustic microscopy based on a water-immersible MEMS scanning mirror.* Journal of biomedical optics, 2012. **17**(8): p. 080505-080505.

56. Zhang, C., et al., *Reflection-mode submicron-resolution in vivo photoacoustic microscopy.* Journal of biomedical optics, 2012. **17**(2): p. 020501-020501.

57. Zhang, C., K. Maslov, and L.V. Wang, *Subwavelength-resolution label-free photoacoustic microscopy of optical absorption in vivo.* Optics letters, 2010. **35**(19): p. 3195-3197.

58. Yuan, Y., S. Yang, and D. Xing, *Optical-resolution photoacoustic microscopy based on two-dimensional scanning galvanometer.* Applied Physics Letters, 2012. **100**(2): p. 023702.

59. Wang, L.V. and L. Gao, *Photoacoustic microscopy and computed tomography: from bench to bedside.* Annual Review of Biomedical Engineering, 2014. **16**(1): p. 155-185.

60. Zhong, X., et al., *Free-moving-state microscopic imaging of cerebral oxygenation and hemodynamics with a photoacoustic fiberscope.* Light: Science & Applications, 2024. **13**(1): p. 5.

61. Lee, J., et al., *Fully waterproof two-axis galvanometer scanner for enhanced wide-field optical-resolution photoacoustic microscopy.* Optics Letters, 2020. **45**(4): p. 865-868.

62. Liu, Y., C. Zhang, and L.V. Wang, *Effects of light scattering on optical-resolution photoacoustic microscopy.* Journal of Biomedical Optics, 2012. **17**(12): p. 126014-126014.

63. Moothanchery, M., et al., *Acoustic resolution photoacoustic microscopy based on microelectromechanical systems scanner.* Journal of Biophotonics, 2020. **13**(2): p. e201960127.

64. Wang, L., et al., *Video-rate functional photoacoustic microscopy at depths.* Journal of biomedical optics, 2012. **17**(10): p. 106007-106007.

65. Song, K.H. and L.V. Wang, *Deep reflection-mode photoacoustic imaging of biological tissue.* Journal of biomedical optics, 2007. **12**(6): p. 060503-060503-3.

66. Kim, J., et al., *Enhanced dual-mode imaging: Superior photoacoustic and ultrasound endoscopy in live pigs using a transparent ultrasound transducer.* Science Advances, 2024. **10**(47): p. eadq9960.

67. Liang, Y., et al., *Optical-resolution functional gastrointestinal photoacoustic endoscopy based on optical heterodyne detection of ultrasound.* Nature Communications, 2022. **13**(1): p. 7604.

68. Kim, K., et al., *Tapered catheter-based transurethral photoacoustic and ultrasonic endoscopy of the urinary system.* Optics Express, 2022. **30**(15): p. 26169-26181.

69. Xia, Q., et al., *Non-invasive evaluation of endometrial microvessels via in vivo intrauterine photoacoustic endoscopy.* Photoacoustics, 2024. **36**: p. 100589.

70. Basij, M., et al. *Development of an integrated photoacoustic-guided laser ablation intracardiac theranostic system*. in *2021 IEEE International Ultrasonics Symposium (IUS)*. 2021. IEEE.

71. Mathuria, N., et al., *In vivo assessment of cardiac radiofrequency ablation in a large-animal model using photoacoustic-ultrasound imaging.* JACC: Clinical Electrophysiology, 2025.

72. Wu, H., et al., *Miniaturized stacked transducer for intravascular sonothrombolysis with internal-illumination photoacoustic imaging guidance and clot characterization.* IEEE Transactions on Biomedical Engineering, 2023. **70**(8): p. 2279-2288.

73. Wen, X., et al., *High-robustness intravascular photoacoustic endoscope with a hermetically sealed opto-sono capsule.* Optics Express, 2020. **28**(13): p. 19255-19269.

74. Yao, D.-K., et al., *In vivo label-free photoacoustic microscopy of cell nuclei by excitation of DNA and RNA.* Optics letters, 2010. **35**(24): p. 4139-4141.

75. Yao, D.-K., et al., *Optimal ultraviolet wavelength for in vivo photoacoustic imaging of cell nuclei.* Journal of biomedical optics, 2012. **17**(5): p. 056004-056004.

76. Zhang, C., et al., *Label-free photoacoustic microscopy of myocardial sheet architecture.* Journal of biomedical optics, 2012. **17**(6): p. 060506-060506.

77. Zhang, C., et al., *Label-free photoacoustic microscopy of cytochromes.* Journal of biomedical optics, 2013. **18**(2): p. 020504-020504.

78. Yao, J., et al., *Label-free oxygen-metabolic photoacoustic microscopy in vivo.* Journal of biomedical optics, 2011. **16**(7): p. 076003-076003-11.

79. Staley, J., et al., *Growth of melanoma brain tumors monitored by photoacoustic microscopy.* Journal of biomedical optics, 2010. **15**(4): p. 040510-040510-3.

80. Zink, D., A.H. Fischer, and J.A. Nickerson, *Nuclear structure in cancer cells.* Nature reviews cancer, 2004. **4**(9): p. 677-687.

81. Sinha, R.P. and D.-P. Häder, *UV-induced DNA damage and repair: a review.* Photochemical & Photobiological Sciences, 2002. **1**(4): p. 225-236.

82. Hu, S., et al. *Multi-contrast photoacoustic microscopy*. in *Photons Plus Ultrasound: Imaging and Sensing 2012*. 2012. SPIE.

83. Krumholz, A., et al., *Functional photoacoustic microscopy of diabetic vasculature.* Journal of biomedical optics, 2012. **17**(6): p. 060502-060502.

84. Society, A.C., *Cancer facts & figures*. 2008: The Society.

85. Galanzha, E.I., et al., *In vivo, noninvasive, label-free detection and eradication of circulating metastatic melanoma cells using two-color photoacoustic flow cytometry with a diode laser.* Cancer research, 2009. **69**(20): p. 7926-7934.

86. Weight, R.M., et al., *Photoacoustic detection of metastatic melanoma cells in the human circulatory system.* Optics letters, 2006. **31**(20): p. 2998-3000.

87. Galanzha, E.I., et al., *In vivo magnetic enrichment and multiplex photoacoustic detection of circulating tumour cells.* Nature nanotechnology, 2009. **4**(12): p. 855-860.

88. Wang, Y., et al., *Fiber-laser-based photoacoustic microscopy and melanoma cell detection.* Journal of biomedical optics, 2011. **16**(1): p. 011014-011014-4.

89. Zhang, Y., et al., *Chronic label-free volumetric photoacoustic microscopy of melanoma cells in three-dimensional porous scaffolds.* Biomaterials, 2010. **31**(33): p. 8651-8658.

90. Jiao, S., et al., *Photoacoustic ophthalmoscopy for in vivo retinal imaging.* Optics express, 2010. **18**(4): p. 3967-3972.

91. Song, W., et al., *Integrating photoacoustic ophthalmoscopy with scanning laser ophthalmoscopy, optical coherence tomography, and fluorescein angiography for a multimodal retinal imaging platform.* Journal of biomedical optics, 2012. **17**(6): p. 061206-061206.

92. Wang, H.-W., et al., *Label-free bond-selective imaging by listening to vibrationally excited molecules.* Physical review letters, 2011. **106**(23): p. 238106.

93. Yakovlev, V.V., et al., *Stimulated Raman photoacoustic imaging.* Proceedings of the National Academy of Sciences, 2010. **107**(47): p. 20335-20339.

94. Xu, Z., C. Li, and L.V. Wang, *Photoacoustic tomography of water in phantoms and tissue.* Journal of biomedical optics, 2010. **15**(3): p. 036019-036019-6.

95. Shen, Y., et al., *Measurement of the optical absorption coefficient of a liquid by use of a time-resolved photoacoustic technique.* Applied Optics, 2000. **39**(22): p. 4007-4012.

96. Wang, B., et al., *Intravascular photoacoustic imaging.* IEEE Journal of selected topics in Quantum Electronics, 2010. **16**(3): p. 588-599.

97. Yao, J. and L.V. Wang, *Photoacoustic microscopy.* Laser & photonics reviews, 2013. **7**(5): p. 758-778.

98. Wood, C.A., et al., *Clinically translatable quantitative molecular photoacoustic imaging with liposome-encapsulated ICG J-aggregates.* Nature communications, 2021. **12**(1): p. 5410.

99. Kim, C., et al., *Deeply penetrating in vivo photoacoustic imaging using a clinical ultrasound array system.* Biomedical optics express, 2010. **1**(1): p. 278-284.

100. Pang, W., et al., *Direct Monitoring of Whole-Brain Electrodynamics via High-Spatiotemporal-Resolution Photoacoustics with Voltage-Sensitive Dye.* Laser & Photonics Reviews, 2024. **18**(10): p. 2400165.

101. Chen, Q., et al., *A self-assembled albumin-based nanoprobe for in vivo ratiometric photoacoustic pH imaging.* Advanced Materials, 2015. **27**(43): p. 6820-6827.

102. Ma, J., et al., *Zinc phthalocyanine-soybean phospholipid complex based drug carrier for switchable photoacoustic/fluorescence image, multiphase photothermal/photodynamic treatment and synergetic therapy.* Journal of Controlled Release, 2018. **284**: p. 1-14.

103. Tsang, V.T., X. Li, and T.T. Wong, *A review of endogenous and exogenous contrast agents used in photoacoustic tomography with different sensing configurations.* Sensors, 2020. **20**(19): p. 5595.

104. Nasiriavanaki, M., et al., *High-resolution photoacoustic tomography of resting-state functional connectivity in the mouse brain.* Proceedings of the National Academy of Sciences, 2014. **111**(1): p. 21-26.

105. Yao, J., et al., *Multiscale photoacoustic tomography using reversibly switchable bacterial phytochrome as a near-infrared photochromic probe.* Nature methods, 2016. **13**(1): p. 67-73.

106. Na, S., et al., *Massively parallel functional photoacoustic computed tomography of the human brain.* Nature Biomedical Engineering, 2022. **6**(5): p. 584-592.

107. Tang, J., et al., *Noninvasive high-speed photoacoustic tomography of cerebral hemodynamics in awake-moving rats.* Journal of Cerebral Blood Flow & Metabolism, 2015. **35**(8): p. 1224-1232.

108. Tang, J., et al., *Wearable 3-D photoacoustic tomography for functional brain imaging in behaving rats.* Scientific reports, 2016. **6**(1): p. 1-10.

109. Wang, B., et al., *A novel detachable head-mounted device for simultaneous EEG and photoacoustic monitoring of epilepsy in freely moving rats.* Neuroscience Research, 2015. **91**: p. 57-62.

110. Gottschalk, S., et al., *Rapid volumetric optoacoustic imaging of neural dynamics across the mouse brain.* Nature Biomedical Engineering, 2019. **3**(5): p. 392-401.

111. Yao, J., et al., *High-speed label-free functional photoacoustic microscopy of mouse brain in action.* Nature methods, 2015. **12**(5): p. 407-410.

112. Yao, J., et al., *Real-time whole-brain imaging of hemodynamics and oxygenation at micro-vessel resolution with ultrafast wide-field photoacoustic microscopy.* 2022.

113. Cao, R., et al., *Functional and oxygen-metabolic photoacoustic microscopy of the awake mouse brain.* Neuroimage, 2017. **150**: p. 77-87.

114. Sciortino, V.M., et al., *Longitudinal cortex-wide monitoring of cerebral hemodynamics and oxygen metabolism in awake mice using multi-parametric photoacoustic microscopy.* Journal of Cerebral Blood Flow & Metabolism, 2021. **41**(12): p. 3187-3199.

115. Cao, R., et al., *Photoacoustic microscopy of obesity-induced cerebrovascular alterations.* Neuroimage, 2019. **188**: p. 369-379.

116. Govinahallisathyanarayana, S., et al., *Dictionary learning-based reverberation removal enables depth-resolved photoacoustic microscopy of cortical microvasculature in the mouse brain.* Scientific reports, 2018. **8**(1): p. 1-12.

117. Qin, W., et al., *High-resolution in vivo imaging of rhesus cerebral cortex with ultrafast portable photoacoustic microscopy.* NeuroImage, 2021. **238**: p. 118260.

118. Jin, T., et al., *Photoacoustic imaging of brain functions: wide filed-of-view functional imaging with high spatiotemporal resolution.* Laser & Photonics Reviews, 2022. **16**(2): p. 2100304.

119. Xu, Z., et al., *Detecting metastatic potential of cancer through longitudinal vasculature imaging of biomaterial scaffold using non-invasive in vivo photoacoustic microscopy and optical coherence tomography.* Theranostics, 2025. **15**(2): p. 509.

120. Lavaud, J., et al., *Noninvasive monitoring of liver metastasis development via combined multispectral photoacoustic imaging and fluorescence diffuse optical tomography.* International Journal of Biological Sciences, 2020. **16**(9): p. 1616.

121. Zhou, Q., et al., *In vivo photoacoustic tomography of EGFR overexpressed in hepatocellular carcinoma mouse xenograft.* Photoacoustics, 2016. **4**(2): p. 43-54.

122. Wang, K., et al., *Multifunctional fluorescence/photoacoustic bimodal imaging of γ-glutamyltranspeptidase in liver disorders under different triggering conditions.* Biomaterials, 2024. **310**: p. 122635.

123. Lee, S., et al., *Non-invasive monitoring of the therapeutic response in sorafenib-treated hepatocellular carcinoma based on photoacoustic imaging.* European Radiology, 2018. **28**: p. 372-381.

124. Zeng, S., et al., *NIR-II photoacoustic imaging-guided oxygen delivery and controlled release improves photodynamic therapy for hepatocellular carcinoma.* Advanced Materials, 2024. **36**(4): p. 2308780.

125. Shao, W., et al., *NIR-II absorbing organic nanoagents for photoacoustic imaging and photothermal therapy.* BMEMat, 2023. **1**(1): p. e12009.

126. Yu, Q., et al., *Label-free visualization of early cancer hepatic micrometastasis and intraoperative image-guided surgery by photoacoustic imaging.* Journal of Nuclear Medicine, 2020. **61**(7): p. 1079-1085.

127. Qiu, T., et al., *Assessment of liver function reserve by photoacoustic tomography: a feasibility study.* Biomedical Optics Express, 2020. **11**(7): p. 3985-3995.

128. Lv, J., et al., *Quantitative Functional Evaluation of Liver Fibrosis in Mice with Dynamic Contrast-enhanced Photoacoustic Imaging.* Radiology, 2021. **300**(1): p. 89-97.

129. Sun, T., et al., *In vivo liver function reserve assessments in alcoholic liver disease by scalable photoacoustic imaging.* Photoacoustics, 2023. **34**: p. 100569.

130. Huang, G., et al., *In vivo quantitative photoacoustic evaluation of the liver and kidney pathology in tyrosinemia.* Photoacoustics, 2022. **28**: p. 100410.

131. Li, W., et al., *Quantification of Vascular Remodeling and Sinusoidal Capillarization to Assess Liver Fibrosis with Photoacoustic Imaging.* Radiology, 2025. **314**(1): p. e241275.

132. Liu, S. and J. Parvizi, *Cognitive refractory state caused by spontaneous epileptic high-frequency oscillations in the human brain.* Science Translational Medicine, 2019. **11**(514): p. eaax7830.

133. Bräuner, T., D.F. Hülser, and R.J. Strasser, *Comparative measurements of membrane potentials with microelectrodes and voltage-sensitive dyes.* Biochimica et Biophysica Acta, 1984. **771**(2): p. 208-16.

134. Shapiro, H.M., *Cell membrane potential analysis.* Methods in Cell Biology, 1994. **41**: p. 121-33.

135. Yu, Q., X. Wang, and L. Nie, *Optical recording of brain functions based on voltage-sensitive dyes.* Chinese Chemical Letters, 2021. **32**(6): p. 1879-1887.

136. Fu, W., et al., *Convergence of olfactory and gustatory connections onto the endopiriform nucleus in the rat.* Neuroscience, 2004. **126**(4): p. 1033-41.

137. Sejnowski, T.J. and A. Destexhe, *Why do we sleep?* Brain Research, 2000. **886**(1-2): p. 208-223.

138. Yang, W. and R. Yuste, *In vivo imaging of neural activity.* Nature Methods, 2017. **14**(4): p. 349-359.

139. Stosiek, C., et al., *In vivo two-photon calcium imaging of neuronal networks.* Proceedings of the National Academy of Sciences, 2003. **100**(12): p. 7319-7324.

140. Hasan, M.T., et al., *Functional fluorescent Ca2+ indicator proteins in transgenic mice under TET control.* PLoS biology, 2004. **2**(6): p. e163.

141. Chen, T.-W., et al., *Ultrasensitive fluorescent proteins for imaging neuronal activity.* Nature, 2013. **499**(7458): p. 295-300.

142. Ouzounov, D.G., et al., *In vivo three-photon imaging of activity of GCaMP6-labeled neurons deep in intact mouse brain.* Nature Methods, 2017. **14**(4): p. 388-390.

143. Piatkevich, K.D., et al., *Population imaging of neural activity in awake behaving mice.* Nature, 2019. **574**(7778): p. 413-417.

144. Wang, L.V. and S. Hu, *Photoacoustic tomography: in vivo imaging from organelles to organs.* Science, 2012. **335**(6075): p. 1458-62.

145. Pang, W., et al., *Two-Dimensional Photoacoustic/Ultrasonic Endoscopic Imaging Based on a Line-Focused Transducer.* Frontiers in Bioengineering and Biotechnology, 2022. **9**: p. 807633.

146. Zhou, Y., et al., *Small Animal In Situ Drug Delivery Effects via Transdermal Microneedles Array versus Intravenous Injection: A Pilot Observation Based on Photoacoustic Tomography.* Pharmaceutics, 2022. **14**(12): p. 2689.

147. Chen, R., et al., *Photoacoustic molecular imaging-escorted adipose photodynamic–browning synergy for fighting obesity with virus-like complexes.* Nature Nanotechnology, 2021. **16**(4): p. 455-465.

148. Huang, X., et al., *Clothing spiny nanoprobes against the mononuclear phagocyte system clearance in vivo: Photoacoustic diagnosis and photothermal treatment of early stage liver cancer with erythrocyte membrane-camouflaged gold nanostars.* Applied Materials Today, 2020. **18**: p. 100484.

149. Kothapalli, S.-R., et al., *Simultaneous transrectal ultrasound and photoacoustic human prostate imaging.* Science Translational Medicine, 2019. **11**(507): p. eaav2169.

150. Shemetov, A.A., et al., *A near-infrared genetically encoded calcium indicator for in vivo imaging.* Nature Biotechnology, 2021. **39**(3): p. 368-377.

151. Liu, Z., et al., *Sustained deep-tissue voltage recording using a fast indicator evolved for two-photon microscopy.* Cell, 2022. **185**(18): p. 3408-3425. e29.

152. Huber, D., et al., *Multiple dynamic representations in the motor cortex during sensorimotor learning.* Nature, 2012. **484**(7395): p. 473-478.

153. Jin, L., et al., *Single Action Potentials and Subthreshold Electrical Events Imaged in Neurons with a Fluorescent Protein Voltage Probe.* Neuron, 2012. **75**(5): p. 779-785.

154. Yamada, A., et al., *Usefulness and Limitation of DiBAC4(3), a Voltage-Sensitive Fluorescent Dye, for the Measurement of Membrane Potentials Regulated by Recombinant Large Conductance Ca2+-Activated K+ Channels in HEK293 Cells.* Japanese Journal of Pharmacology, 2001. **86**(3): p. 342-350.

155. Janko, C., et al., *Navigation to the graveyard-induction of various pathways of necrosis and their classification by flow cytometry*, in *Necrosis: Methods and Protocols*. 2013, Springer. p. 3-15.

156. Zhang, C., L. Long, and C. Shi, *Mitochondria-Targeting IR-780 Dye and Its Derivatives: Synthesis, Mechanisms of Action, and Theranostic Applications.* Advanced Therapeutics, 2018. **1**(7): p. 1800069.

157. Singh, A.P. and P. Nicholls, *Cyanine and safranine dyes as membrane potential probes in cytochrome c oxidase reconstituted proteoliposomes.* Journal of Biochemical and Biophysical Methods, 1985. **11**(2-3): p. 95-108.

158. Boix-Lemonche, G., M. Lekka, and B. Skerlavaj, *A Rapid Fluorescence-Based Microplate Assay to Investigate the Interaction of Membrane Active Antimicrobial Peptides with Whole Gram-Positive Bacteria.* Antibiotics, 2020. **9**(2): p. 92.

159. Sims, P.J., et al., *Mechanism by which cyanine dyes measure membrane potential in red blood cells and phosphatidylcholine vesicles.* Biochemistry, 1974. **13**(16): p. 3315-3330.

160. Zhang, H.K., et al., *Listening to membrane potential: photoacoustic voltage-sensitive dye recording.* Journal of biomedical optics, 2017. **22**(4): p. 045006.

161. Dhir, A., *Pentylenetetrazol (PTZ) Kindling Model of Epilepsy.* Current Protocols in Neuroscience, 2012. **58**(1): p. 9-37.

162. Samokhina, E. and A. Samokhin, *Neuropathological profile of the pentylenetetrazol (PTZ) kindling model.* International Journal of Neuroscience, 2018. **128**(11): p. 1086-1096.

163. Xi, L., et al., *Hybrid photoacoustic and electrophysiological recording of neurovascular communications in freely-moving rats.* Neuroimage, 2017. **161**: p. 232-240.

164. Deán-Ben, X.L., et al., *Functional optoacoustic neuro-tomography for scalable whole-brain monitoring of calcium indicators.* Light: Science & Applications, 2016. **5**(12): p. e16201-e16201.

165. Matthes, R., et al., *Guidelines on Limits of Exposure to Laser Radiation of Wavelengths between 180 nm and 1,000 μm.* Health Physics, 2013. **105**(3): p. 271-295.

166. Zharov, V.P., et al., *In vivo photoacoustic flow cytometry for monitoring of circulating single cancer cells and contrast agents.* Optics Letters, 2006. **31**(24): p. 3623-3625.

167. Acharya, U.R., et al., *Automated EEG analysis of epilepsy: A review.* Knowledge-Based Systems, 2013. **45**: p. 147-165.

168. Murugappan, M. and S. Murugappan. *Human emotion recognition through short time Electroencephalogram (EEG) signals using Fast Fourier Transform (FFT)*. in *2013 IEEE 9th International Colloquium on Signal Processing and its Applications*. 2013. Kuala Lumpur: IEEE.

169. Zhu, X., et al., *Optical Brain Imaging: A Powerful Tool for Neuroscience.* Neuroscience Bulletin, 2017. **33**(1): p. 95-102.

170. Osten, P. and T.W. Margrie, *Mapping brain circuitry with a light microscope.* Nature Methods, 2013. **10**(6): p. 515-23.

171. Trachtenberg, J.T., et al., *Long-term in vivo imaging of experience-dependent synaptic plasticity in adult cortex.* Nature, 2002. **420**(6917): p. 788-94.

172. Holtmaat, A., et al., *Long-term, high-resolution imaging in the mouse neocortex through a chronic cranial window.* Nature Protocols, 2009. **4**(8): p. 1128-44.

173. Xu, H.T., et al., *Choice of cranial window type for in vivo imaging affects dendritic spine turnover in the cortex.* Nature Neuroscience, 2007. **10**(5): p. 549-51.

174. Grutzendler, J., et al., *Transcranial two-photon imaging of the living mouse brain.* Cold Spring Harbor Protocols, 2011. **2011**(9): p. 065474.

175. Linares-Hernández, L., et al., *Voltage-dependent calcium influx in human sperm assessed by simultaneous optical detection of intracellular calcium and membrane potential.* Biochimica et Biophysica Acta, Biomembranes, 1998. **1372**(1): p. 1-12.

176. Hrynevich, S.V., et al., *Influence of Glucose Deprivation on Membrane Potentials of Plasma Membranes, Mitochondria and Synaptic Vesicles in Rat Brain Synaptosomes.* Neurochemical Research, 2015. **40**(6): p. 1188-1196.

177. Alvarez-Bustamante, J.A. and V.V. Lemeshko, *Computational models for monitoring the trans-membrane potential with fluorescent probes: the DiSC3(5) case.* European Biophysics Journal, 2016. **45**(8): p. 815-830.

178. Li, L., et al., *Single-impulse Panoramic Photoacoustic Computed Tomography of Small-animal Whole-body Dynamics at High Spatiotemporal Resolution.* Nat Biomed Eng, 2017. **1**(5).

179. Kalva, S.K., et al., *Spiral volumetric optoacoustic tomography for imaging whole-body biodynamics in small animals.* Nature Protocols, 2023. **18**(7): p. 2124-2142.

180. Na, S., et al., *Massively parallel functional photoacoustic computed tomography of the human brain.* Nature Biomedical Engineering, 2022. **6**(5): p. 584-592.

181. Zhou, J. and J.V. Jokerst, *Photoacoustic imaging with fiber optic technology: A review.* Photoacoustics, 2020. **20**: p. 100211.

182. Lai, P., et al., *Photoacoustically guided wavefront shaping for enhanced optical focusing in scattering media.* Nature Photonics, 2015. **9**(2): p. 126-132.

183. Yu, Z., et al., *Wavefront shaping: A versatile tool to conquer multiple scattering in multidisciplinary fields.* Innovation, 2022. **3**(5): p. 100292.

184. Bataller, R. and D.A. Brenner, *Liver fibrosis.* The Journal of clinical investigation, 2005. **115**(2): p. 209-218.

185. Roehlen, N., E. Crouchet, and T.F. Baumert, *Liver fibrosis: mechanistic concepts and therapeutic perspectives.* Cells, 2020. **9**(4): p. 875.

186. Poynard, T., et al., *Liver fibrosis evaluation using real-time shear wave elastography: applicability and diagnostic performance using methods without a gold standard.* Journal of hepatology, 2013. **58**(5): p. 928-935.

187. Dietrich, C.F., et al., *EFSUMB guidelines and recommendations on the clinical use of liver ultrasound elastography, update 2017 (long version).* Ultraschall in der Medizin-European Journal of Ultrasound, 2017. **38**(04): p. e16-e47.

188. Martinez, S.M., et al., *Noninvasive assessment of liver fibrosis.* Hepatology, 2011. **53**(1): p. 325-335.

189. Pang, W., et al., *Multi-Parametric Photoacoustic Elastomicroscopy: Quantitative Elasticity Mapping and Microstructural Analysis for Early-Stage Hepatic Fibrosis Detection.* Journal of Physics: Photonics, 2025.

190. Zhou, Y., et al., *Single-shot linear dichroism optical-resolution photoacoustic microscopy.* Photoacoustics, 2019. **16**: p. 100148.

191. Insana, M.F. and J.C. Bamber, *Tissue motion and elasticity imaging*. 2000. p. 001.

192. Joshi, R., et al., *Accuracy and reliability of palpation and percussion for detecting hepatomegaly: a rural hospital-based study.* Indian Journal of Gastroenterology, 2004. **23**: p. 171-174.

193. Ghany, M.G. and E. Doo, *Assessment of liver fibrosis: palpate, poke or pulse?* Hepatology, 2005. **42**(4): p. 759-761.

194. Park, C.C., et al., *Magnetic resonance elastography vs transient elastography in detection of fibrosis and noninvasive measurement of steatosis in patients with biopsy-proven nonalcoholic fatty liver disease.* Gastroenterology, 2017. **152**(3): p. 598-607. e2.

195. Zhou, M., et al., *Multi-Scale Spatial Heterogeneity of Liver Fibrosis Evaluated by MR Elastography in Rat Models.* Journal of Magnetic Resonance Imaging. **n/a**(n/a).

196. Wilson, M.P., et al., *Comparing FIB-4, VCTE, pSWE, 2D-SWE, and MRE Thresholds and Diagnostic Accuracies for Detecting Hepatic Fibrosis in Patients with MASLD: A Systematic Review and Meta-Analysis.* Diagnostics, 2025. **15**(13): p. 1598.

197. Sigrist, R.M., et al., *Ultrasound elastography: review of techniques and clinical applications.* Theranostics, 2017. **7**(5): p. 1303.

198. Zvietcovich, F., et al., *Reverberant 3D optical coherence elastography maps the elasticity of individual corneal layers.* Nature communications, 2019. **10**(1): p. 4895.

199. Feng, X., et al., *In vivo stiffness measurement of epidermis, dermis, and hypodermis using broadband Rayleigh-wave optical coherence elastography.* Acta Biomaterialia, 2022. **146**: p. 295-305.

200. Rippy, J.R., et al., *Ultrasound Shear Wave Elastography and Transient Optical Coherence Elastography: Side-by-Side Comparison of Repeatability and Accuracy.* IEEE Open Journal of Engineering in Medicine and Biology, 2021. **2**: p. 179-186.

201. Singh, M., et al., *Optical coherence elastography.* Nature Reviews Methods Primers, 2025. **5**(1): p. 39.

202. Li, M., et al., *Atomic force microscopy studies on cellular elastic and viscoelastic properties.* Science China Life Sciences, 2018. **61**: p. 57-67.

203. Singh, M.S. and A. Thomas, *Photoacoustic elastography imaging: a review.* Journal of biomedical optics, 2019. **24**(4): p. 040902-040902.

204. Hai, P., et al., *Quantitative photoacoustic elastography in humans.* Journal of Biomedical Optics, 2016. **21**(6): p. 066011.

205. Wan, M., et al., *Optical-resolution photoacoustic microelastography system for elasticity mapping: Phantom study and practical application.* Journal of Biophotonics, 2024. **17**(8): p. e202400032.

206. Hu, P., et al., *Quantification of Cervical Elasticity During Pregnancy Based on Transvaginal Ultrasound Imaging and Stress Measurement.* IEEE Transactions on Biomedical Engineering, 2024. **71**(10): p. 2948-2955.

207. Yang, F., et al., *Phase-domain photoacoustic mechanical imaging for quantitative elastography and viscography.* IEEE Transactions on Biomedical Engineering, 2024.

208. Mandal, S., et al., *Determining elastic contrast in tissue-mimicking phantoms using frequency resolved photoacoustic imaging*. SPIE BiOS. Vol. 10878. 2019: SPIE.

209. Yuan, Y., et al., *Photoacoustic remote sensing elastography.* Optics Letters, 2023. **48**(9): p. 2321-2324.

210. Cai, C., et al., *Feature coupling photoacoustic computed tomography for joint reconstruction of initial pressure and sound speed in vivo.* Biomedical Optics Express, 2019. **10**(7): p. 3447-3462.

211. Hai, P., et al., *Photoacoustic elastography.* Optics letters, 2016. **41**(4): p. 725-728.

212. Qiu, Y., et al., *Collagen fibers quantification for liver fibrosis assessment using linear dichroism photoacoustic microscopy.* Photoacoustics, 2025: p. 100694.

213. Cui, X.-W., et al., *Ultrasound elastography.* Endoscopic Ultrasound, 2022. **11**(4): p. 252-274.

214. Miao, X., et al., *Liver Fibrosis Assessment by Viewing Sinusoidal Capillarization: US Molecular Imaging versus Two-dimensional Shear-Wave Elastography in Rats.* Radiology, 2022. **304**(2): p. 473-482.

215. Carrillo, F., et al., *Nanoindentation of polydimethylsiloxane elastomers: Effect of crosslinking, work of adhesion, and fluid environment on elastic modulus.* Journal of materials research, 2005. **20**(10): p. 2820-2830.

216. Kondo, S. and T. Igarashi, *Hypersonic sound velocity in liquid and rubbery polymers.* Journal of Applied Physics, 1980. **51**(3): p. 1514-1519.

217. Ormachea, J. and K.J. Parker, *A Preliminary Study of Liver Fat Quantification Using Reported Ultrasound Speed of Sound and Attenuation Parameters.* Ultrasound in Medicine & Biology, 2022. **48**(4): p. 675-684.

218. Yu, Z., et al., *Wavefront shaping: a versatile tool to conquer multiple scattering in multidisciplinary fields.* The Innovation, 2022. **3**(5).

219. Cheng, S., et al., *High-resolution photoacoustic microscopy with deep penetration through learning.* Photoacoustics, 2022. **25**: p. 100314.

220. Huang, T., et al., *Artificial intelligence for medicine: Progress, challenges, and perspectives.* The Innovation Medicine, 2023. **1**(2).

221. Lin, L., et al., *Single-breath-hold photoacoustic computed tomography of the breast.* Nature Communications, 2018. **9**(1): p. 2352.

222. Choi, W., et al., *Three-dimensional Multistructural Quantitative Photoacoustic and US Imaging of Human Feet in Vivo.* Radiology, 2022. **303**(2): p. 467-473.